SPECTRAL SENSING TECHNIQUE FOR WATER CONSTITUENTS

by

JING ZHOU

A dissertation submitted to the Graduate Faculty in Engineering in partial fulfillment of the requirements for the degree of Doctor of Philosophy,

The City University of New York

2006

UMI Number: 3213252

ProQuest Information and Learning Company
300 North Zeeb Road
P.O. Box 1346
Ann Arbor, MI 48106-1346

This manuscript has been read and accepted for the
Graduate Faculty in Engineering in satisfaction of the
dissertation requirement for the degree of Doctor of Philosophy.

Fred Moshary

Date — Chair of Examining Committee

Mumtazk K. Kassir

Date — Executive Officer

Samir Ahmed

Barry Gross

Reza Khanbilvardi

Jacek Chowdhary

Supervisory Committee

THE CITY UNIVERSITY OF NEW YORK

Abstract

SPECTRAL SENSING TECHNIQUE FOR WATER CONSTITUENTS

by

Jing Zhou

Adviser: Professor Fred Moshary

Spectral measurements of optical properties of water were conducted throughout the Chesapeake Bay area during the 2005 summer cruise campaign. This included reflectance, absorption, attenuation and backscattering spectra. The analysis of the data illustrates the diversity and complexity of constituents that shape spectral features of the coastal water. A novel technique is proposed to separate the chlorophyll fluorescence component from the reflectance spectra of algae contained water. This approach utilizes of polarization properties of elastically scattered light and the unpolarized nature of fluorescence and was successfully applied to measurements of various algae species first in lab and later in field measurements. The efficiency and limitation of this approach has been further examined under various conditions as well as through vector radiative transfer modeling. Finally Twomey Iterative Method (TIM) has been applied to the retrieval of hydrosol microphysical properties for the first time. Assuming a known refractive index, both single and multi-mode distributions were successfully retrieved from both simulation and experiments through the introduction of an initial distribution biased towards larger particles. In addition, the technique is extended to the retrieval of an unknown

refractive index, which is also validated using both simulation and experimental results.

To My Parents and Husband

Acknowledgement

First I would like to thank Prof. Fred Moshary who provided me with the opportunity to continue my study in CUNY with full financial support after I got my masters degree in Optical engineering from China. As my mentor, he taught me lots of hands on optical experimental skills, as well as technical writing and lecturing skills, which I believe will definitely benefit me throughout my career.

Also working as part of a team, this thesis has contributions from my many colleagues including professors and research associates in the Optical Remote Sensing Lab at City College. Prof. Samir Ahmed's unique insights into problems have led to interesting directions in research presented here. I thank Prof. Barry Gross for many discussions that helped clarify and organize the concepts presented here. He has also been a great help in polishing my papers. It has been a great opportunity for me to have worked side by side with Dr. Alex Gilerson who has a much broader experience in this field. I have learned a lot from him and his guidance saved me much time during my Ph.D thesis.

Most importantly, I could not have finished the work without the continued and unwavering moral support of my husband, Jian Wu. He moved all the way from Texas up to New Jersey to be closer to me and make life a lot easier for me in this foreign country. He tolerates the life style of being apart from me during weekdays and together with me only in weekends so that I can concentrate more on my research and teaching works. I dedicate this thesis to him with the deepest love and appreciation.

Last but not least, this book is also for my parents' consistent and unselfish love and support. They never complain that their daughter could not be around to take care of them, to celebrate every holiday and birthday with them. All they want is that their daughter is happy and healthy. No words can express my appreciation for what they have given to me.

Table of Contents

List of Tables

List of Figures

Chapter 1 Introduction

When light interacts with matters, it can be either absorbed or scattered thus altering its intensity, direction and polarization depending on the wavelength. These processes frequently result in unique optical characteristics, which are determined by the chemical, physical and biological properties of the substances. Spectral sensing techniques entail recording and analysis these optical features as a function of wavelengths. The utility of spectral measurements has long been recognized in diverse fields from chemistry, to material science,… to remote sensing. Although the measurements of optical properties of water constituents have been carried out for over 50 years, most of the instruments used have been laboratory bench-top spectrophotometers and radiometers with several channels from UV to IR wavelength. These instruments were relatively slow with sample scan rates on the order of minutes to maximize signal to noise. Even just a decade ago, computational limitation also made processing and storage of large amount of spectral data difficult. However, within the last five years, high sample rate (less than seconds) in situ sensors with high resolution (less than 10nm) for remote sensing purpose have been developed and utilized for various coastal and open ocean studies. In addition due to the advances in computer technology, the powerful computation ability has made the rapid processing of hyperspectral data possible and the dramatically miniaturized storage media with high capacity enables us to store and archive these large and often difficult to manage data sets at a low price.

Much of the ocean optics researches of ocean waters have been focused on open oceans. The popular bio-optical models used, that work well for open oceans become problematic when applied to far more complex and biologically productive coastal and in land waters. However, there are increasing demand on monitoring and management of coastal waters as they play an important role in fisheries, natural resources, transport of goods and recreation and that pollution from river, terrestrial run off and contaminants can adversely affect these economical benefits. Hyperspectral measurements provide oceanographers with the potential ability to classify complex oceanic environments. For example, high wavelength resolution absorption measurements make it possible to identify phytoplankton by taxonomic groups by quantification of accessory absorption peaks at featured wavelength. At the same time, such measurements also bring with them challenges in modeling these spectral data for extracting biochemical information of water. The inherent difficulties of the inverse problems require reasonable assumptions for the retrieval. However, due to the large variability of continuants of natural water, especially coastal water, such assumptions are valid only for a limited range of water bodies, which prevents a given algorithm from being applicable to all the cases. For instance, the general empirical shape of chlorophyll absorption spectrum has been often employed in the optical models to relate water constituents to inherent optical properties. However departure from that universal spectral shape for one specific algae species results in large errors in the estimations. The traditional blue-green ratio is able to obtain the chlorophyll concentration from the remote sensing spectra of open ocean, while correlates poorly with the biomass content in most of the coastal

area, where the assumption of correlation between chlorophyll and other constituents is not valid. Use of backscattering ratio to discriminate particle types in water by estimating their bulk refractive index is thought to be the major breakthrough in ocean optics. Whether it can be applied to the non-spherical inhomogeneous particles like algae cells is still not clear. Two of the most important aspects in ocean optical remote sensing are the comprehensive data collection of optical properties in various locations and seasons by using the new generation of instruments and validation of existing algorithms using these new data.

The optical tools are not only valuable in oceanography, but also useful for studies of fresh water and hydrosols microphysics in other field such as noninvasive characterization of tissue cells. One of the most promising applications is to use the UV laser-induced fluorescence for inexpensive and fast water quality monitoring.

This thesis is dedicated to the white light hyper-spectral sensing technique for water analysis. The contribution of this thesis is the following:

1. Field measurement of optical properties including reflectance, absorption, attenuation and backscattering was conducted throughout the Chesapeake Bay area during the 2005 summer cruise campaign. The analysis and bio-optical modeling using this data illustrates the diversity of the coastal water and also is a basis for future algorithm validation.

2. A novel technique is proposed to separate the chlorophyll fluorescence component from the reflectance spectra of algae contained water. This approach makes use of polarization properties of elastically scattered light and the unpolarized nature of

fluorescence and was successfully applied to measurements of various algae species first in lab and later in field measurements in eastern Long Island. The efficiency and limitation of this approach has been further examined under various ocean conditions through vector radiative transfer model.

3. For the first time the Twomey Iterative Method (TIM) has been applied to the retrieval of hydrosol microphysical properties. Assuming a known refractive index, both single and multi-mode distributions were successfully retrieved from both simulation and experiments through the introduction of an initial distribution biased towards larger particles. In addition, the technique is extended to the retrieval of an unknown refractive index, which is also validated using simulated and experimental results.

Chapter 2 Field Measurement and Analysis of Water Optical Properties in Chesapeake Bay

The optical properties of water can be divided into two classes: inherent and apparent. The inherent optical properties (IOP) like the absorption and scattering coefficients depend only upon the medium while the apparent optical properties (AOP) such as reflectance are determined by the medium and the geometric structure of the ambient light field. The overall optical properties of natural water are determined, in part, by the optically active constituents in water. The AOP's are usually computed through radiative transfer or empirical models using the combined IOP's as inputs, which are obtained from the relavant IOP's for each constituent of a water body [1]. The relationships between water optical properties and physical constituents forms the basis of retrieving the concentration of water component of interest such as chlorophyll and mineral particles from both surface and satellite based optical remote sensing data [2,3]. In-situ field measurements of water optical properties can provide not only the necessary input for light field calculation based on radiative transfer method but also create a valuable database for validation of various bio-optical models and inversion algorithms[4]. Calibration and correction of satellite data also rely on the accurate ground based measurements data obtained for different seasons and locations. Such a database is even more important for coastal water, where human activities and terrestrial run-offs have a larger impact than the global nutrition balance on water constituents making it more difficult to predict and describe by traditional simple models. Furthermore, the water constituents and hence water optical properties can vary from oligotrophic, mesotrophic to eutrophic

sometimes on scales of meters, which is difficult to resolve with typical 1-km satellite pixels [5]. Understanding the complex coastal optical properties often relies on the use of in-situ ground based measurements.

In this chapter, we present measurements of both absorption and scattering coefficients as well as reflectance as a function of wavelength from 400nm to 800nm for the Chesapeake Bay area during the 2005 summer cruise campaign. Using a parameterized bio-optical model, a LSQ fitting was applied to the measured absorption and scattering coefficient. The fitted results were then compared with the measurement results from the same cruise.

2.1 Background

2.1.1 Absorption and scattering coefficient

Two of the fundamental IOP's are the absorption coefficient and the volume scattering function. Consider a small volume ΔV of water with thickness Δr, illuminated by a narrow collimated beam of monochromatic light with spectral radiant power P_i, Wnm^{-1}, as schematically illustrated in Fig. 1. Some part of incident power is absorbed within the volume of water $P_a(\lambda)$; some part is scattered out of the beam at an angle θ $P_s(\theta, \lambda)$; and the remaining light $P_t(\lambda)$ propagate in the same direction and transmitted through the volume. The spectral absorption coefficient is defined as the fraction of incident power that has been absorbed per unit length:

$$a(\lambda) = \lim_{\Delta r \to 0} \frac{P_a(\lambda)}{P_i(\lambda)\Delta r} \quad m^{-1} \qquad (1)$$

The angular scattered power per unit length and unit solid angle normalizing to the incident power is defined as volume scattering coefficient $\beta(\theta;\lambda)$ which is a

function of the angle between the directions of incident and scattering light θ (scattering angle, changes from 0 to π):

$$\beta(\theta;\lambda) = \lim_{\Delta r, \Delta\Omega \to 0} \frac{P_S(\theta;\lambda)}{P_i(\lambda)\Delta r \Delta\Omega} \qquad m^{-1}sr^{-1} \qquad (2)$$

Integration of $\beta(\theta;\lambda)$ over the 4π space is the total fraction of incident power per unit distance that has been scattered, and is defined as the scattering coefficient b(λ):

$$b(\lambda) = \lim_{\Delta r \to 0} \frac{P_S(\theta;\lambda)}{P_i(\lambda)\Delta r} = \int_{4\pi} \beta(\theta;\lambda) d\Omega \qquad m^{-1} \quad (3)$$

The attenuation coefficient c(λ) is defined as:

$$c(\lambda) = a(\lambda) + b(\lambda) \qquad m^{-1} \qquad (4)$$

which describes the fraction of incident power loss per unit distance, either absorbed or scattered.

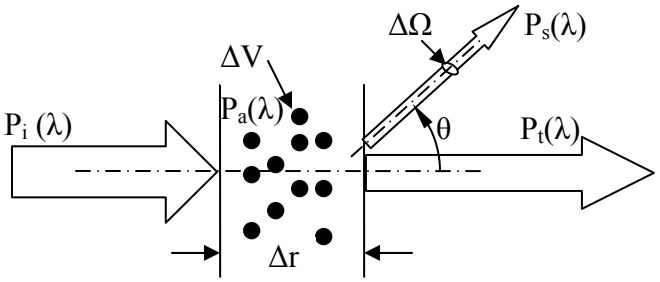

Figure 1 Geometry used to define IOP's

If a water body contains several different substances which have scattering or absorption coefficient a_i, b_i for the ith substances, then a or b of the whole water body is the addition of all of a_i or b_i:

$$a = \sum_i a_i \text{ and } b = \sum_i b_i \qquad (5)$$

Similar approaches can be also applied to the attenuation coefficient c.

2.1.2 Reflectance

Reflectance is a commonly used AOP in the remote sensing field. Consider the case of horizontally homogeneous water bodies, z is the depth measured from the mean sea surface (positive downwards). The spectral irradiance reflectance $R(z;\lambda)$ and remote-sensing reflectance $R_{rs}(z;\theta,\varphi,\lambda)$ are defined as fraction of the spectral upwelling radiance $E_u(z;\lambda)$ or irradiance $L_u(z;\theta,\varphi,\lambda)$ respectively when normalized to the downwelling plane irradiance $E_d(z;\lambda)$.

$$R(z;\lambda) = \frac{E_u(z;\lambda)}{E_d(z;\lambda)} \qquad (6)$$

$$R_{rs}(z;\theta,\varphi,\lambda) = \frac{L_u(z;\theta,\varphi,\lambda)}{E_d(z;\lambda)} \quad sr^{-1} \qquad (7)$$

The remote sensing reflectance is most commonly associated with the IOP's in the water and is therefore of great significance.

2.1.3 Single particle scattering (Mie theory)

To model the IOP's from microphysical properties, we need techniques that can supply the relevant scattering and absorption properties. Mie theory is the rigorous solution of single particle scattering of homogeneous spheres with arbitrary size. Even though not all the particles in water are spherical, it is still often used for the simulation of scattering properties of particulates in water. Fig. 2 shows the basic geometry in scattering from a spherical particle. The plane wave, assumed to propagate along the x axis, interacts with a particle located at the origin with radius r and refractive index n_p. Here, E is the electrical field strength of the light and the

different subscripts (v,h) represent the polarized component perpendicular and parallel to the scattering plane formed by the incident and scattered direction (the xy plane in Fig. 2). The angular distribution of the polarized scattered light intensity $I_v(\theta,\varphi)$ and $I_h(\theta,\varphi)$ in the far field (distance d) can be obtained through the spherical wave solution of Maxwell equations:

$$\begin{aligned} I_v(\theta,\varphi) &= i_1(\theta,\varphi) I_{v0} / {k_0}^2 d^2 \\ I_h(\theta,\varphi) &= i_2(\theta,\varphi) I_{v0} / {k_0}^2 d^2 \end{aligned} \qquad (8)$$

where k_0 is the wave number of incident light $k_0 = \frac{2\pi n_m}{\lambda}$, n_m is the refractive index of the surrounding media. The scattering angle θ is the angle between the direction of scattered and incident light and φ is azimuthal angle. $i_1(\theta,\varphi)$ and $i_2(\theta,\varphi)$ depend on the refractive index of the particle relative to surrounding media $n = \frac{n_p}{n_m}$, r and λ [6]. For natural incident sunlight which is unpolarized, the scattering power per solid angle is $\frac{dP}{d\Omega} = \frac{i(\theta,\varphi)}{k^2} I_0$ with $i = \frac{i_1 + i_2}{2}$. For convenience, the differential scattering cross-section is defined as $\sigma(\theta,\varphi) = \frac{i(\theta,\varphi)}{k^2}$, so that $\frac{dP}{d\Omega} = I_0 \sigma$. From spherical symmetry, the scattered light intensity actually only depends on θ so that the light scattered by a single particle is: $P = \int dP = I_0 \int \sigma(\theta,\varphi) \sin\theta \cdot d\theta d\varphi = I_0 \sigma_s$. Here σ_s is total scattering cross section: $\sigma_s = \int \sigma(\theta,\varphi) \sin\theta \cdot d\theta d\varphi$. The cross section can be converted to the dimensionless efficiency by dividing by the geometrical cross section area of the particle. For example, the total scattering efficiency is $Q_s = \frac{\sigma_s}{\pi \cdot r^2}$.

If we focus on the angle dependence of the scattering only, $\sigma(\theta,\varphi)$ can be made dimensionless by normalizing the directional scatter to the total scatter σ_s, so the normalized scatter or phase function is given as: $p(\theta,\varphi)=\dfrac{\sigma(\theta,\varphi)}{\sigma_s}$.

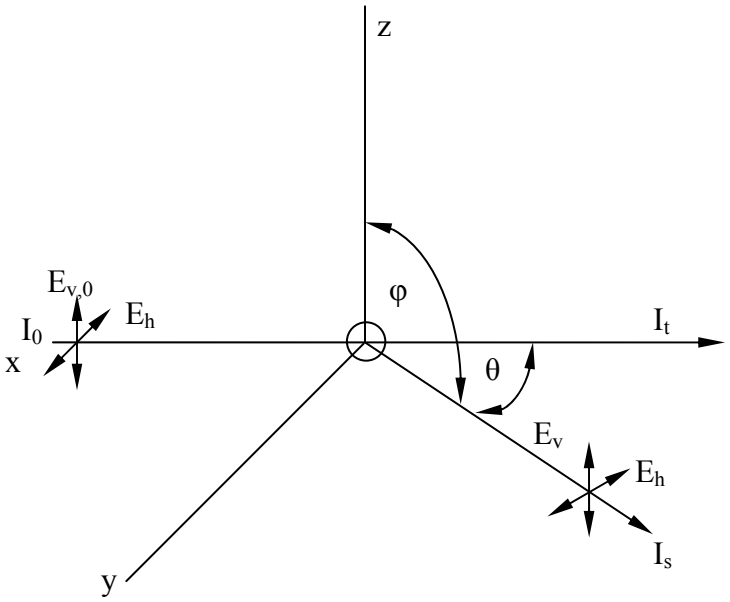

Figure 2 Geometry of single particle scattering

When dealing with a system containing many particles, the total scattering is the sum of contributions from each individual particle in the system assuming that the light is only scattered once before it reaches the detector (single scattering regime). Suppose N_i (m^{-3}) is the number density for the ith type of particles with total and scattering cross section $\sigma_{s,i}$ and $\sigma_i(\theta,\varphi)$, respectively, then the total scattering coefficient and the volume scattering function of this system are given as:

$$b=\sum_i N_i\sigma_{s,i} \text{ and } \beta(\theta,\varphi)=\sum_i N_i\sigma_i(\theta,\varphi).$$

Of course, if we have a continuous distribution of particle sizes, the summations are replaced by suitable integrations.

2.2 Optically significant constituent in water and its bio-optical modeling

2.2.1 Optically significant constituent

The physical constituents in water can be divided into dissolved matter and particulate matter according to their sizes. A general diagram of their categorization is displayed in Fig. 3.

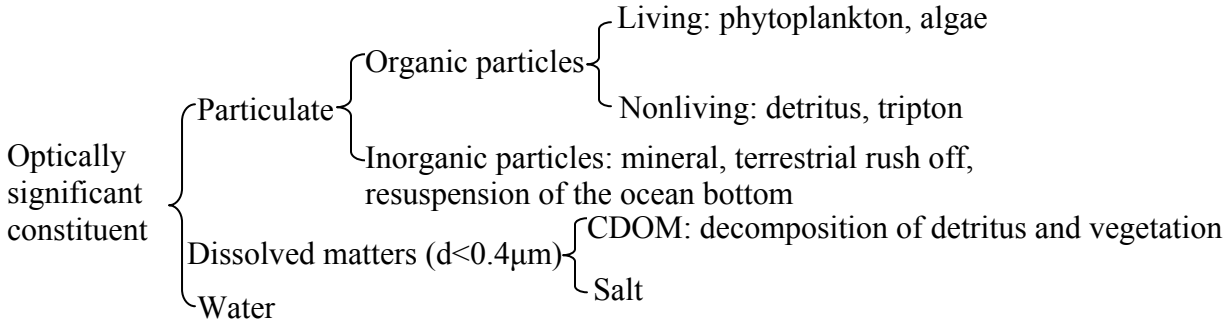

Figure 3 Diagram of optically significant constituent

Particles with diameter less than 0.4μm are considered to be dissolved in water. For these particles, only absorption is significant and scattering effects are negligible. Within this category, colored dissolved organic matters (CDOM) is one of the most commonly occurring substances in natural water and results from the decomposition of vegetation and phytoplankton detritus. CDOM is also called yellow substance since it absorbs strongly in the blue region and appears brownish. The wavelength dependence of its absorption coefficient a_y is generally modeled as:

$$a_y = a_{y_0} \exp[-0.014(\lambda - \lambda_0)] \qquad (9)$$

with a_{y_0} is the absorption at λ_0 =400nm. Dissolved salt can also absorb light which leads to an increase in absorption coefficient for pure saline water when compared with pure water.

Particulate matter can have either an organic or inorganic source. One of the most important living organisms in the ocean is phytoplankton, in which the major absorbing pigment is Chlorophyll a. Phytoplankton has strong absorption bands in both the blue and red (i.e. 440nm and 665nm) with very little absorption in the green region. Although the shape of spectral absorption for phytoplankton varies with different types of algae due to the pigment packaging effect, its absorption coefficient a_{phy} is often expressed as

$$a_{phy} = 0.06 a_c^{*} C_{chl}^{0.65} \qquad (10)$$

where a_c^{*} is a nondimensional, statistically derived and regionally tuned chlorophyll-specific absorption coefficient and C_{chl} is the chlorophyll concentration. In addition to the organic phytoplankton, nonliving organic particles (detritus or tripton) are produced from the body of phytoplankton when they die. Other particulates mainly consist of clay minerals, may enter the ocean system through terrestrial rush off and resuspension of the ocean bottom. Both of them have very similar exponential spectral absorption features with CDOM but are much weaker absorbers than CDOM. Their respective models are:

$$\begin{aligned} a_{\text{det}} &= a_{\text{det}_0} \exp[-0.011(\lambda - \lambda_0)] \\ a_{\text{min}} &= a_{\text{min}_0} \exp[-0.009(\lambda - \lambda_0)] \end{aligned} \qquad (11)$$

where a_{det_0} and a_{min_0} are the absorption coefficient of detritus and mineral particles at λ_0=400nm.

The typical absorption spectra for pure water, CDOM and phytoplankton are plotted in Fig. 4. From the graph, we can see that pure water can also absorbs light very strongly specifically above 720nm. In this region, the strong water absorption

makes the water essentially black except for coastal waters where large sediments can still reflect light.

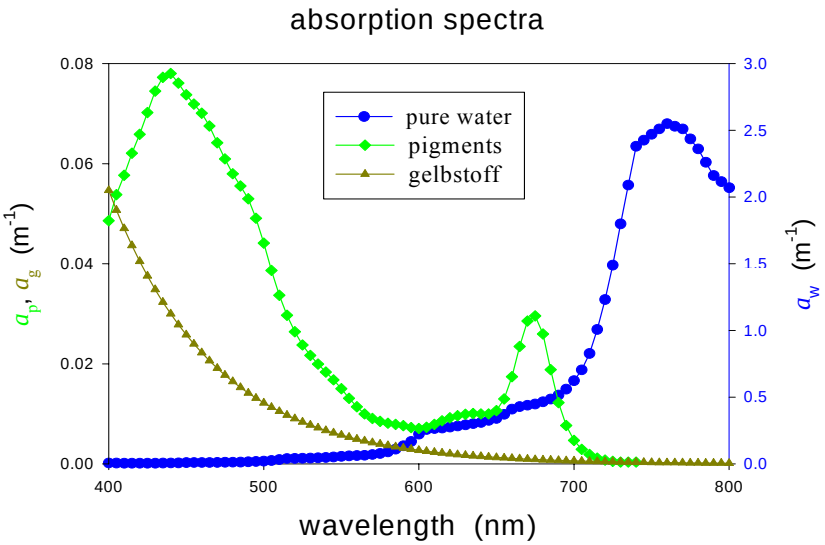

Figure 4 Typical spectral absorptions of pure water, chlorophyll and CDOM

The characterization of the spectral scattering coefficients for spherical particulates having a particular size distribution $f(r)$ and refractive index n is given as integration over the size dependant Mie cross-sections: $b = \int_0^\infty \sigma_s(r,n,\lambda) \cdot f(r) dr$. Similar integration form also holds for backscattering. It is often assumed that the particle size distribution is given by a power law function with a slope ξ (Junge distribution): $f(r) = f_0 r^{-\xi}$. In this case, the spectral dependence of the scattering coefficient b is also given as a power law $b = b_0 \lambda^{-\gamma}$ where the exponents are connected by $\gamma \approx \xi - 3$. The mineral particles are considered more effective scatters especially for backscattering than phytoplankton cells due to their higher refractive

index. Taking advantage of this, the average refractive index can be estimated from the ratio of backscattering and total scattering coefficients [9].

2.2.2 Bio-optical models of water optical properties

It is often desirable to describe the optical properties of water in terms of chlorophyll a concentration as this pigment is responsible for the photosynthesis process and is highly correlated to the nutrition movements of ocean. For this purpose, natural water will be divided into two types: case I and case II water. Case I water occurs when chlorophyll a is dominant in absorption and scattering and the concentrations of all the other substances are low and co-vary with its concentration, which covers over 90% of the open ocean water. In this case, the optical properties (IOP) of water can be modeled as a function of chlorophyll concentration:

$$
\begin{aligned}
&a(\lambda) = a_w(\lambda) + 0.06 a_c^*(\lambda) C_{chl}^{0.65} + a_{y_0} \exp(-0.014(\lambda - \lambda_0)) \\
&a_{y_0} = 0.2[a_w(\lambda_0) + 0.06 C_{chl}^{0.65}] \qquad \lambda_0 = 400nm \qquad (12) \\
&b = b_w + (\frac{550}{\lambda}) 0.3 C_{chl}^{0.62}
\end{aligned}
$$

where a_w and b_w are absorption and scattering coefficient of pure water.

When other constituents do not covary with the chlorophyll concentration, the optical properties become far more complex which is commonly referred to as case II water. Most of the coastal waters belong to this category and the relations between the optical properties of case II water and the water constituents can vary significantly from one location to another or even seasonally. Obviously, it is far more difficult to obtain a single general model to quantify the optical spectral features for all the cases encountered in the real ocean. Therefore, for accurate remote sensing, it is extremely important to obtain a complete set of ground based field measurements as the

necessary basis to validate general bio-optical models and optimize it according to regional situations. The next section describes this procedure during the 2005 summer cruise campaign throughout the Chesapeake Bay area.

2.3 Field measurements in Chesapeake Bay

2.3.1 Optical instruments

In-situ measurements were carried out at 42 stations shown in Fig. 5 across the whole Chesapeake Bay area from July 11th to 20th 2005 using a ship-deployed profiling package assembled by WET Labs (Philomath, Oregon). This package consists of three instruments: an AC-S, an ECO-scattering meter and a CTD, as shown in Fig. 6. The AC-S has dual 25cm flow cells in which spectral absorption and attenuation are measured every 250ms at 82 wavelengths from 400nm to 800nm. To obtain accurate absorption measurements, the inner side of the tube is coated with quartz which can reflect the scattered light back into the chamber and finally collected by the detector. In order to increase the field of view, the tube has a larger inner radius with large effective detection area. The inside of the attenuation tube is thin with a small detector area and is made of black plastic so that it absorbs most of the light hitting the wall and only allows the signal along the light path to reach the detector. The water sample is pumped into the chambers through one of the intakes and a filter is installed at another intake to prevent large objects such as stones from entering the tubes and damaging the meters. The ECO-scattering meter has 9 wavelength channels from 9 LEDs modulated at 1Hz to eliminate vibrational noise. Seven channels measure the volume scattering at one nominal angle of 117˚ and the total backscattering coefficient is estimated assuming a constant proportionality

between β (117˚) and b_b. The remaining two channels are for chlorophyll and CDOM measurement through fluorescence excitation. Conductivity, temperature and depth parameters were recorded every 1.25s with a conductivity-temperature-depth (CTD) sensor (SBE37-SI) from SeaBird Inc. A data logger was used to power all the instruments, acquire data, coordinate different timing schemes and transmit the data up through a single cable to the computer. The depth of the profiler was raised and lowered either manually or by automatic winch in order to sample the depth profile of the ocean. The whole system was cleaned with pure water after every cruise day.

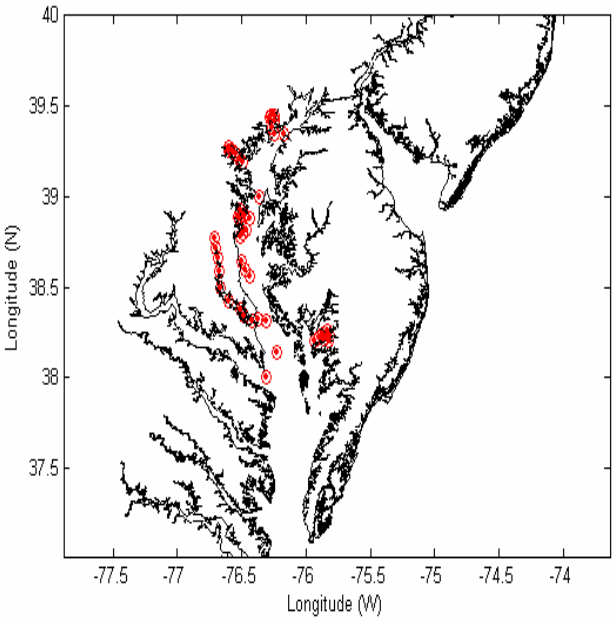

Figure 5 Map of Chesapeake Bay with the locations
of the 42 station sampled

At the same time, the upwelling and downwelling radiance from the water were collected and delivered by fiber bundles to the spectroradiometers (Ocean optics). The fiber probe for upwelling measurements was placed just beneath the

surface so that reflectance from the ocean surface can be obtained from normalizing the upwelling radiance to the downwelling radiance.

Figure 6 Wetlabs instrument suite

2.3.2 Data correction

Temperature and salinity correction is performed to take into account the difference in the absorption and attenuation coefficient between pure water used for the calibration of the AC-S before the measurement and the water encountered in the field measurements. These effects are larger for the red channels with the salinity effect being less significant compared to temperature recalibration.

Furthermore, due to the finite acceptance angle of the detector, the reflecting tube of absorption meter does not collect all of the light scattered from the beam. This uncollected light will lead to an overestimation of the absorption coefficient. Assuming a fixed proportion ε of the scattering coefficient b(λ) will be cut off by the sensors, the measured absorption coefficient a_m should be the actual coefficient a plus

a correction term εb(λ): $a_m = a + \varepsilon b(\lambda) = a + \varepsilon[c(\lambda) - a(\lambda)]$. This correction term will be included in the fitting process described later. At the same time, there is always a part of the scattered light entering the detecting system in the attenuation meter, which causes underestimation of attenuation coefficient. However, the scattering correction of attenuation coefficient is not recommended by the manufacturer as it is extremely complicated and sometime ambiguous.

During the scattering measurement, there was also attenuation along the path from the light source to the detector which depends on the FOV of sample volume so an attenuation correction was also made for the scattering data [8].

2.4 Least Square Fitting

2.4.1 Parameterization of absorption

Since the influence of water absorption has already been excluded by calibrating the AC-S through pure water, the obtained total absorption coefficient am mainly comes from yellow substance ay and chlorophyll pigments contained in the phytoplankton a_{phy} plus a scattering correction term.

$$a_m = a + \varepsilon[c(\lambda) - a(\lambda)] = a_y(\lambda) + a_{phy}(\lambda) + \varepsilon[c(\lambda) - a(\lambda)]$$

$$a_y = a_{y_0} \exp[-s(\lambda - \lambda_0)] \qquad \lambda_0 = 400nm$$
$$a_{phy} = 0.06 a_c^{*} C_{chl}^{0.65} \qquad (13)$$

It should be noted that other non-pigment components such as detritus and mineral particles are absorbed into the yellow substance since they have very similar spectral shape and CDOM is the dominant absorbing matters. Therefore the s parameter is actually the average slope for all the non-pigments. Thus our model of the total

absorption coefficient has 4 parameters: the chlorophyll concentration C_{chl}, absorption at λ_0 of yellow substance a_{y0}, the average decaying slope s and the scattering correction ε.

2.4.2 Parameterization of scattering and attenuation

Given the particulate attenuation and absorption, the total scattering coefficient from particles can be computed as b=c-a. Here, b(λ) is commonly taken to be inversely proportional to wavelength and its amplitude at 550nm is determined by the chlorophyll concentration when scattering from phytoplankton cells are dominant:

$$b(\lambda) = 0.3C_{chl}^{0.62}\frac{550}{\lambda} \qquad (14)$$

However poor fitting results were obtained between the model $b(\lambda) = A(\frac{550}{\lambda})^{\gamma}$, (A and γ are the fitting parameters) and our scattering spectra. In fact, due to the imaginary part of refractive index of chlorophyll, the wavelength dependence of the scattering will have two dips around the absorption peak of chlorophyll pigments. This may be the reason that the shape of the scattering spectra to differs from the traditional model [9]. It should also be noted that the impact of the spectral dependence of absorption on the spectral scattering characteristics can be seen more clearly by sampling 81 wavelengths in the visible range (acs) than measuring the absorption a and extinction c at only 9 wavelengths (ac-9) as done in other papers[9]. We find however that the featured structure in the absorption spectrum is some what compensated by the absorption modulated scattering spectrum. Therefore the particulate attenuation spectra c(λ) appear to be smooth functions and decrease monotonically with increasing wavelength as a power law model:

$$c(\lambda) = A_c \lambda^{-\gamma} \qquad (15)$$

Therefore, the attenuation spectra can be expressed as a function of wavelength with two parameters amplitude A_c and the exponent γ.

2.5 Data and Results

To get a feeling about the general features of measured spectral data, we plot the absorption (left panel) and attenuation data (right panel) near the surface in Fig. 7 as well as the spectral reflectance just below the surface in Fig. 8 for all the 42 stations. A particular interesting case where a strong brown tide occurred can be seen in station CB6. To demonstrate its unique features, the corresponding optical data has been singled out by thicker solid lines with brown color in these graphs.

In general, the measured IOP and AOP data exhibits large variability in space across the Chesapeake Bay area. The absorption curves decrease sharply with longer wavelength as CDOM absorption is dominant in blue region and have a local peak around 675nm due to chlorophyll absorption. The spectral dependence of the total water absorption changes from cases which CDOM dominant with barely no featured chlorophyll absorption local peaks to cases where chlorophyll is the dominant mechanism (such as the brown tide case). The value of a(400) varies from 1.7 to 10 m^{-1} while the attenuation coefficients range from less than 5 m^{-1} to more than 30 m^{-1}, indicating the presence of highly variable non-algal particles. The reflectance of the brown tide case is small and shows a strong local peak in the NIR region. On the other hand, in some of the other stations, the large amount of inorganic particles raises the upwelling radiance signal greatly which almost masks the features in NIR region.

The typical LSQ fitting results are displayed in Fig.9 together with the experimental data. The fitted correction factor ε of scattering lies in the range of 0.15-0.2 which is reasonable compared with manufacturer recommended value of 0.14-0.18. The value of s is in the range of 0.011-0.015 which is also consistent with the commonly used value 0.014. Assuming a Junge distribution for the size distribution of the particulates, the fitted values of γ from 0.8 to 1.2 should result in values of ζ from 3.8-4.2. The chlorophyll concentration obtained from the fitting is plotted vs. that from the fluorescence channel in Fig. 10 for one of the stations. The solid line represents the unit slope case (y=x). The fitted C_{chl} highly correlates with the profiler measurements but with approximately double the values that of fluorescence measurements. This may be caused by either an inaccurate calibration factor used for the fluorescence measurement or the normalized chlorophyll spectral absorption used in the fitting process may not be appropriate for the algae species in the Chesapeake Bay area. To solve this issue, a careful calibration according to the detailed analysis of planktonic community in this area is needed to determine the absolute value of C_{chl}. Despite this calibration issue, we can still use the retrieved C_{chl} either from spectral fitting or from fluorescence measurements for comparative purposes.

For example, Fig. 11 shows the vertical profile of the measured chlorophyll concentration for four different stations. The chlorophyll concentration drops sharply for deeper water which is reasonable since higher C_{chl} indicates more phytoplankton nutrition near the surface, where rich sun light is available [10]. The spectral absorption by algae cells can be obtained by subtracting the fitted absorption of yellow substance from the total absorption value. Fig. 12 displays the spectral

absorption by algae normalized at 440nm for all the 42 stations. Even though the general features are similar to the typical spectral absorption of the major pigment, chlorophyll a, the spectra still show significant variability. The non-uniform distribution of chlorophyll inside the algae cells and other existing pigments such as chlorophyll b or c are responsible for the various ratios at the two absorption peaks at 440nm and 665nm as well as the third absorption peak around 630nm. For these two reasons, the spectral absorption of algae varies also from species to species.

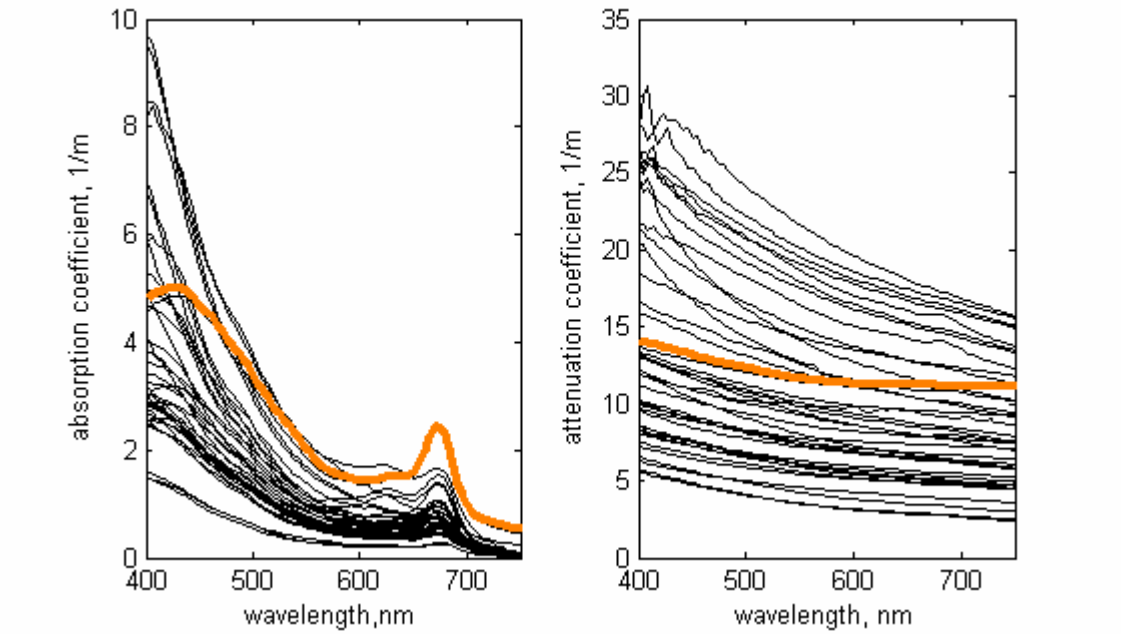

Figure 7 Measured absorption coefficient (left panel) and attenuation coefficients (right panel) versus wavelength near water surface for all the 42 stations. The thick brown line represents the brown tide case

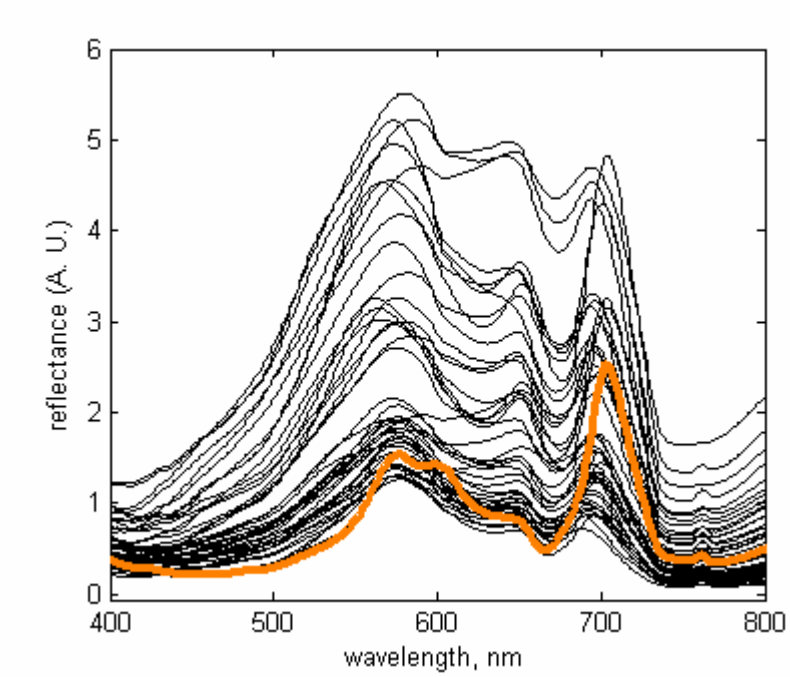

Figure 8 Measured spectral reflectance just below surface for all the 42 stations. The thick brown line represents the brown tide case

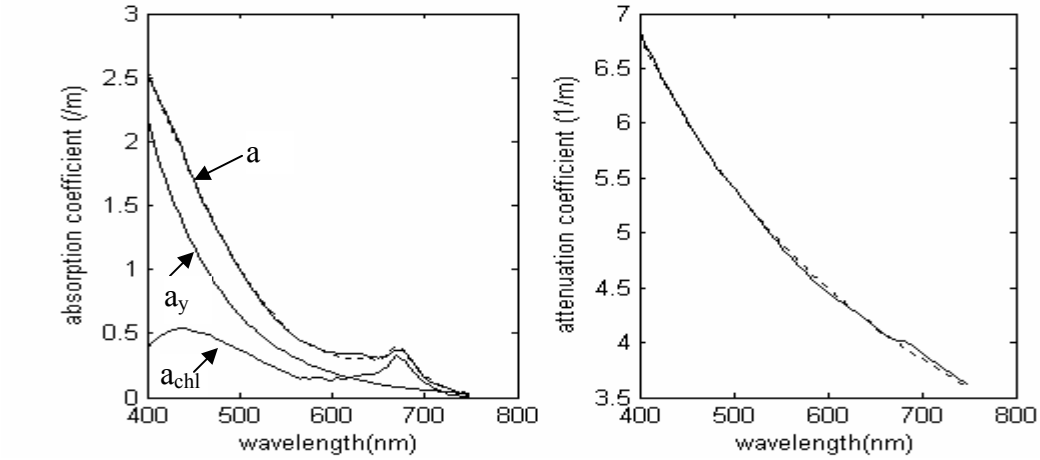

Figure 9 Typical fitting results for absorption (left) and attenuation (right): solid, measured data; dashed line, fitted spectrum

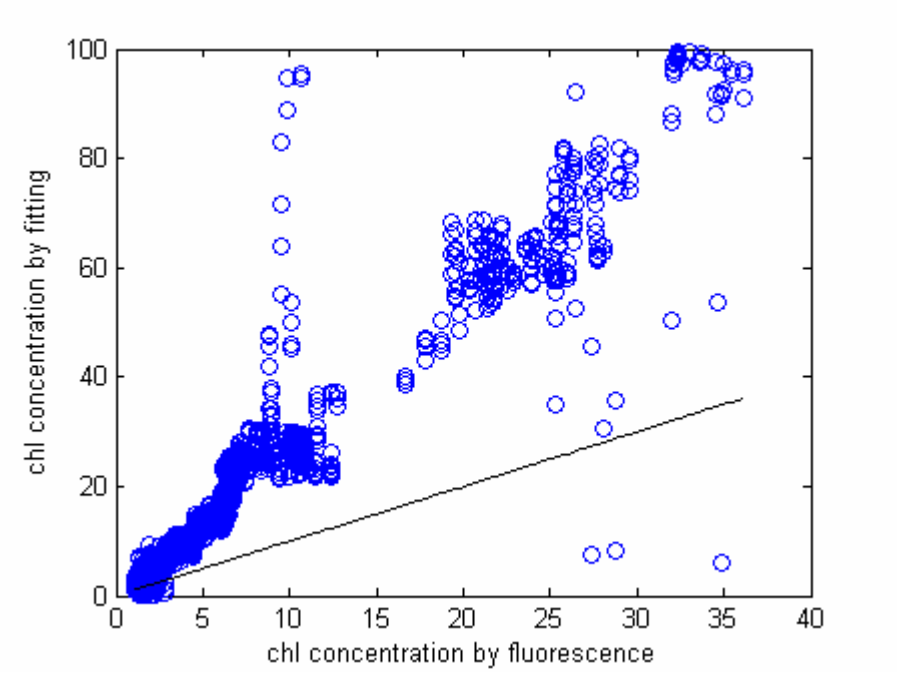

Figure 10 Chl concentration by fitting versus chl concentration by fluorescence measurement; solid line represents the unit slop (y=x)

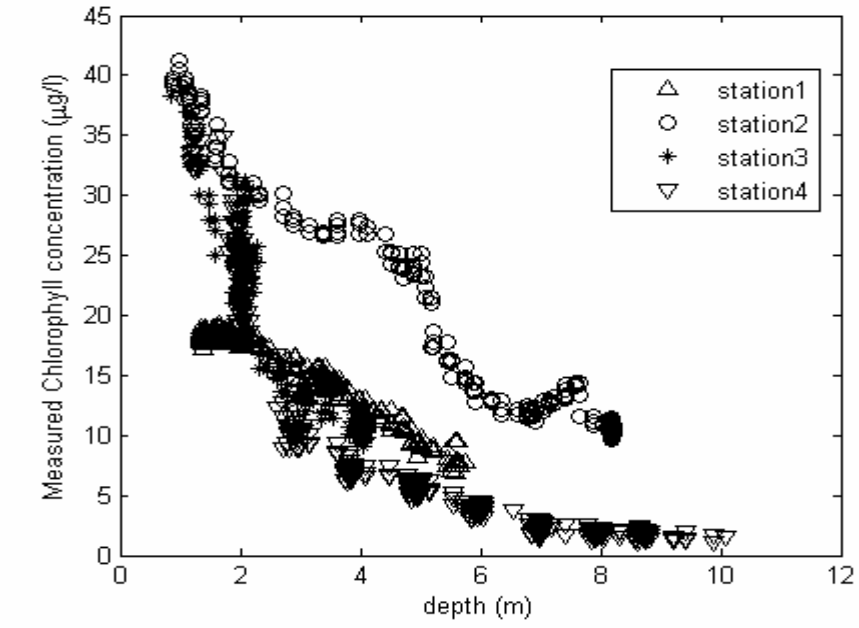

Figure 11 Measured Chl concentration as a function of depth for 4 different stations

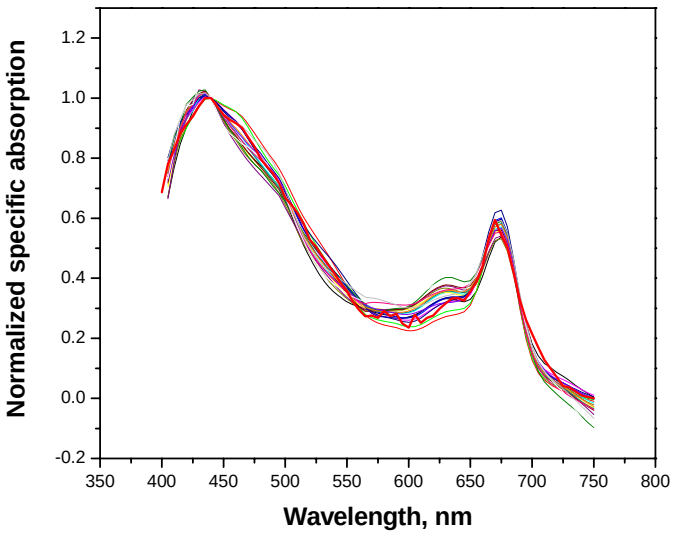

Figure 12 Spectral absorption by algae normalized at 440nm at all 42 stations

2.6 Summary and Conclusion

A comprehensive database of water IOP and AOP in the Chesapeake Bay area was generated by in-situ optical measurement during the summer cruise 2005. This includes the spectral absorption and attenuation coefficient at 81 wavelengths from 400nm to 800nm, volume scattering at 117˚ at 7 visible wavelength channels as well as CDOM and chlorophyll concentration by excited fluorescence and spectral reflectance measurements. Through parameterization a 4-component and 2-component model were used to fit the measured a(λ) and c(λ) successfully by LSQ method. The fitted results for the spectral shaping factors such as s and γ fall into the range of commonly used values in other reference. The nearly constant ratio in chlorophyll concentration between the fitted and measured ones results from the

discrepancy in calibration which is algae species dependent. The spatial diversity of water constituents in coastal area leads to large dynamic range in all the measured optical properties of local coastal water.

Reference*:*

1. C. D. Mobley, "Light and Water: Radiative Transfer in Natural Waters", Academic Press, New York, 1994

2. C. S. Roesler, M. J. Perry, "In situ phytoplankton absorption, fluorescence emission and particulate spectra determined from reflectance", J. Geoph. Res. Vol. 100, 13279-13294 (1995)

3. B. Hamre, O. Frette, S. R. Erga, J. J. Stamnes and K. Stamnes, "Paramterization and analysis of the optical absorption and scattering coefficients in a western Norwegian fjord: a case II water study", Appl. Opt. 42, 883-892 (2003)

4. G. Chang, K. Mahoney, A. Briggs-Whitmire, D.D.R. Kohler, C.D. Mobley, M. Lewis, M.A. Moline, E. Boss, M. Kim, W. Philpot, and T.D. Dickey, "The New Age of Hyperspectral Oceanography", Oceanography, Vol. 17, 16-23 (2004)

5. T.D. Dickey, "Studeis of Coastal Ocean Dynamics and Processes Using Emerging Technologies", Oceanography, Vol. 17, 10-13 (2004)

6. Van de Hulst, "Light Scattering by Small Particles", Dover Publications, 1981

7. K. Carder1, F. Chen1, J. Cannizzaro1, J. Campbell, "Performance of MODIS Semi-Analytic Ocean-Color Algorithms: Chlorophyll a, Absorption Coefficients, and Absorbed Radiation by Phytoplankton (ARP)", poster

8. Wetlabs instrument manual

9. M. S. Twardowski, E. Boss, J. B. Macdonald, W. Scott Pegau, A. H. Barnard and J. V. Zaneveld, "A model for estimating bulk refractive index from the optical backscattering ratio and the implications for understanding particle composition in case I and case II waters", J. Geoph. Res. Vol. 106, 14129-14142 (2001)

10. M. Stramska and D. Stramski, "Effects of a nonuniform vertical profile of chlorophyll concentration on remote-sensing reflectance of ocean", Appl. Opt., 1735-1747(2005)

Chapter 3 Polarization Discrimination Technique to Extract Chlorophyll Fluorescence from Reflectance Spectra of Algae Contained Water

3.1 Abstract

A technique is described here in which the polarization properties of elastically scattered light and the unpolarized nature of excited fluorescence are utilized to extract the white light induced chlorophyll fluorescence component from the reflectance spectra of algae contained in sea water. This technique was successfully applied to measurements on four types of algae of different sizes and shapes in the laboratory, with both polarized and unpolarized illumination sources, and, with in some cases, the addition of different concentrations of clay, and to in-situ field measurements in eastern Long Island.

3.2 Introduction

Separating the fluorescence and elastic scatter/reflection components of fluorescing materials illuminated by white light (or sunlight) is of great interest for a variety of environmental, remote sensing, medical diagnostics, and colorimetry applications. These include: the study of upwelling radiation from algae in sea water, where the magnitude of the fluorescence peak can be considered a measure of chlorophyll concentration and photosynthetic activity, and the examination of coral reefs containing fluorescing pigments [1-4]. Separation of fluorescence and elastic scatter under white light illumination has been approached by a variety of techniques. Dual monochromator techniques utilize sources and detectors selectively tuned in tandem over appropriate spectral ranges to measure true elastic reflectance [5]. By

using long pass filters to block the fluorescence excitation wavelength, the fluorescence signal of coral reefs can be separated from reflectance by comparing the reflectance spectrum with and without a long pass filter [1]. Polarization methods have also been widely used alone and in combination with different methods for the improvement of the image visibility and separation of single from scattering in turbid media [6-10].

In this chapter, the new polarization discrimination technique recently developed by us [11] is presented. This technique makes use of the polarization properties of elastically scattered light and the unpolarized nature of excited fluorescence to separate the two components and thus extract the fluorescence component from the total reflectance spectra of algae in sea water illuminated by white light, including sunlight. The validity of the technique is confirmed by the excellent match between the spectral shape of fluorescence extracted in this manner and laser induced fluorescence of the same species. We show that the polarization discrimination technique was successfully applied to fluorescence extraction on four types of algae of different sizes and shapes in the laboratory, with both polarized and unpolarized illumination sources as well as with sunlight and, with in some cases, the addition of different concentrations of clay, and to in-situ field measurements in eastern Long Island. Based on Mie theory, this technique is shown to be generally effective for extraction of the chlorophyll fluorescence in the 685 nm region from reflectance of algae contained water dominated by chlorophyll pigments. We also report the results of preliminary examination of the impact of surface roughness on the efficacy of the technique for measurements above and below the surface. The

technique is applicable to many situations of practical interest, with both polarized and unpolarized light sources, making it applicable for passive remote sensing diagnostics with natural sunlight illumination.

3.3 Polarization Discrimination Technique

The essential principal of the technique is based on the fact that light elastically scattered by the phytoplankton particles in water in any given direction will generally show a certain degree of polarization when illuminated by white light, depending on the polarization and geometrical configuration of the illumination, whereas excited fluorescence radiates uniformly into the 4π stradians without any polarization. This is also true for unpolarized light illumination, except for 180 degree backscatter or 0 degree forward scatter. Thus if a polarizer is placed in front of a detector to collect the scattered light, rotation of this polarizer will cause the detected light to vary from a minimum to a maximum depending on the polarization of the scattered light. The respective spectra for maximum and minimum detected light, $R_{\max}(\lambda)$ and $R_{\min}(\lambda)$ obtained by rotating the polarizer consist of $R_{\parallel}(\lambda)$ and $R_{\perp}(\lambda)$, the components of elastic scattering parallel and perpendicular to the scattering plane respectively, plus half of the fluorescence $0.5Fl(\lambda)$ spectra due to the chlorophyll pigments in algae cells (with a peak at 685 nm and a full width at half maximum of 25 nm), which remains unchanged as the detector is rotated. These maximum and minimum detected signals can be expressed as:

$$R_{\max}(\lambda) = R_{\perp}(\lambda) + 0.5Fl(\lambda), \tag{1}$$

$$R_{\min}(\lambda) = R_{\parallel}(\lambda) + 0.5Fl(\lambda). \tag{2}$$

The total signal $R(\lambda)$, is then given by

$$R(\lambda) = R_{\max}(\lambda) + R_{\min}(\lambda) = R_{\perp}(\lambda) + R_{\parallel}(\lambda) + Fl(\lambda) \quad (3)$$

and the total elastically scattered component is given by

$$R_s(\lambda) = R_{\perp}(\lambda) + R_{\parallel}(\lambda). \quad (4)$$

We will next examine how these relationships can be used to separate and extract the fluorescence component from the total signal, and hence separate the fluorescent and elastically scattered components.

To facilitate the discussion, we first examine the ideal case when the incident light is perpendicular to the scattering plane formed by the axis of illumination and detection. According to single scattering Mie theory, the elastically scattered light will retain the polarization of the incident light relative to the scattering plane. The cross polarized component $R_{\parallel}(\lambda)$ will be zero when any depolarization caused by the finite numerical aperture, collection geometry limitations and departures from spherical shape of the algae cells is neglected. Then eq. (2) reduces to:

$$Fl(\lambda) \approx 2R_{\min}(\lambda). \quad (5)$$

We can obtain the total elastically scattered component $R_s(\lambda)$ by subtracting the fluorescence $Fl(\lambda)$ from the total reflectance, thus,

$$R_S(\lambda) = R_{\perp} = R(\lambda) - Fl(\lambda). \quad (6)$$

In the case of polarized illumination, $R_s(\lambda)$ is the elastically scattered light polarized in the direction perpendicular to the scattering plane.

We now consider the more general case where the scattering signal is partially polarized. This usually happens for unpolarized illumination (complete forward and

backscatter cases are excluded). The degree of the polarization depends on the illumination and detection geometries as well as the shape of the algae particles. Then both of the polarization components $R_{//}(\lambda)$ and $R_{\perp}(\lambda)$ in eq. (3) will exist. In this case, subtraction of (1) and (2) removes fluorescence signal leaving the difference of two polarized scatter components:

$$R_D = R_{\perp} - R_{//} \tag{7}$$

It has been found in both experiments and simulation that the elastic scattering R and R_D are linearly correlated throughout the spectral range outside the fluorescence spectral region. Taking advantage of this, a linear regression is performed to fit the function $R_D(\lambda)$ outside the fluorescence spectral region into $R_s(\lambda)$ (identical to R(λ)) then:

$$R_s = A \times R_D + B \tag{8}$$

This linear relation is next extended into the fluorescence spectral region to estimate the scattering component $R_s(\lambda)$ in that region. The fluorescence Fl can then be obtained by subtracting the estimated scattering signal R_s from the total reflectance R:

$$Fl(\lambda) = R(\lambda) - R_s(\lambda) \tag{9}$$

The validity of the near linearity assumption between $R_D(\lambda)$ and $R_s(\lambda)$ appears borne out by experimental results and can be understood in terms of the simulation model described later for scattering by particles with complex refractive index where the real part n' relative to the water is small (less than 1.06 for algae cells) and the elastic scattering process is dominated by the imaginary, absorptive part, and hence largely independent of polarization. Under these conditions, the spectral dependence of both

$R_{\parallel}(\lambda)$ and $R_{\perp}(\lambda)$ will be essentially the same, and the two will be linearly related. This near linearity assumption between $R_{\parallel}(\lambda)$ and $R_{\perp}(\lambda)$ also leads to the following relationship

$$R_{max}(\lambda) - 0.5\,Fl(\lambda) = (R_{min}(\lambda) - 0.5\,Fl(\lambda))A_1 + B_1, \quad (10)$$

where A_1 and B_1 are regression parameters obtained in fitting $R_{\parallel}(\lambda)$ into $R_{\perp}(\lambda)$ in the spectral zones outside the fluorescence region. This gives another expression for the fluorescence component:

$$Fl(\lambda) = 2(A_1 R_{min}(\lambda) + B_1 - R_{max}(\lambda))/(A_1-1). \quad (11)$$

In practice, factors such as a finite numerical aperture and non-spherical shape of algae particles result in depolarization in the scattered light detected. There are always small residual values of $R_{\parallel}(\lambda)$ for polarized illumination. Then the same procedure described above can be also applied to estimate the elastic scattering signal and separate the fluorescence from the total reflectance signals.

3.4 Experiments

3.4.1 Experimental set-up

Experiments were carried out with both polarized and unpolarized light sources, including sun light, in the laboratory. The basic experimental set-up is that shown in Figure 1. White light from a 150 W EKE lamp in PL-900 Dolan Jenner illuminator or from a 150 W quartz halogen lamp in a Cuda Corp. illuminator is used to illuminate curvette C containing algae in sea water through an optical fiber fitted with a collimating lens, and an optional polarizer, P1 (used in some of the experiments for polarized illumination). The test sample is illuminated at different

angles i_1 directly (Fig. 1b) or through clear glass on the side of the curvette (Fig. 1a) when the incident angle $i_1=90^o$. All other side and bottom surfaces of the curvette are covered with black tape to minimize spurious reflections. The elastically scattered and fluorescence signals are collected by a fiber optic probe (multimode fiber with 200-μm core diameter and NA=0.22) and coupled into a SQ-2000 spectrometer(Ocean Optics). The fiber probe is installed vertically above the surface of the water (Fig.1a) or at the angle i_2 to the vertical direction (Fig. 1b). A rotatable polarizer P2 is placed in front of the probe. All measured spectra were referenced to a Spectralon reflector from Labsphere.

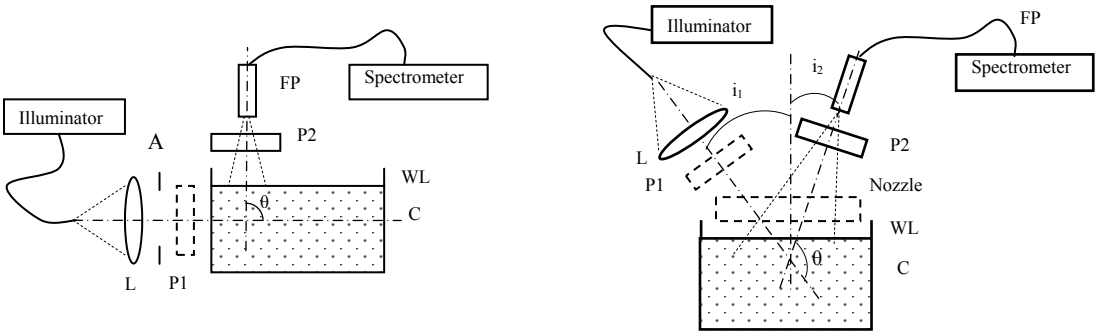

Figure 1 Experimental set-up: a- $i_1 = 90°$, $i_2 = 0$. L – lens, FP – fiber probe, A – aperture, P1, P2 – polarizer and analyzer, C – cuvette with algae, WL – water level; b- general case of illumination and detection

Four types of algae have been tested in the lab: (1) *Isochrysis sp* with largely spherical cells of approximately 5 μm diameter and a real refractive index 1.056 at 550 nm relative to water (2) Tetraselmis striata with slightly elliptical cells of approximately 12 μm diameter; (3) The algae "*Pavlova*" are close to spherical with the sizes around 10 μm (4) *Thalassiosira weissflogii*, have the shape of rectangular plates with sizes 8-10x14-18 μm. The microscopic images of these algae cells were seen in Fig.2. Their concentrations are of the order of 10^6 cells/ml. Two types of clay

were added as additional scatterers to the algae samples when examining the impact of additional scattering on the measurement, Na-Montmorillonite and Ca-Montmorillonite. Both of them have particulates with diameters in the range 2-6 μm. The concentration of clay was varied from 10 mg/L to 500 mg/L. The algae samples were obtained from Cornell's Long Island Horticultural Research and Extension Center and clays from Source Clay Minerals Repository, University of Missouri – Columbia.

Experiments were also carried out with sunlight illumination on the roof of the CCNY building with cultured algae, and are discussed section 3.4.4.

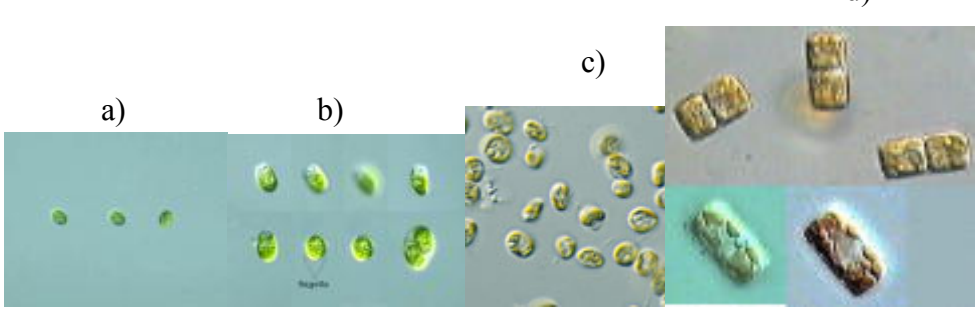

Figure 2 The microscopic images of the four types of algae used in the experiment: a) *Isochrysis sp* b) *Tetraselmis* c) *Pavlova* d) *Thalassiosira weissflogii*

3.4.2 Polarized illumination

Experiments were first carried out with the polarizer P1 oriented to pass horizontally polarized light, which in the context of the experimental set-up shown in Fig.1a, is perpendicular to the scattering plane. The probe is positioned vertically and the incident light path is normal to the detection path (i_1=90˚ and i_2=0˚). The detected elastic scatter component varied from a maximum, when the optical axis of P2 is parallel to the incident polarization, to essentially zero for the cross polarized direction, while detected fluorescence signal is unchanged with any rotation of the polarizer. Fig.3 shows the respective spectra for maximum and minimum detected

light signal, $R_{\max}(\lambda)$ and $R_{\min}(\lambda)$. If the scattering is truly due to spherical particles, $R_{\|}(\lambda)$ should be zero no matter what scattering angle is, and $R_{\min}(\lambda)$ will be half of the fluorescence only. Actually when $R_{\min}(\lambda)$ was compared with the fluorescence spectrum $Fl(\lambda)_{laser}$ of the same algae obtained using laser excitation at 488 nm (the $Fl(\lambda)_{laser}$ showed no polarization), the two spectra, $R_{\min}(\lambda)$ and $Fl(\lambda)_{laser}$ matched reasonably well.

However, the finite numerical aperture, collection geometry limitations and departures from sphericity of the algae will result in a small background depolarizatio $R_{\|}(\lambda)$, which is evident in the $R_{\min}(\lambda)$ of Fig. 3a outside the fluorescence band. In order to remove this background, linear regression was performed to fit the function $R_D(\lambda)$ in the 450 - 650 nm range (outside the fluorescence spectral region) into $R(\lambda)$. The regression parameters were then used to calculate the scattering component according eq. (8) for the whole wavelength range 450 – 750 nm. The fluorescence $Fl(\lambda)$ component in the total spectrum $R(\lambda)$ can then be obtained from equation (9).

The spectra $R(\lambda), R_D(\lambda), R_s(\lambda)$ and $Fl(\lambda)$ obtained in this manner are shown in Fig.3b. $Fl(\lambda)$ is an exact fit and undistinguishable from the normalized laser induced fluorescence spectra $Fl(\lambda)_{laser}$. It should be noted that the two-polarizer approach would be applicable to any scattering angle θ, up to 180 degrees (backscattering mode), since the elastically scattered light retains the incident polarization (in the single scattering limit), and a cross-polarizer on the detector would permit discrimination between it and any fluorescence.

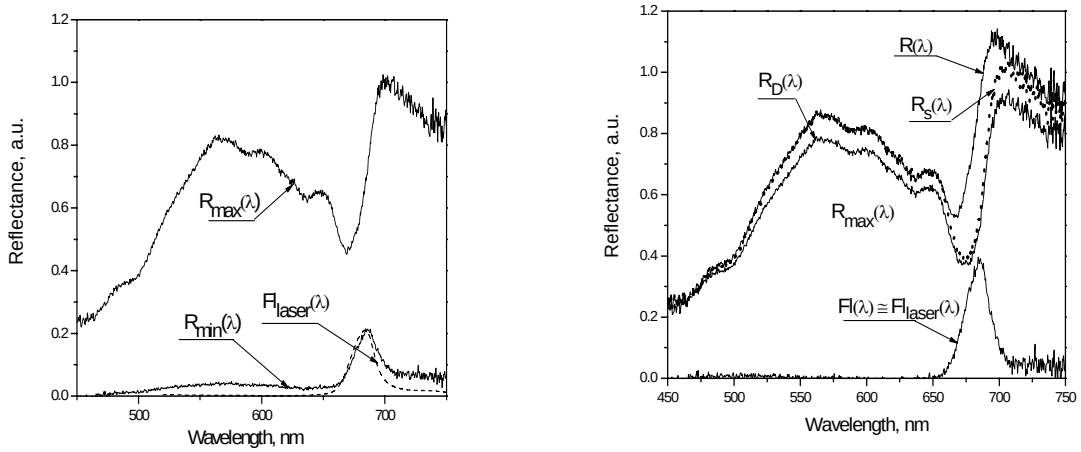

Figure 3 Measured spectra for algae Isochrysis sp with two polarizers: P1 installed, sample is illuminated by horizontally polarized light (i_1 =90˚ and i_2 =0˚)

3.4.3 Unpolarized illumination

Without the polarizer P1, the illuminating light contains equal amount of vertical as well as horizontal polarizations, which results in a significant non-zero component $R_{\|}(\lambda)$ in the scattering signals. The experimental results $R_{\max}(\lambda)$ and $R_{\min}(\lambda)$ without the first polarizer P1 in place are shown for *Isochrysis sp* in Fig. 4a, together with the spectra $R(\lambda)$, $R_s(\lambda)$ and $Fl(\lambda)$ obtained by the same linear regression procedure. Comparison of the spectra $R(\lambda)$ and $Fl(\lambda)$ with one polarizer and two polarizers shows that despite significant difference in the scattering spectra by the algae cells illuminated by unpolarized and horizontally polarized light, the magnitude and spectral distribution of fluorescence (normalized to the appropriate intensity of the incident light) obtained from the fitting procedures are found to be approximately the same. Similar results for the extraction of fluorescence for another algae species Tetraselmis striata are shown in Fig. 4b. Applying the linear fitting method to

estimate the scattering component in the reflectance spectra of the algae *Thalassiosira weissflogii* and *pavlova* chlorophyll fluorescence was also successfully extracted from the total reflectance signal for both a polarized source (2 polarizers) and an unpolarized source (1 polarizer before the detector), as seen in Fig. 5 and 6, despite the fact that the shape of the algae particles *Thalassiosira weissflogii* is far from spherical.

The success of the fluorescence separation from the lab measured reflectance spectra for different types of algae with different sizes and shapes confirms the validity of this approach and the near linear correlations for the elastically scattered spectral components of two cross polarizations.

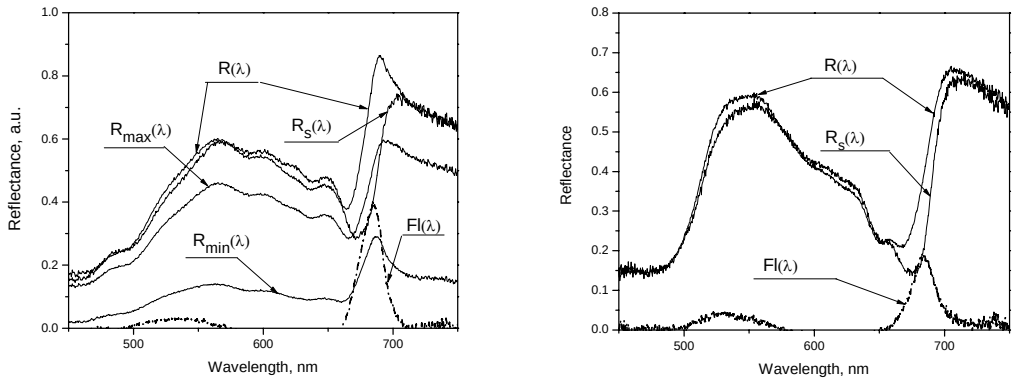

Figure 4 Measured and processed spectra for the experiments with one polarizer: (i_1 =90˚ and i_2 =0˚)

a – Algae *Isochrysis sp*, diameter of particles ≈ 5 μm
b - Algae Tetraselmis striata, diameter of particles ≈ 12 μm

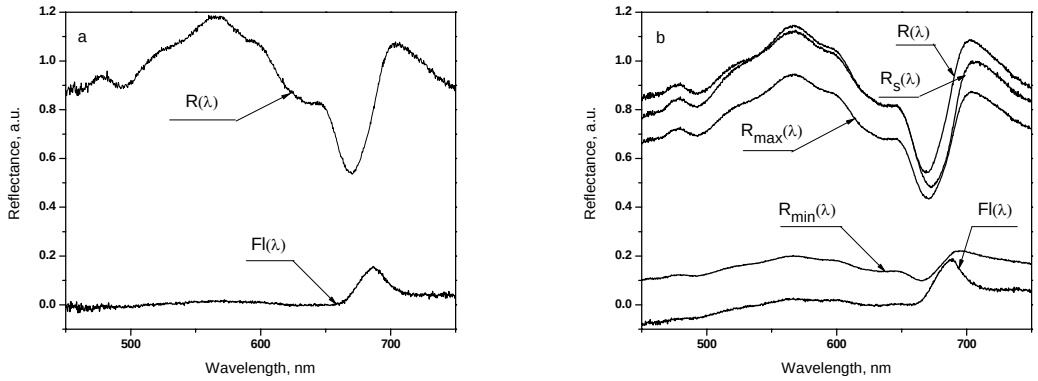

Figure 5 Measured and processed spectra for the experiments with the algae *Thalassiosira weissflogii*: a – polarized light source, b – unpolarized light source. (i_1=90˚ and i_2=0˚)

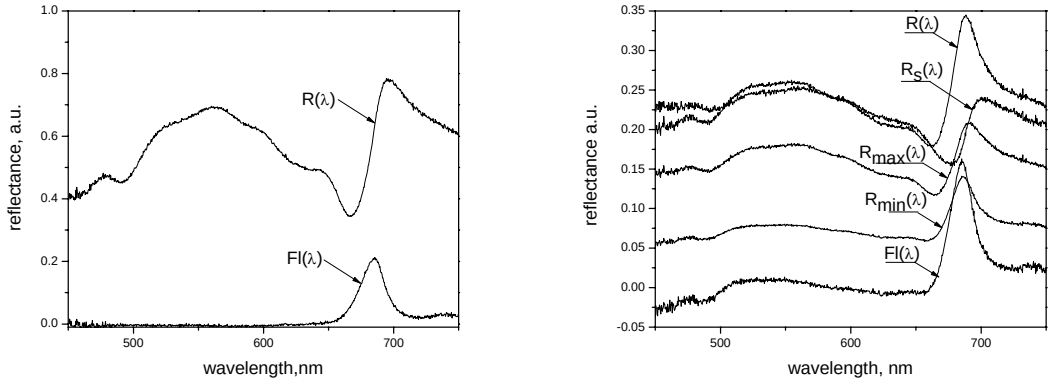

Figure 6 Measured and processed spectra for the experiments with the algae *pavlova*: a – polarized light source, b – unpolarized light source (i_1=90˚ and i_2=0˚)

3.4.4 Sunlight illumination

Experiments with natural sunlight illumination were performed on the roof of the CCNY building with cultured algae sample. The reflected signal was collected through a fiber probe (NA=0.22) and detected using a GER 1500 spectroradiometer (which was also used for the field measurements discussed in section 3.5).

As shown in Fig. 7, measurements were conducted with a solar zenith angle of 50 degrees (scattering angle $\theta = 130^o$) with only one polarizer in front of the probe,

which was in vertically oriented. As expected, retrieved fluorescence agrees with that obtained by laser excitation.

Reflectance spectra were recorded for different types of algae, at different sun angles and viewing angles (between the vertical and the axis of the detector). When specular reflection is avoided, for sun angles from 30 to 50 degrees from zenith and for viewing angles 0-20 degrees we were able to successfully extract fluorescence using only one polarizer, in front of the detector. In the Fig. 8 there is another example of the fluorescence extraction with sunlight illumination. The fluorescence was reliably detected despite very small differences between the signals with 2 different orientation of polarizer $R_{\max}(\lambda)$ and $R_{\min}(\lambda)$.

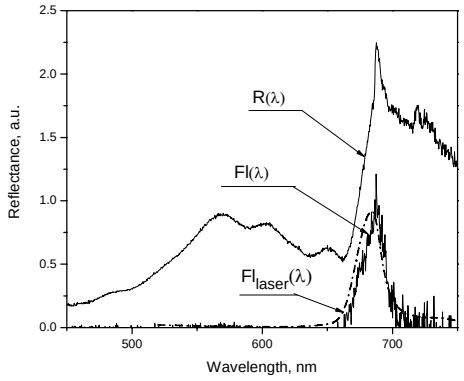

Figure 7 Experiments with sun light illumination (Solar zenith angle 50°), Algae *Isochrysis*

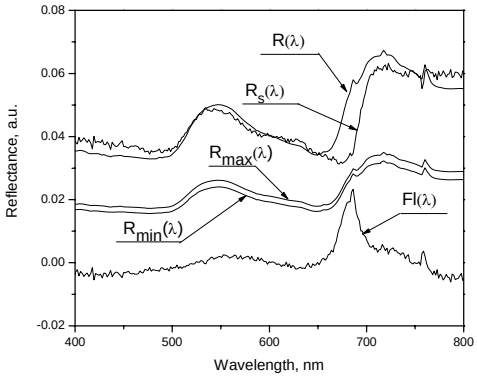

Figure 8 Extraction of fluorescence with sunlight illumination. Algae *Tetraselmis striata*, 04/29/04 at 12 pm, sun was at 29 degrees from zenith, detector was in the vertical position

3.4.5 Experiments with different angles of illumination

We also tested efficacy of the fluorescence extraction for different angles of illumination i_1 with the detection probe in the vertical position, for polarized and unpolarized light sources. Fig.9 shows that for polarized light, determination of fluorescence is reliable for the whole range of incident angles up to 70^o. While the amplitudes of the reflectance curves and the magnitudes of the local peaks in the NIR spectral region are different due to the variation in the intersected volumes of illumination and detection, the shape of the extracted fluorescence is the same with a peak at 685 nm and nearly zero outside the fluorescence zone. Extraction of fluorescence for unpolarized light is less accurate but still possible for angles of illumination up to $i_1 = 45^o$ as shown in Fig.10.

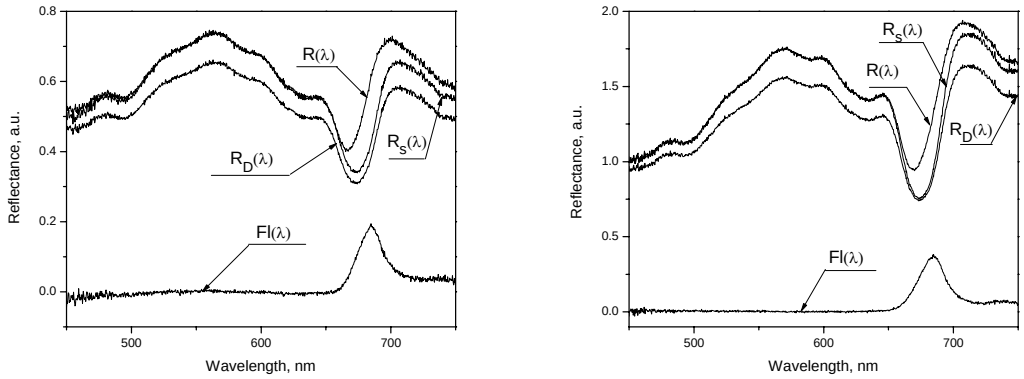

Figure 9 Spectra for the experiments with polarized light, different angles of illumination, algae *Isochrysis* (diameter d ≈ 5μm): a – i_1= 30°; b – i_1= 70°.

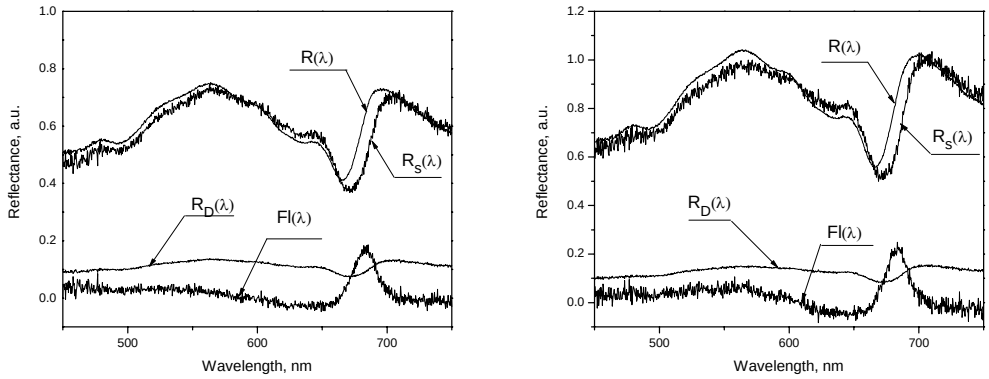

Figure 10 Spectra for the experiments with unpolarized white light, different angles of illumination, algae *Isochrysis* (diameter d ≈ 5 μm): a – i_1= 30°; b – i_1= 40°.

3.4.6 Dilution Experiments

Fig. 11 shows the fluorescence curves extracted at various algae concentrations, using unpolarized illumination. The extracted fluorescence was proportional to concentration of algae as the test samples were diluted down to as low as 1/250 of the original concentration (corresponding to less than 1 μg/l. and not shown on the graph because of the too small value).

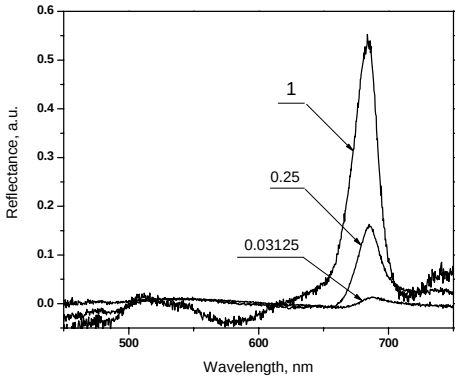

Figure 11 Fluorescence extracted in the 1 polarizer setup for different concentrations of algae *Pavlova.* Numbers on the graph are relative concentrations.

The magnitude of extracted fluorescence in the dilution experiments are combined in Fig. 12 for both unpolarized and polarized incident light using 2 types of algae. Concentrations and fluorescence magnitudes are normalized respectively to the original concentration of algae and fluorescence magnitude at this concentration. While the curves show some saturation at the high concentrations due to reabsorption of fluorescence, they are very close to each other for both polarized and unpolarized sources. Similar results have been obtained for the other types of algae.

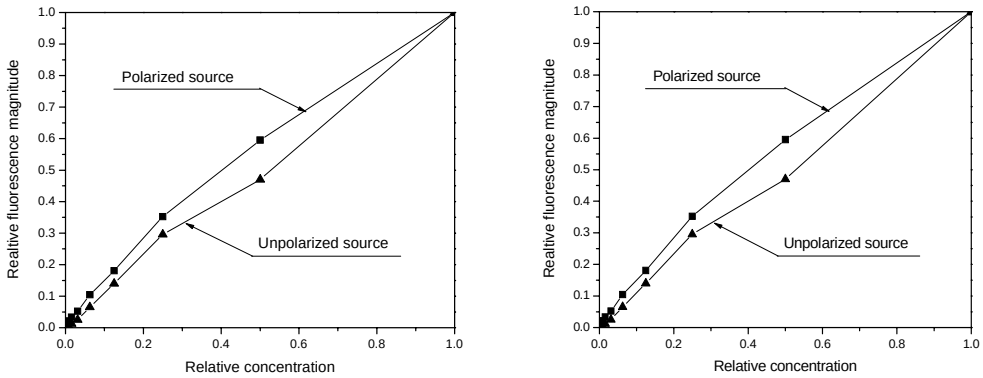

Figure 12 Extraction of fluorescence magnitude for different concentrations of algae *Pavlova* (left) and *Tetraselmis striata* (right) for polarized and unpolarized light sources

3.4.7 Algae with clay

To examine the impact of additional scattering on the efficacy of the polarization discrimination technique, clay particles were added to a constant concentration of algae in seawater. Clay particles as additional scatterers lead to both an increase of scattering/reflections amplitude and a change of the shape of the total scattering/reflectance spectra. Scattering and fluorescence from the mixture was investigated using both polarized and unpolarized light sources. With clay concentrations ranging from 10 mg/L to 500 mg/L the fluorescence magnitude and shape extracted by the technique remained almost the same as that without clay particles. There were no significant differences in results in using the technique with either 2 polarizers or 1 polarizer. Fig. 13 shows the total scatter/fluorescence signal, $R(\lambda)$, obtained for different concentrations of clay while keeping the algae concentration constant. Comparison of extracted fluorescence for pure algae and for the algae samples with high concentration of clay are also shown in Fig. 13. It is interesting to note that even at the high clay concentrations, in the multiple scattering regime, the extracted fluorescence was still a very good match with the pure algae case, confirming applicability of the technique in these conditions.

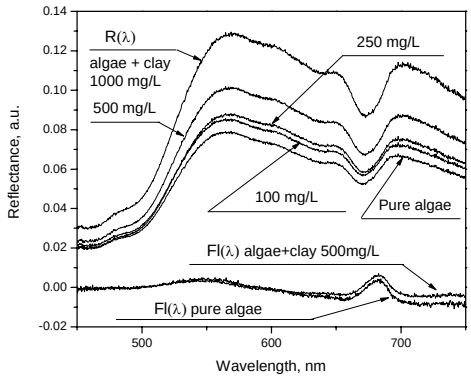

Figure 13 Reflectance curves and extracted fluorescence for different concentrations of clay with the algae. Algae *Isochrysis sp*, clay Na-Montmorillonite

3.5 Field measurements

Field measurements were conducted in the coastal area of Shinnecock Bay, Long Island, NY in June 2004. Chlorophyll concentrations were measured by a Sea Tech fluorometer. Reflectance was measured by a GER 1500 spectroradiometer for different sun angles by placing the fiber optic probe in the vertical position. A polarizer in front of the probe was oriented with its optical transmission direction in and perpendicular to the scattering plane formed by the axes of illumination and detection. Examples of extracted fluorescence are shown in Fig. 14. Spectra were recorded at approximately 8:30 am when sun was at 61 degrees from the zenith. Chlorophyll concentration was approximately 8μg/l.

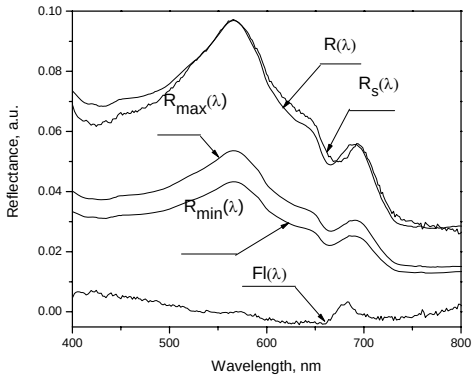

Figure 14 Measured and processed spectra for the measurements in Shinnecock Bay

3.6 Simple scattering model

As previously discussed, the accuracy of the polarization technique depends on the linearity between $R_D(\lambda)$ and $R_s(\lambda)$ or between $R_{\max}(\lambda)$ and $R_{\min}(\lambda)$. To explore this condition, we developed a simulation model based on Mie scattering theory [13] valid for spherical scatterers to simulate our experimental conditions. A Gaussian size distribution of algae was used with a mean radius 2.5 μm, and a standard deviation σ = 0.5 μm. To obtain the imaginary part of the refractive index, n'' for algae cells and the related absorption coefficient $\gamma = 4\pi n''/\lambda$, we used a statistically derived dimensionless chlorophyll-specific absorption coefficient over the wavelength range from 400 nm to 700 nm from [15] together with $n'' = 0.007673$ (relative to water) for the *Isochrysis sp.* at 440 nm [12]. The real part of the refractive index n' was derived using the Kramers-Kronig relationship by decomposition of the absorption coefficient wavelength dependence into 2 dominant single oscillators with Lorentzian shapes [15], using $n' = 1.056$ (relative to water) at 550 nm as an input [12]. The simulation provides values for the perpendicular $S_{\max}(\lambda)$ and parallel

$S_{\min}(\lambda)$ scattering components. To compare those to the experimentally observed $R_{\max}(\lambda)$ and $R_{\min}(\lambda)$, it is necessary to adjust them for extinction and also to add an appropriate fluorescence term based on laser excitation results. The extinction process is a combination of the following: (i) absorption of pure water [16], (ii) the total algae extinction spectrum derived using Mie scattering theory for the above mentioned particle size distribution and complex refractive index and (iii) absorption of yellow substance calculated using an empirical formula from [16]. The $S^{A}_{\max}(\lambda)$ and $S^{A}_{\min}(\lambda)$ are the extinction adjusted spectra with addition of fluorescence signal to simulate experimental spectra $R_{\max}(\lambda)$ and $R_{\min}(\lambda)$ for both θ = 90^{o} and θ = 130^{o} scattering angles.

Simulation spectra of perpendicular $S^{A}_{\max}(\lambda)$ and parallel $S^{A}_{\min}(\lambda)$ components at θ = 90o are compared in Fig.15b with the experimental spectra $R_{\max}(\lambda)$ and $R_{\min}(\lambda)$ obtained with one polarizer. Comparison shows good agreement for perpendicular components $S^{A}_{\max}(\lambda)$ and $R_{\max}(\lambda)$. Less consistent agreement between $S^{A}_{\min}(\lambda)$ and $R_{\min}(\lambda)$ has been already previously noted [17].

To examine the range applicability of the method, numerical simulations were carried out for different scattering angles and refractive indices. Since we are mainly interested in the behavior of signal ratios, extinction corrections, which are the same for $S_{\min}$ and $S_{\max}$, can be removed. Analysis of $(S_{\max} - S_{\min})$ and $(S_{\max} + S_{\min})$ for the wavelengths between 450 nm and 750 nm indicated that there is a good linear correlation between them and consequently extraction of fluorescence is accurate enough for the particles diameters of up to 12 μm and for n' = 1.06 and less. This

covers the most interesting range of parameters for algae. Fig.15a shows the linear correlation coefficient between $(S_{\max} - S_{\min})$ and $(S_{\max} + S_{\min})$ as a function of n' for different scattering angles. For the higher n' correlation coefficient is smaller, so extraction of fluorescence will be less accurate. These conditions set the limitations of this technique which need to be experimentally verified.

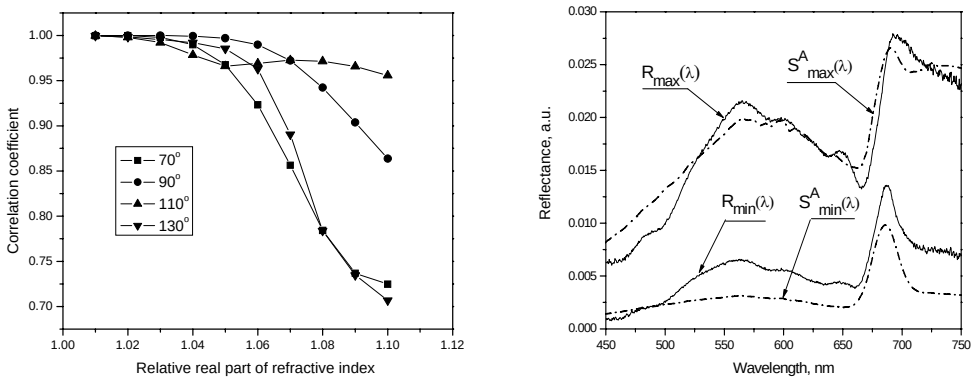

Figure 15 a - Linear correlation coefficient between (S_{max}- S_{min}) and (S_{max}+ S_{min}) for different indices of refraction and illumination angles.Mean radius = 2.5 μm, standard deviation σ = 0.5 μm.b-Comparison of experimental and calculated spectra.

3.7 Conclusion

A technique for separation of the scattering and fluorescence components in reflectance spectra based on the polarization properties of elastically scattered light and the unpolarized nature of excited fluorescence has been demonstrated for retrieving the fluorescence component from the total reflectance spectra of algae in the sea water excited by white light. The efficacy of the technique is confirmed by an excellent match between the extracted fluorescence and the laser induced fluorescence of the same species. This technique was successfully applied to measurements of four types of algae with different sizes and shapes in the laboratory, with, in some cases the addition of different concentrations of clay, and to in-situ field

measurements in eastern Long Island. It is shown to be effective for extraction of the chlorophyll fluorescence in the 685 nm region from reflectance of water containing algae dominated by chlorophyll pigments. While the use of polarized illumination increases attainable accuracies by this method, a practically useful range of applicability is also found for unpolarized white light sources. Computer simulations based on a Mie scattering model indicate limitations of the technique, which is found to be appropriate to the general range of the algae particle sizes with typically small real parts of relative refractive index.

References

1. E. Fuchs, "Separating the Fluorescence and Reflectance Components of Coral Spectra", Appl. Opt. 40 (2001) 3614-3621.

2. J.F.R. Gower, R. Doerffer, G.A. Borstad, "Interpretation of the 685nm peak in water-leaving radiance spectra in terms of fluorescence, absorption and scattering, and its observation by MERIS", Int. J. Rem. Sens. 20 (1999) 1771-1786.

3. A.A. Gitelson, Y.Z. Yacobi, D.C. Rundquist, R.Stark, L.Han, and D. Etzion. "Remote estimation of chlorophyll concentration in productive waters: Principals, algorithm development and validation", Proc. of NWQMC (Austin Texas, 2000) 149-160.

4. K.H. Szekielda, C.Gobler, B.Gross, F.Moshary, S. Ahmed, "Spectral Reflectance measurements of estuarine waters", Ocean Dynamics 53 (2003) 98-102.

5. F. Grum, Colorimetry of fluorescent materials, in Optical Radiation Measurements, vol. 2, Academic, New York, 1980, Chap. 6.

6. J.M. Schmitt, A.H. Gandjbakhche, R.F. Bonner, "Use of polarized light to discriminate short-path photons in a multiply scattering medium", Appl. Opt. 31 (1992) 6535-6546.

7. S.G. Demos, R.R.Alfano, "Temporal gating in highly scattering media by the degree of optical polarization", Opt. Lett. 21 (1996) 161-163.

8. S.P. Morgan, M.P. Khong, M.G. Somekh, "Effects of polarization state and scatterer concentration on optical imaging through scattering media", Appl. Opt. 36 (1997) 1560-1565.

9. S.P. Schilders, X.S. Gan, Min Gu, “Effect of scatterer size on microscopic imaging through turbid media based on differential polarisation-gating”, Opt. Comm. 157 (1998) 238-248.

10. A. Cunningham, P. Wood, D. McKee, “Brewster-angle measurements of sea-surface reflectance using a high resolution spectroradiometer”, J. Opt. A: Pure Apl. Opt. 4 (2002) S29-S33.

11. S. Ahmed, A. Gilerson, A. Gill, B. M. Gross, F. Moshary, J. Zhou, “ Separation of Fluorescence and Elastic Scattering from Algae in Seawater Using Polarization Discrimination”, Opt. Comm. Vol 235/1-3, (2004) , pp23-30

12. D. Stramski., A.Bricaud, A.Morel, “Modeling the Inherent Optical Properties of the Ocean Based on the Detailed Composition of the Planktonic Community”, Appl. Opt. 40 (2001) 2929-2945.

13. C.F. Bohren, D.R. Huffman, Absorption and Scattering of Light, Wiley, John & Sons, 1998.

14. L. Prieur, S. Sathyendranath, “An optical classification of coastal waters based on the specific spectral absorption curves of phytoplankton pigments, dissolved organic matter and other particulate materials”, Limnolog. Oceanogr. 26 (1981) 671-689.
15. S.Ahmed, M.A. Ali, K. Mitwally, and M. El-Massry, J. Chem. Phys. 91 (1989) 3838-3845.

16. C. D. Mobley, Light and Water. Radiative Transfer in Natural Waters, Academic Press, New York, 1994.

17. H. Volten, J.F. de Haan, J.W. Hovenier, R. Schreurs, W. Vassen, A.G. Dekker, H.J. Hoogenboom, F.Charlton, R. Wouts, Limnolog. Oceanogr. 43 (1998) 1180-1197.

Chapter 4 Modeling of the Fluorescence Separation from Ocean Reflectance Spectra using Polarization Discrimination Technique

4.1 Abstract

In order to theoretically evaluate the scope and limitations of the polarization discrimination technique in fluorescence height retrieval under various ocean conditions, computer simulations are performed over a wide range of both chlorophyll concentrations and mineral particle concentrations. Polarized radiative transfer (RT) program were used to model the polarized light in atmosphere-ocean systems and an assumed realistic level of fluorescence is superimposed onto the RT calculated elastic reflectance spectrum. In particular, we explore how the degree of linear polarization contributes to the quality of the fluorescence retrieval. The simulations show that the polarization-based fluorescence retrieval works generally well for both case I and II waters, but that it may be limited if the ocean bottom albedo and/or particularly high TSS multiple scattering contributes a major component of unpolarized water leaving radiance. They also show that the retrievals obtained by polarization discrimination are more accurate than traditional baseline methods which make use of the unpolarized reflectance spectrum. That is because the latter cannot properly decouple the affects of chlorophyll fluorescence and absorption. Furthermore, we show that the baseline fluorescence extraction method strongly overestimates fluorescence value for case 2 waters. Finally, it should be noted that the polarization properties of the reflectance spectra obtained here are also

of intrinsic interest because of their potential for constraining the remote sensing retrievals of both aerosols and hydrosols.

4.2 Introduction

The reflectance from the ocean is the water-leaving radiance/irradiance normalized to the down-welling irradiance. When sun light enters a natural water body, it changes in both amplitude and direction through wavelength dependent absorption and scattering process, which are determined by the concentrations and optical properties of the optically active constituents in the water. Part of the light makes its way back to the ocean surface and is detected by the sensors on the satellite or air-crafts. The ocean reflectance connects the input and output light field of water and is one of the few quantities that can be measured by the satellite. As such, it plays an important role in obtaining information about water constituents. Among them chlorophyll concentration is one of the most interested ocean parameters since it is a strong indicator of ocean biomass which controls the global carbon cycle and has therefore been extensively studied for the past thirty years.

Various algorithms have been developed to relate the chlorophyll concentration with the spectral reflectance. The traditional blue-green ratio has been successfully applied to satellite measurements to retrieve chlorophyll concentration in the case I waters [1], where all the other components co-vary with the concentration of the chlorophyll. But it has inherent problem when applied to case II water, where absorption of CDOM and scattering of mineral particles are significant [2-4]. Recently algorithms have begun to take advantage of the reflectance in the NIR spectral region where the influence of CDOM absorption is negligible [5-7].

Unfortunately, the reflectance in this range is complicated by the overlapping spectrum of sun-induced fluorescence and local maximum value of chlorophyll absorption [8-10]. A baseline subtraction method [11] has been used to extract the chlorophyll fluorescence from the ocean reflectance. However, simulations show that the interplay of water and chlorophyll absorption can also result in apparent spectral peak features near the fluorescence peaks (around 685nm) [12]. Other bio-optical algorithms that utilize reflectance ratios at several NIR wavelengths are based on chlorophyll absorption features only and ignore the chlorophyll fluorescence [5-7] but chlorophyll fluorescence can contribute significantly to the reflectance peak in NIR region depending on the water composition. In essence, the chlorophyll fluorescence signals contaminate the elastic reflectance spectrum thereby reducing the efficacy of the retrieval algorithms in the NIR region. Therefore, determination of the magnitude of chlorophyll fluorescence is an important step in cleaning the elastic signal before further processing. An accurate separation of fluorescence signal from the ocean reflectance spectra in the NIR band is necessary for developing more robust algorithms for constituent estimation in water.

In previous chapter, the angular differential scattering of phytoplankton with narrow size distribution, based on Mie theory, was used to explain the fluorescence extraction process of polarization discrimination technique. The analysis was limited to a single particle size distribution and one algae component. Although this model is proper for the water sample which contains only one species of phytoplankton, it is not enough to describe the complexity of the natural water body in the field measurement data. In this chapter, combining the impact of absorption and scattering

of pure water, color dissolved organic matters (CDOM or yellow substance), mineral particles and algae cells a vector radiative transfer program based on the adding/doubling method [13,14] is used to model the polarization reflectance spectra for both case I and case II waters. It utilizes optical properties of single particles for different components in natural water to solve the polarized radiative transfer equation numerically, where multiple scattering has been incorporated. By adding a fluorescence signal on top of the simulated reflectance, the retrieved fluorescence from both polarized discrimination technique and the traditional base line subtraction method were compared with the theoretical input of fluorescence strength over a large variety in concentration of chlorophyll and mineral particles.

4.3 Simulation reflectance model

The computations by vector radiative transfer code provide the complete Stokes vector set I = {I, Q, U, V} for the total upwelling radiance just above the ocean surface as well as for the water leaving radiance contribution. The polarization degree of the light field is obtained from $P_w = \sqrt{Q^2 + U^2} / I$. A homogeneously mixed layer of molecules and aerosols with an aerosol optical thickness 0.1 at λ = 500 nm was assumed for the atmosphere. The ocean layer contained 3 types of particles: phytoplankton, detritus, and minerals. A Junge distribution was assumed with the slope –4 for all 3 types of particles over a size range from 0.1 to 50 μm and real refractive indices relative to water of 1.06, 1.04 and 1.18 respectively. The scattering matrices for these particles were derived from Mie computations, and appropriate fractions of each component were used to compile the effective scattering matrix of

oceanic particulates. The underwater light absorption was modeled by the sum of absorption coefficients of pure water, phytoplankton, and detritus particles for case I waters. Absorption by CDOM and scattering of mineral particles were included in case II waters. The ocean bottom reflection albedo, assumed Lambertian, was varied from 0 to 0.5. The number concentrations of the particulate matter for case 1 waters are shown in Table 1. They were determined using particle composition in [15] with the changes of the number concentrations according to Morel [16]. It should be pointed out that this partitioning leads to an overestimation of the mineral fraction in comparison to the common values for case I waters. For case II waters, fractions were varied according to the concentrations of both chlorophyll [Chl] and mineral particles, which are discussed in Section 4.4. The ocean optical thickness was fixed at 4.6 except for the shallow-water cases in which the effect of the bottom was analyzed. The ocean surface roughness was modeled according to Cox and Munk [17] for wind speeds varying between 1.37 to 18.9 m/s. The analysis was limited to a solar zenith angle of 40° and in most cases to a nadir viewing position of the probe. This scattering geometry corresponds to an underwater light incident angle of $\theta w \approx 30°$ for direct sunlight illumination and to a corresponding underwater light single scattering angle of $\Theta w = 150°$. The probe was placed just above ocean surface.

Table 1 Number of phytoplankton, detritus and mineral particles/m^3 used in RT simulations for different [Chl] concentrations.

[Chl], mg/m^3	Phytoplankton	Detritus	Minerals	Total
0.01	1.30E+11	1.29E+13	5.24E+12	1.82E+13
0.2	2.60E+12	8.25E+13	3.36E+13	1.19E+14
5	6.50E+13	2.92E+14	1.19E+14	4.76E+14
20	2.60E+14	3.71E+14	1.51E+14	7.83E+14
40	5.20E+14	3.25E+14	1.32E+14	9.77E+14
80	1.04E+16	1.22E+14	4.95E+13	1.06E+16

4.4 Modeling of fluorescence spectra and its retrieval through polarization of reflectance spectra

Estimation of the fluorescence spectra emitted from the water for given fluorescence efficiency requires analysis of absorption of light by algae and the total absorption between λ = 400 and 675 nm, the range of which defines the transformation of photosynthetically available radiation (PAR) into photosynthetically usable radiation (PUR) as well as reabsorption of fluorescence in water [18]. The fluorescence energy is proportional to [Chl] and is represented as

$$E_{Fl} = \eta[Chl] \int_{400}^{675} (E_d(\lambda) a'_{ph}(\lambda) / a(\lambda)) d\lambda \quad , \quad (1)$$

where η is the fluorescence quantum efficiency, $E_d(\lambda)$ is the downwelling irradiance, and $a'_{ph}(\lambda)$ is the chlorophyll-specific (i.e., per unit [Chl]) absorption. After taking into account fluorescence reabsorption[12], considering only emission into upper hemisphere, and assuming η = 0.03, we modeled the fluorescence spectrum $Fl(\lambda)$ as a Gaussian shape centered at 685 nm with a FWHM of 25 nm. The area under this

shape was equal to the emitted fluorescence energy, and we normalized the Fl(λ) spectrum to the downwelling irradiance $E_d(\lambda)$.

To simulate the retrieval of the fluorescence, the fluorescence spectrum Fl(λ) was split equally and superimposed on the orthogonal components $R_{\perp}(\lambda)$ and $R_{||}(\lambda)$ derived from the radiative transfer computations of Stokes parameters I and Q for observations in the scattering plane. The reflectance components $R_{max}(\lambda)$ and $R_{min}(\lambda)$ were subsequently calculated according to Eqs. (3.1) and (3.2). The regression was performed in the chlorophyll fluorescence free spectral bands of λ = 400 to 450 nm, 600 to 650 nm and 750 to 800 nm. Note that these bands are also minimally affected by CDOM fluorescence [11,19]. The input fluorescence spectrum Fl(λ) was varied according to changes in [Chl] from 5 to 80 mg/m^3.

4.5 Results of Simulation

To test the radiative transfer model, its numerical results were compared for the irradiance ratio A just below the surface with those obtained from a general bio-optical model for case I waters. The bio-optical model values were derived from [1]

$$A(\lambda) = 0.33 b_b / a \qquad (2)$$

where

$$b_b(\lambda) = 0.5 b_w(\lambda) + \{0.002 + 0.02(0.5 - 0.25 * \log[\mathrm{Chl}])(550/\lambda)\}\{0.30[\mathrm{Chl}]^{0.62} - b_w(550)\} \qquad (3)$$

is the total backscattering coefficient[16], b_w is the pure sea water scattering coefficient, and a is total absorption coefficient which for a CDOM-free ocean is given by Morel[20]:

$$a(\lambda) = a_{\mathrm{W}}(\lambda) + 0.06 a_{\mathrm{c}}^{*}(\lambda)[\mathrm{Chl}]^{0.65}. \quad (4)$$

In Eq. (4), a_w is the absorption coefficient of pure water and a_c* is the statistically derived [Chl]-specific absorption coefficient normalized to the chlorophyll absorption at 440 nm. The results in Fig. 1 show good agreement between the shapes of the irradiance ratio spectra predicted by the bio-optical model and provided by the RT computations. The values provided by the RT computations were higher because of the higher concentration of the mineral particles used in the calculations as explained in section 4.3.

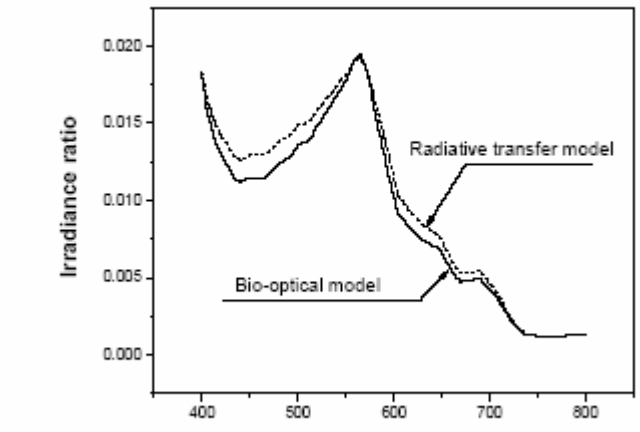

Figure 1 Irradiance ratio spectra calculated by bio-optical model and the vector radiative transfer code for case 1 waters with [Chl] = 20 mg/m^3

It is important to realize that the degree of underwater light linear polarization P_w reaches its maximum at a single-scattering angle Θ_w of about 90° for an average case I ocean. In our case, Θ_w = 150° which leads to $P_w \approx 10\%$ [21]. Since the fluorescence retrieval technique essentially uses P_w to identify contributions from elastic scattering, changes in the magnitude of P_w will significantly affect the accuracy of this retrieval. We first examined variations of this accuracy for light

emerging from waters dominated by algae. Fig. 2 shows the water-leaving reflectance and its degree of linear polarization for waters with [Chl] = 5, 20, 40 and 80 mg/m^3. It is observed that this degree varies between 8% to 16%, which, as will be seen later, is sufficient for the separation and retrieval of fluorescence.

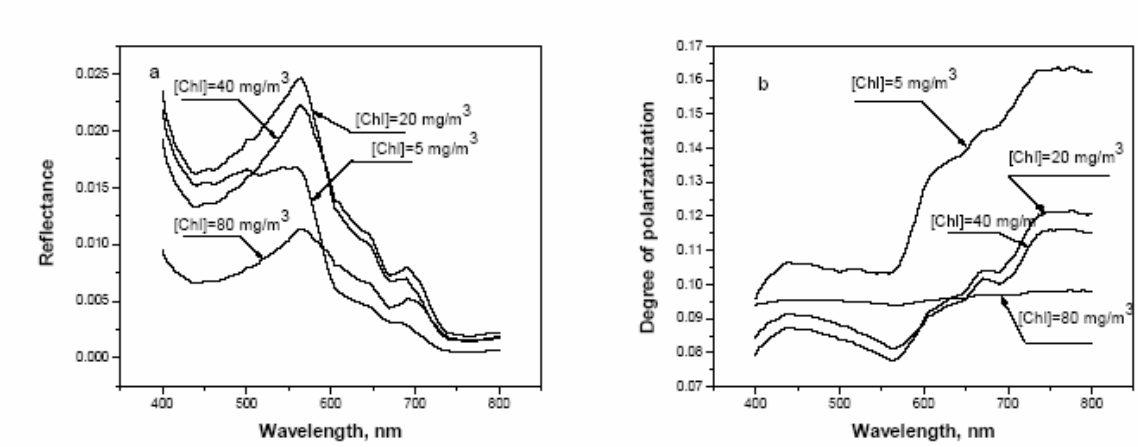

Figure 2 Spectra of water-leaving reflectance (a) degree of polarization (b) for [Chl] = 5, 20, 40 and 80 mg/m^3.

Results of $R\perp(\lambda)$ and $R\parallel(\lambda)$, as well as for the retrieval of fluorescence, are presented in Fig. 3 for [Chl] = 20 mg/m3. They show that Chlorophyll fluorescence can be extracted with high accuracy for $\lambda > 650$ nm. There are on the other hand large errors in retrieved fluorescence spectrum for the green part of the spectrum. These errors are caused by small deviations in linear relation between $R\perp(\lambda)$ and $R\parallel(\lambda)$

which are subsequently amplified by the small denominator in the equation (3.11).

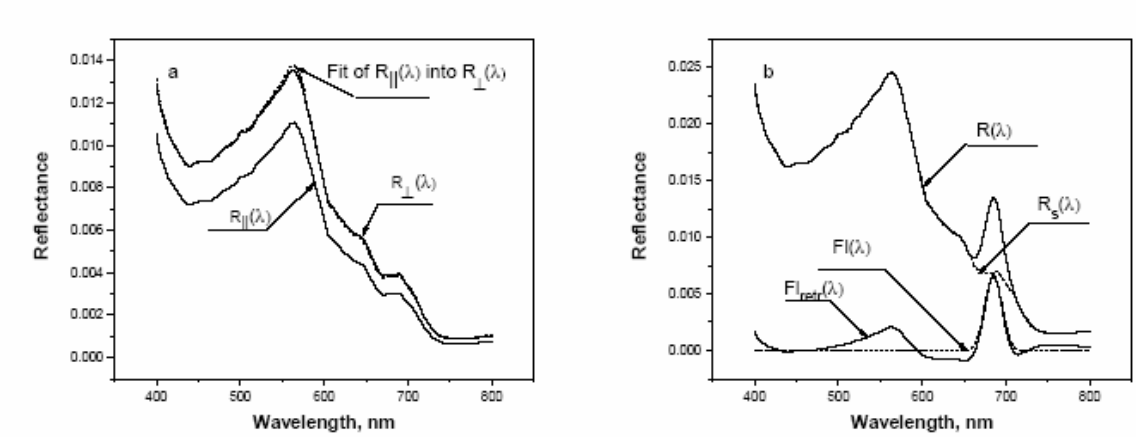

Figure 3 (a) Spectra of $R_{\perp}(\lambda)$, of $R_{\parallel}(\lambda)$, and of the fit of $R_{\parallel}(\lambda)$ onto $R_{\perp}(\lambda)$.
(b) Results of fluorescence retrieval (b) for [Chl] = 20 mg/m^3.

To see how accurate the polarization-based retrieval of fluorescence can be, the fluorescence height Fl_{retr} [defined as $Fl(685)$–$Fl(650]$ was derived from this retrieval and compared with the theoretical input and with the baseline-method derived fluorescence Fl_{baseline}. The results of this comparison are shown in Fig. 4. It is seen that while fluorescence line heights from polarization discrimination and baseline methods correlate well with the theoretical (input) values, the baseline approach systematically overestimates the fluorescence height by at least 5-10%. This error leads to an underestimation of the elastic backscatter spectrum and hence of the [Chl] value from NIR spectra. It should be pointed out that while extracting the fluorescence line height is important, the fluorescence height itself is not a complete indicator of [Chl] because of the dependence of fluorescence efficiency on illumination and environmental factors which can vary considerably.

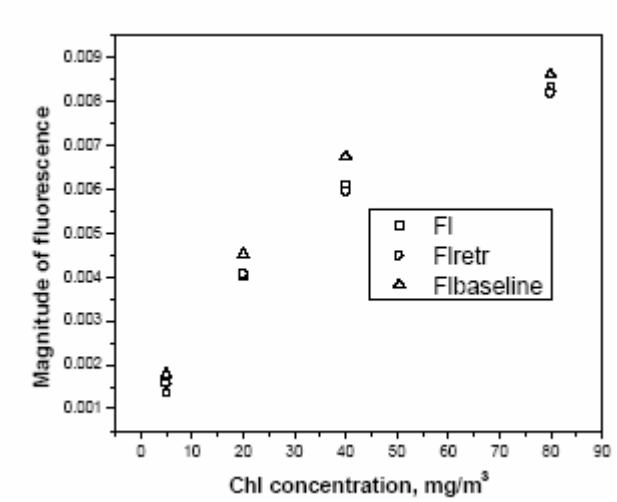

Figure 4 Comparison between the input fluorescence value and the corresponding polarization-retrieved and baseline-retrieved values

We examined also the effect of ocean surface roughness on the polarization-based retrieval of fluorescence. Fig.5 shows that while the total reflectance spectra increase if the surface wind speed increases from 1.4 m/s to 18.9 m/s, the corresponding degrees of polarization stay within the same range 8–16% in the NIR. Note however that these results pertain to average ocean surface wave slopes. To get similar results in field measurements, one should average measurements of the reflectance spectra taken over a time period of several seconds to minimize noise and fluctuations as were done in both laboratory and field tests.

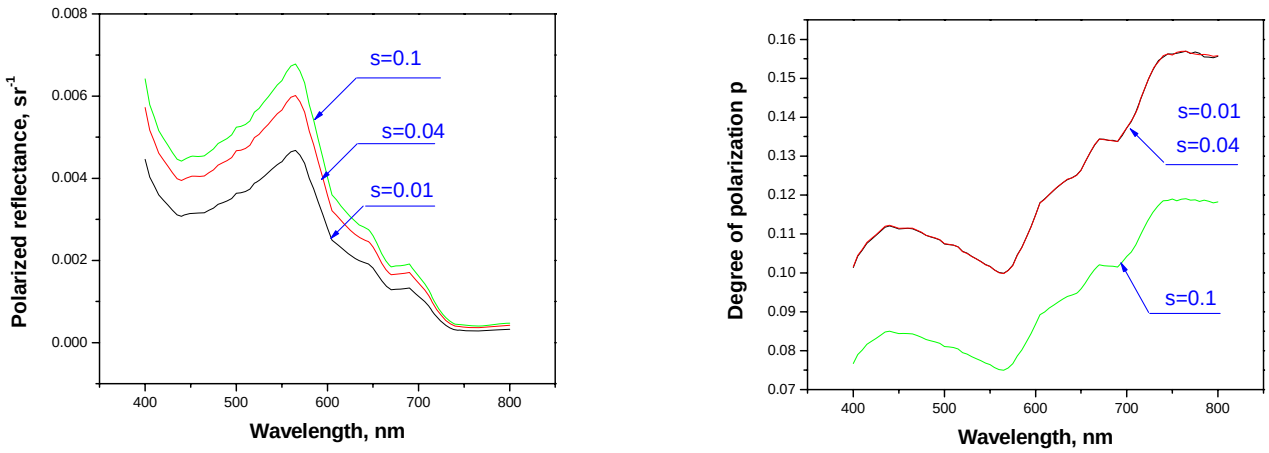

Figure 5 Polarized total reflectance spectra (a) and degree of polarization (b) for [Chl] = 20 mg/m^3 and ocean surface wind speeds ranging from 1.37 m/s to 18.9 m/s (surface roughness parameter S = 0.01-0.1.

Finally, we examined the effect of ocean bottom albedo on the polarization-based retrieval of fluorescence. We assumed this bottom to be unpolarized and modeled it as a Lambertian reflector. Here, we found the potential of significant influence on the accuracy of the polarization-derived fluorescence spectrum. In particular, when the ocean optical depth is much less than 4.6, a significant portion of the downwelling underwater light field reaches the bottom. In addition if the albedo of this bottom is larger than 0.1, light reflected by this bottom could contribute significantly to the water leaving radiances. This contribution causes the degree of linear polarization of these radiances to drop a lot. We found this occur at depths ranging from 1 to 20 m with [Chl] = 20 mg/m^3. Fig. 6 shows the accompanying large increase in total reflectance.

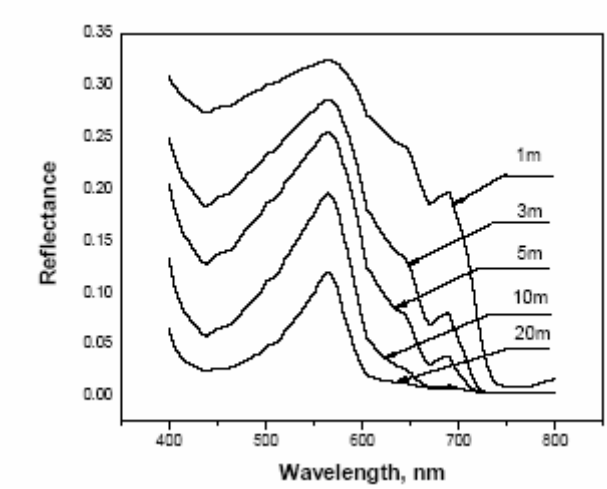

Figure 6 Reflectance for an ocean layer with [Chl]=20 mg/m^3 as a function of depths. The ocean bottom albedo and surface wind speed for these cases are 0.5 and 7.2 m/s, respectively.

While it is clear that the bottom reflection of underwater light degrades the degree of linear polarization of water-leaving radiances, one should remember that we conducted our sensitivity study for a fairly difficult scattering geometry, i.e., for a small sun angle and nadir viewing which leads to an underwater light single-scattering angle of 150°. The polarization of underwater light scattered at such angles is already quite small and hence easily masked by the unpolarized nature of light reflected by the bottom. More favorable scattering geometries can be obtained by viewing the scattering plane off the nadir direction. Such geometries lead to larger polarization degrees of water leaving radiances (provided that the polarization caused by ocean surface transmission remains small), and hence to more accurate fluorescence spectra with polarization-based retrieval methods.

4.6 Modification of the simulation model for case II waters

In case II waters, concentrations of mineral particles can dominate the scattering process and CDOM concentrations can increase the total absorption

coefficient significantly. Note that these concentrations often do not covary with [Chl]. The total absorption coefficient for such waters can be modeled by [15,20]

$$a(\lambda) = a_{\mathrm{w}}(\lambda) + a_{\mathrm{ph}}(\lambda) + N_{\min}\sigma_{\mathrm{a,min}}(\lambda) + a_{\mathrm{y}}(\lambda), \qquad (5)$$

where $a_{ph}(\lambda)$ is the absorption of algae, N_{min} is the particle concentrations, $\sigma_{a,min}(\lambda)$ is the absorption cross section of mineral particles, $a_w(\lambda)$ is the absorption of pure water, and $a_y(\lambda)$ is the absorption of yellow matter (CDOM). Algae absorption can be calculated according to $0.06a_c^*(\lambda)[\mathrm{Chl}]^{0.65}$ in Eq. (4). Absorption of yellow matter can be obtained from $a_y(\lambda) = a_y(\lambda_0)\exp[-0.014(\lambda-\lambda_0)]$ where $a_y(\lambda_0)$ is the absorption of the yellow matter at a reference wavelength λ_0. In our calculations, we choose $a_y(\lambda_0) = 0.5\ \mathrm{m}^{-1}$ at $\lambda_0 = 440$ nm.

We considered the same set of particles as in previous simulations but varied the particulate fractions with [Chl] = 20 mg/m^3 and concentrations of mineral particles [Cs] =10, 40 and 100 mg/l, which correspond to the number of mineral particles/m^3 3.36E+15, 1.34E+16, 3.36E+16 respectively. The real part of refractive index of the mineral particles is 1.18, its density is 2600 kg/m^3 and its absorption coefficient follows $a_s(\lambda) = a_s(\lambda_0)\exp[-0.009(\lambda-\lambda_0)]$, where $a_s(\lambda_0) = 0.01263[\mathrm{Cs}]$ at $\lambda_0 = 440$ nm[7].

Simulations for the conditions described in previous section show that, as a result of scattering by the mineral particles, the degree of linear polarization for water leaving radiances can become nearly zero. To increase the degree of polarization, we reduced the underwater light single-scattering angle from 150° to 128° by changing the viewing angle above the water from 0° to 30°. Results for the simulated

reflectance with and without superimposed fluorescence as well as for degree of polarization are shown in Fig. 7. Note that the degree of polarization is now of the order of 10% which allows fluorescence to be retrieved successfully. This shows that attention should be paid for the probe orientation to extract the fluorescence in case 2 waters.

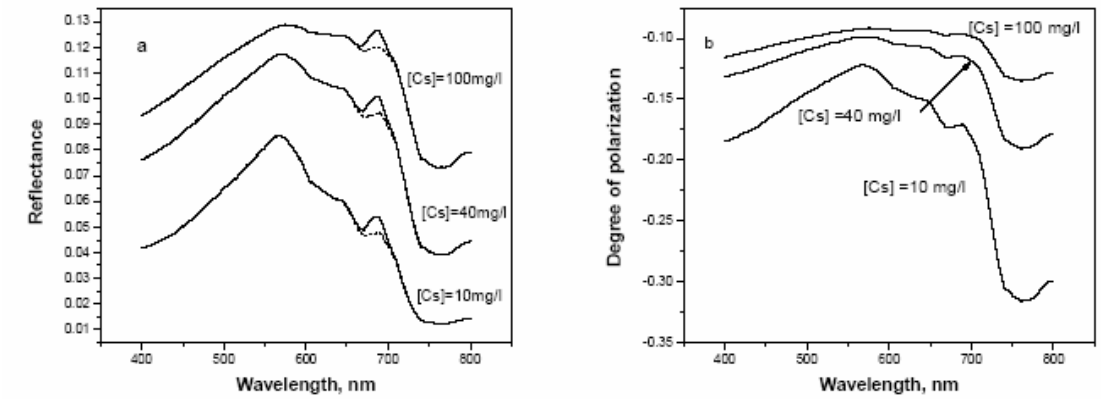

Figure 7 (a) Reflectance of water leaving radiances with (solid lines) and without (dotted lines) superimposed fluorescence. (b) The corresponding degree of polarization for [Chl] = 20 mg/m^3 and concentration of minerals [C_s] = 10, 40 and 100 mg/l.

Finally, it should be pointed out that while [Chl] was kept the same for all 3 concentrations of minerals, the fluorescence signal due to chlorophyll which reaches the detector can actually decrease for high mineral concentrations because of an slightly increase in total absorption. Our simulations demonstrate further that the fluorescence height over baseline method leads to a strong overestimation of fluorescence for such high mineral concentrations (Fig. 8).

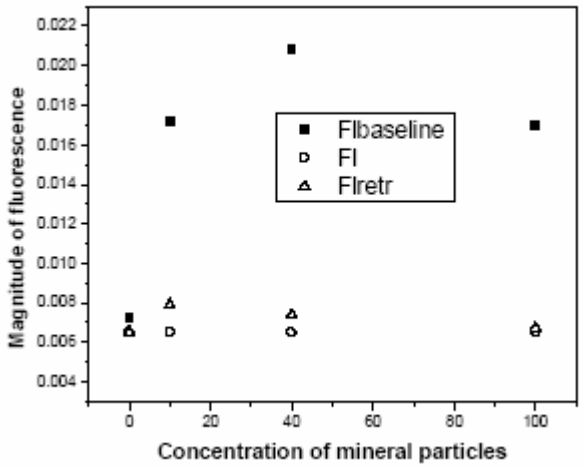

Figure 8 Comparison between the input fluorescence signal and the corresponding polarization-retrieved and baseline-retrieved values for case 2 waters.

4.7 Conclusion

The polarized radiative transfer model were employed to obtain the polarization of radiances emerging from case I and case II waters under different underwater light conditions. The calculated polarization components are used to simulate fluorescence retrieval using a recently developed polarization differentiation technique. It was found that the retrieval algorithm gives excellent results for both case I and II waters, permitting accurate extraction of fluorescence with less than 10% errors, depending on the Chlorophyll concentration and other water composition. Limitations of the method are encountered when bottom reflectance and multiple scattering due to high mineral concentration are major contributions to the water leaving radiance. To improve retrieval accuracy under such circumstances requires a change in viewing angle such that the underwater light single-scattering angles becomes closer to 90° where polarization of scattered light is the largest.

The fluorescence heights obtained by the polarization-based retrieval method were also compared to those obtained by the traditional baseline subtraction methods and found to be much more accurate. The radiative transfer analyses discussed above showed that the traditional height over baseline fluorescence extraction method strongly overestimates the fluorescence values, particularly for case II waters, where the baseline retrieved fluorescence height erroneously increases with concentration of mineral particles due to scattering/absorption changes which bias the baseline. This effect is more significant for lower fluorescence efficiencies and must be taken into account in algorithms utilizing fluorescence height.

Reference:

1. A. Morel and L. Prieur, “Analysis of variations in ocean color”, Limnol. Oceanogr. 22, 709-722, 1977

2. J. E. O’Reilly, S. Maritorena, B. G. Mitchell, D. A. Siegel, K. L. Carder, S. A. Garver, M. Kahru and C. McClain, “Ocean color chlorophyll algorithms for SeaWiFS”, J. Geophys. Res. 103 (C11), 1998, 24937-24953

3. M. Sydor, R. Arnone, “Effect of suspended particulate and dissolved organic matter on remote sensing of coastal and riverine waters”, Appl. Opt., 36, 6905-6912 (1997)

4. L. Han, D. C. Rundquist, L. L. Liu, R. N. Fraser, J. F. Schalles, “The spectral responses of algal chlorophyll in water with varying levels of suspended sediment”, Int. J. Rem. Sens., 15, 3707-3718 (1994)

5. J. F. Schalles, C. M. Hladik, “Remote chlorophyll estimation in coastal waters with tription and CDOM interferences”, Proceedings of the Ocean Optics XVII conference, (Fremantle, Australia, 2004).

6. G. Dall’ Olmo and A. A. Gitelson, “Effect of bio-optical parameter variability on the remote estimation of chlorophyll a concentration in turbid productive waters: experimental results”, App. Opt., 44, 412-422 (2005)

7. D. Doxaran, J. M. Froidefond, S. Lavender, P. Castaing, “Spectral signature of highly turbid waters: Application with SPOT data to quantify suspended particulate matter concentrations”, Rem. Sens. Of Environm., 81, 149-161 (2002)

8. C. Hu, K. J. Voss, “Measurements of solar-stimulated fluorescence in natural waters”, Limnol. Oceanogr., 43, No. 6, 1198-1206 (1998)

9. J. Fischer and U. Kronfeld, “Sun-stimulated chlorophyll fluorescence. 1. Influence of oceanic properties”, Int. J. Rem. Sens., 11, 2125-2147 (1990)

10. S. R. Laney, R. M. Letelier, and M. R. Abbott, “Parameterizing the natural fluorescence kinetics of Thalassiosira weissflogii”, Limnol. Oceanogr., 50, 1499-1510 (2005)

11. D. Pozdnyakov, A. Lyaskovsky, H. Grassl and L. Petterson, “Numerical modeling of transpectral process in natural waters: implications for remote sensing”, Int. J. Rem. Sens., 23, NO.8, 1581-1607 (2002)

12. J.F.R. Gower, R. Doerffer, G.A. Borstad, “Interpretation of the 685 nm peak in water-leaving radiance spectra in terms of fluorescence, absorption and scattering, and its observation by MERIS,” Int. J. Rem. Sens. 20, 1771-1786 (1999)

13. J. Chowdhary, “Multiple Scattering of Polarized Light in Atmosphere-Ocean Systems: Application toSensitivity Analyses of Aerosol Polarimetry,” Ph.D. thesis, Columbia University. New York, N.Y (1999)

14. J. Chowdhary, B. Cairns, M.I. Mishchenko, P.V. Hobbs, G.F. Cota, J. Redemann, K. Rutledge, Holben B.N., and E. Russell, “Retrieval of aerosol scattering and absorption properties from photopolarimetric observations over the ocean during the CLAMS experiment,” J. Atmos. Sci. 62, 1093-1117 (2005)

15. D. Stramski., A. Bricaud, A. Morel, “Modeling the inherent optical properties of the ocean based on the detailed composition of the planktonic community”, Appl. Opt., 40, 2929-2945 (2001)

16. A. Morel, “Optical modeling of the upper ocean in relation to its biogenuous matter content (Case 1 waters),” J. Geophys. Res. 93, No C9, 10749-10768 (1988)

17. C. Cox, W. Munk, “Statistics of the sea-surface derived from sun-glitter,” J. Mar. Res., 13, 198-227 (1954)

18. M.Babin, A.Morel and B. Gentili, “Remote sensing of sea surface Sun-induced chlorophyll fluorescence: consequences of natural variations in the optical characteristics of phytoplankton and the quantum yield of chlorophyll a fluorescence,” Int. J. Rem. Sens., 17, 2417-2448 (1996)

19. S.A. Green, N.V. Blough, “Optical absorption and fluorescence properties of chromophoric dissolved organic matter in natural waters,” Limnol. Oceanogr, 39, No 8, 1903-1916 (1994).

20. A. Morel, “Light and marine photosynthesis: a spectral model with geochemical and climatological implications,” Prog. Oceanogr. 26, 263-306 (1991)

21. M. Chamin, R. Santer, E. Dilligeard, “Radiative transfer model for the computation of radiance and polarization in an ocean-atmosphere system: polarization properties of suspended matter for remote sensing”, Appl. Opt., 40, 2938-2416 (2001)

Chapter 5 Particle Size Retrieval from Spectral Backscatter by Twomey Iterative Method: Simulation

5.1 Formulation of problems

For a system of spherical particles in the single and independent scattering regime, the backscattering coefficient b(λ) can be related to the particle size distribution (PSD) f(r) by the following Fredholm integral equation of the first kind [1]:

$$b(\lambda) = N_0 \int_{r_{\min}}^{r_{\max}} Q_b(\lambda, r, n) \cdot \pi r^2 \cdot f(r) dr \qquad (1)$$

where Q_b is the Mie backscatter efficiency which is determined by wavelength λ, size radius r and refractive index of particles relative to surrounding media n. N_0 is the total number density of the particles. f(r) is normalized such that: $\int_{r_{\min}}^{r_{\max}} f(r) dr = 1$. r_{min} and r_{max} is the lower and upper limit of particle sizes. If we divide the finite size range $[r_{min}, r_{max}]$ into N intervals with equal spacing $\Delta r = (r_{max}-r_{min})/N$ and approximate f(r) on the jth interval $[r_j, r_{j+1}]$ by $f(r_j+\Delta r/2)$, eq. (1) is reduced to a set of linear equations:

$$b(\lambda_i) = b_i = N_0 \sum_{j=1}^{N} K_{bij} \cdot f_j \qquad i = 1, 2, \cdots M \qquad (2)$$

where

$$K_{bij} = \int_{r_j}^{r_{j+1}} Q_b(\lambda_i, r) \cdot \pi r^2 dr \qquad (3) \qquad j = 1,2, \cdots N$$

and f_j is the number density of particles within size range $[r_j, r_{j+1}]$ and $r_j = r_{\min} + (j-1) \cdot \Delta r$

Unfortunately, using the number density may result in unstable retrievals since even for relatively high number densities at smaller radii particles, the scattering is dominated by large particulates. To help reduce this problem, a weighting function w(r) can be used to modify the inversion process. In particular, it has been shown[1] that retrieving the particle volume density: $v(r) = w(r) \cdot f(r)$ where $w(r) = \frac{4}{3}\pi r^3$ is more stable. In the volume representation,

$$b_i = N_0 \sum_{j=1}^{N} \overline{K}_{bij} \cdot v_j \quad (4)$$

where $\overline{K}_{bij} = \int_{r_j}^{r_{j+1}} \frac{Q_b(\lambda_i, r) \cdot \pi r^2}{w(r)} dr$.

In all of the following work, we first solve for $v(r)$ and then transform back to particle size distribution via $f_j = \frac{v_j}{w(r_j + \frac{\Delta r}{2})}$.

5.2 Review of inverse method

The particle size retrievals from light scattering usually involve the solution of the ill-posed Fredholm equation of the first kind like eq. (1) and in most of cases its discrete linear format eq. (2). This is notoriously difficult in that each row of the kernel matrix $\mathbf{K}$ is not completely independent to each other and more than one solution can satisfy this equation within the measurement error limits. Various numerical schemes have been developed to find the optimal solutions[2,3].

Generally, Eq. (2) can be written in matrix-vector notation as $\mathbf{b} = \mathbf{Kf}$, where $\mathbf{b}$ is a column vector with M elements, $\mathbf{f}$ is a column vector containing N number of

sought for function values and $\mathbf{K}$ is a M×N matrix. The minimization of the residual $(\mathbf{Kf}-\mathbf{b})^{\mathbf{T}}(\mathbf{Kf}-\mathbf{b})$ leads to the solution: $\mathbf{f}=(\mathbf{K}^{\mathbf{T}}\mathbf{K})^{-1}\mathbf{K}^{\mathbf{T}}\mathbf{b}$. Since $\mathbf{K}$ is usually nearly singular, the measurement errors in $\mathbf{b}$ will be magnified enormously by the very small eigenvalues of $\mathbf{K}$, which makes a highly unstable solution. Small changes in the measurement data can result in a large variation in the solution that is often unphysical though mathematically acceptable. In order to find the sought for solutions, additional restrictions such as smoothness have to be imposed on $\mathbf{f}$, which yields the Twomey-Philips solution: $\mathbf{f}=(\mathbf{K}^{\mathbf{T}}\mathbf{K}+\gamma\mathbf{H})^{-1}\mathbf{K}^{\mathbf{T}}\mathbf{b}$, where the $\mathbf{H}$ matrix is nearly diagonal and depends on the choice of smoothing constraint and γ is an underdetermined Lagrangian multiplier to measure the strength of the constraint $\mathbf{H}$. This constrained linear inversion has been widely used to retrieve atmospheric aerosols from lidar data[4-7]. To develop an optimal solution, the value of γ need to be carefully determined to balance between the smoothness of the retrieved solution and the degree in which the physical model reproduces the measurement data. This scheme is referred to as regularization and the balance between smoothness and goodness of fit is quite complex and hardly unique.

To reduce the instability of noise, it is often sufficient to restrict the retrieved distribution to a parameterized analytic function such as Gaussian or log-normal distribution and apply nonlinear least square fitting to optimize the distribution parameters [8-10]. However, in most cases of interest, such shape constraint methods impose too many assumptions on the nature of the size distribution. It becomes even more problematic when multimode distributions are considered. Alternatively, since the backscatter spectrum exhibits oscillations which depend on particle size, Fourier

transformation of the spectra can be also used to retrieve size information, but it is mainly applicable to nearly mono-dispersed particle analysis. [11,12]

Stochastic optimization like inverse Monte Carlo (IMC)[13,14] and genetic algorithm technique [15] have been applied to determine particle size distribution (PSD) from both angular scattering and wavelength dependent extinction and backscatter. These methods in general have the advantage of insuring positivity while smoothness is maintained by an appropriate termination conditions. However, these approaches are very computer intensive. To avoid the time complexity, iterative inversion method such as modified Chahine algorithm can be used to obtain PSD from spectral extinction data [16]. However, the latter requires that the kernel response function possesses a smooth kernel with a single maximum value which is not appropriate for highly oscillatory backscatter kernels. To eliminate the restrictions of Chahine method, another iterative approach proposed by Twomey, which does not require a highly peaked kernel function is considered here. This approach has been applied to analysis of data from indirect measurement techniques including multi-wavelength extinction coefficient measurements [17] and cascade impactor measurements in aerosol science [2,18], but the application of this approach to retrieve hydrosols microphysics from the backscattering spectrum of white light has not been explored so far.

In this chapter, TIM has been applied to the retrieval of PSD from backscatter spectrum over wavelength range $0.4\mu m \leq \lambda \leq 0.8\mu m$. The TIM method is described in section 2. In section 3, we report on extensive tests of the TIM on computer simulated backscatter spectra generated from both single mode and multi-mode distributions.

Within this context, TIM's ability to handle noise is examined. In section 5, an iterative procedure is introduced to obtain the average particle refractive index for mono-dispersed system and is also verified through simulation.

5.3 Twomey iterative method (TIM)

The TIM begins with an initialization of the distribution v_j^0. In the kth iteration, $\hat{b}_i^k$ is the calculated result from v_j^k:

$$\hat{b}_i^k = \sum_{j=1}^{N} \overline{K}_{ij} \cdot v_j^k \qquad i = 1, 2, \cdots M \qquad (5)$$

then by comparing $\hat{b}_i^k$ with the actual measurement data b_i and introducing high frequency components which are spectrally similar to the kernels into the solution, v_j^{k+1} for the next iteration is obtained according to the following correction[12]:

$$v_j^{k+1} = \{\prod_{i=1}^{M} [1 + (\frac{b_i}{\hat{b}_i^k} - 1) \cdot \overline{K}_{ij}]\} \cdot v_j^k \qquad (6)$$

Note that $\frac{b_i}{\hat{b}_i^k} - 1 \geq -1$ and $\overline{K}_{ij}$ is always less than 1, the adjustment factor is always greater than zero so that v_j^k will never turn negative with a positive initial v_j^0. Also to eliminate calibration issues, only the shape of the backscatter spectrum is considered here so that N_0 can be absorbed by normalizing b_i and $\hat{b}_i$.

The following two metrics were used to test for convergence:

$$\chi_1 = \frac{1}{N} \sqrt{\sum_{i=1}^{N} (\frac{b_i - \hat{b}_i^k}{\hat{b}_i^k})^2} \qquad \chi_2 = \sqrt{\sum_{j=1}^{M} (v_j^{k+1} - v_j^k)^2} \qquad (7)$$

where χ_1 is root mean error (rme) which describes the average relative deviation of the fitted data from the measured data and χ_2 measures the average difference in v_j between consecutive iterations. The iteration stops when either χ_1 is less than a specified value chosen to be around the input noise level or χ_2 reaches a very small value (10^{-4} was used here). Fig. 1 describes the flow of steps of the inversion process.

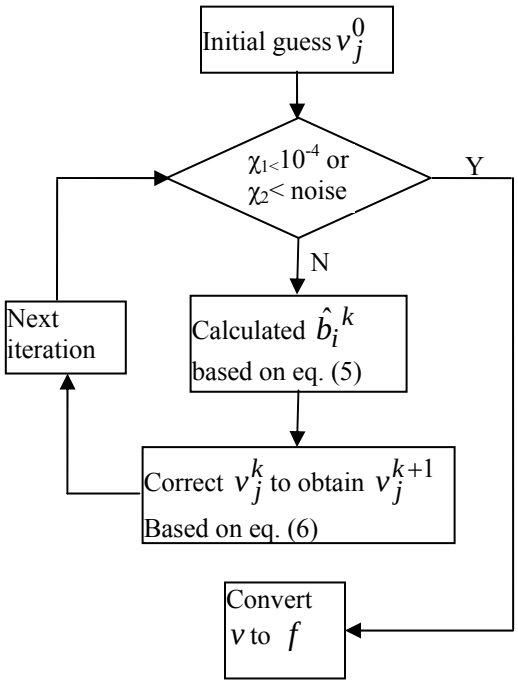

Figure1. The flowchart of TIM iteration method

5.4 Simulated retrieval

5.4.1 Implementation

The computer generated spectra were calculated based on eq. 1) by assuming a two parameter log-normal PSD functions:

$$f(r;r_m,\sigma)=\frac{1}{r\cdot\sigma\cdot\sqrt{2\pi}}\cdot\exp[-\frac{(\ln r-\ln r_m)^2}{2\sigma^2}] \qquad (8)$$

where r_m is the mode radius and the σ is the logarithm of the width of the distribution. When σ is small, the corresponding standard deviation of the size distribution (δ) defined as:

$$\delta = \sqrt{\int_0^\infty (r-\bar{r})^2 f(r) dr} \qquad (9)$$

is approximately $\sigma \cdot r_m$, where $\bar{r}$ is the average size radius $\bar{r} = \int_0^\infty r f(r) dr$.

Unless otherwise stated, as in section 5, the refractive index of the particles is fixed at n_p=1.589 for all the wavelength values within the spectral window. Considering that the average refractive index of water is 1.33, the relative particle refractive index is n=1.1917. In order to investigate the sensitivity and stability of TIM retrieval for various signal to noise ratios S/N, different levels of random noise were superposed on the generated data b(λ) to simulate the real measurement:

$$\tilde{b}(\lambda) = b(\lambda) \cdot (1 + \gamma \cdot \varepsilon) \qquad (10)$$

where γ is the relative noise level to the signal (=1/SNR) and ε is a normally distributed random numbers with zero mean and unit standard deviation. The inversion is repeated with 50 different noise ensembles to determine the statistics in the retrieval process.

In this work, the size (radius) range was set to [0.1μm, 2μm]. This is reasonable given that backscattering spectrum from particle sizes of the same order as the measurement wavelength possess size dependent scattering efficiency. The wavelength range from 0.4μm to 0.8μm is sampled at 5nm resulting in a total of N=81 points over the wavelength range. This sampling frequency is sufficient to

sample the oscillatory features of the backscatter spectrum for all mono-dispersed particles in the given size range. To determine the number of size bins over the size range considered, it is important to note that, on one hand, a large number of size bins introduces instability into the inversion while on the other hand, the ability to resolve a narrow distribution is determined by the interval between the grid points. We have found that the most robust choice in our simulations were to make the number of radius bins equal to the number of wavelength bins so M = N = 81.

5.4.2 Initialization and numerical properties

If the initial guess is chosen so that $\frac{b_i}{\hat{b}_i^0}$ is close to 1, there will be little correction and the iteration will stop immediately since the correction factor approaches unity. It is often common to assume a uniform distribution for the initialization. However through numerical simulations, we observed that this choice of initial distribution tends to produce final results that overestimate the value at small size bins because of their small scattering cross section. In other words, the initial distribution should not be homogeneous over the size window since small radii contribute little to the resultant backscatter spectrum. Instead we use a power distribution r^p where p is an exponent usually chosen to be p=6 for the retrieval. However, in the presence of high noise on the order of 30%, it may be necessary to use an even higher exponent. The initialization mentioned here is for $f(r)$ instead of volume density distribution $v(r)$, therefore the initial $v(r)$ used in the simulation is r^{p+3}. Since absolute particle number density requires absolute calibration, we choose to normalize all PSDs to unit area.

In all simulations, the residual χ_1 usually drops sharply within first 100 iterations and slow down after that. It takes around 500 iterations for χ_2 to reach its stopping threshold. Less iteration are needed when noise is present in the spectrum since the iterations will terminate as the residual χ_1 approaches the noise level before it reaches the threshold of χ_2. The speed at which the each method performs depends on specific computer used. However comparison is still possible between different methods based on the machine independent benchmark. On a Pentium 4 2.4GHz machine inversion result including the uncertainties test of the noisy data can be obtained by TIM method in approximately 10s, while 120s is needed for the statistical methods such as IMC on a SGI ONYX/R10000 mainframe [13]. Considering our machine is 3 times faster than the SGI computer in terms of floating point calculation ability, our method should be approximately 4 times faster than the IMC method.

5.4.3 Single mode distribution

A set of synthetic backscatter spectra were generated from mono-modal lognormal PSDs by varying the modal radius in the range of r_m=[0.2, 1.8]μm with step size of 0.1μm for 3 different standard deviations (δ=0.01, 0.05, 0.1μm) to test the TIM retrieval. In these simulations, both uniform and power law initial distribution were used. The optical backscatter spectra were modified by adding 5% random noise when utilizing power law initial distribution. Adding 5% noise to the uniform initialization resulted in very large error fluctuations, so for comparison, uniform initial distribution was performed on the noise-free spectra. In Figures 2(a),(c) and (e), the ratio between the retrieved radius and the modal radius R=$\frac{r_{ret}}{r_m}$

are plotted as a function of r_m. The retrieved distribution widths in terms of standard deviation δ_{ret} vs. r_m are also displayed in Figures 2(b), (d) and (f) for each case of the three input δ values (panel a,b: δ=0.01μm; panel c,d: δ=0.05μm and panel e, f: δ=0.1μm). To see the retrieved size distribution more clearly, we plot in Figures 3-5, the retrieved PSD together with the corresponding input distributions (solid line) in the left panels and the fitted backscatter spectrum (dots) compared with the synthetic spectrum (solid line) in the right panels for two selected particle sizes at each δ value: Fig. 4, r_m=0.3 and 1.8μm with δ=0.01μm; Fig. 5, r_m=0.9 and 1.5μm with δ=0.05μm; and Fig 6, r_m=0.7 and 1.5μm with δ=0.1μm. In these figures, the triangle symbols represent the retrieval results for the power law initial distribution. For the purpose of illustration and less confusion the retrieved PSD using uniform initialization was shown only in Fig. 4 (star symbol).

In general, we observe that the power law initialization is far more accurate in retrieving the mean particle radius than uniform initialization. The r_{ret} obtained from uniform initial guess is smaller than the input r_m except for sufficiently narrow distributions and small radii. This can be explained by realizing that relatively large values in small radii bins contribute little to the resultant backscatter spectrum and therefore limits the sensitivity of the TIM method to make corrections in the small size bins. As seen in Fig. 4, when uniform initialization is used, the iteration can reach the termination criteria still with spurious spikes at small sizes. In order to compensate for this overestimation at small sizes, an initial distribution biased towards the large sizes is required. As shown in Fig. 4 (a) and (c), the power law initial distribution effectively removes the spurious spikes at the lower end of size

window and retrieves the mean radius r_{ret} with much higher accuracy: within 5% for δ=0.01μm and 15% for δ=0.05μm. The retrieved width δ_{ret} for these two δ values (Fig. 2 (b) and (d)) was also vastly improved when a power law initialization is used.

One notable feature is the remarkable ability of TIM to retrieve the size distributions for such a wide range of particle sizes considering that the size windows are much larger than the wavelength ranges of the backscattering spectra. This results from the inherent positive constraint of TIM technique and compensation effect of the power law initial distribution.

As the width of the PSD function becomes broader, there are less and less features in the backscattering data within the limited spectral range. A direct result of this is that there will be a broader class of solutions that are indistinguishable from the backscattering spectra in terms of a noise level threshold within the residual χ_1. This is the case for δ=0.1μm and the solution depends much on the choice of the initial guess. The accuracy of the retrieved size radius is within 40% in this case.

In Fig. 3 and 4, for small widths, we see that there is sufficient spectral structure to accurately retrieve the distributions. In Fig. 5, the TIM solution is far less accurate and only partially retrieves the PSD. However, even in this case, for sufficiently large particles, $r_m \geq 1.3\mu m$, the retrievals are much more accurate. This may be explained by observing that for a given absolute width, the fractional width becomes smaller with increasing mode size, resulting in more spectral features. In addition, the initial guess is weighted significantly to large particles.

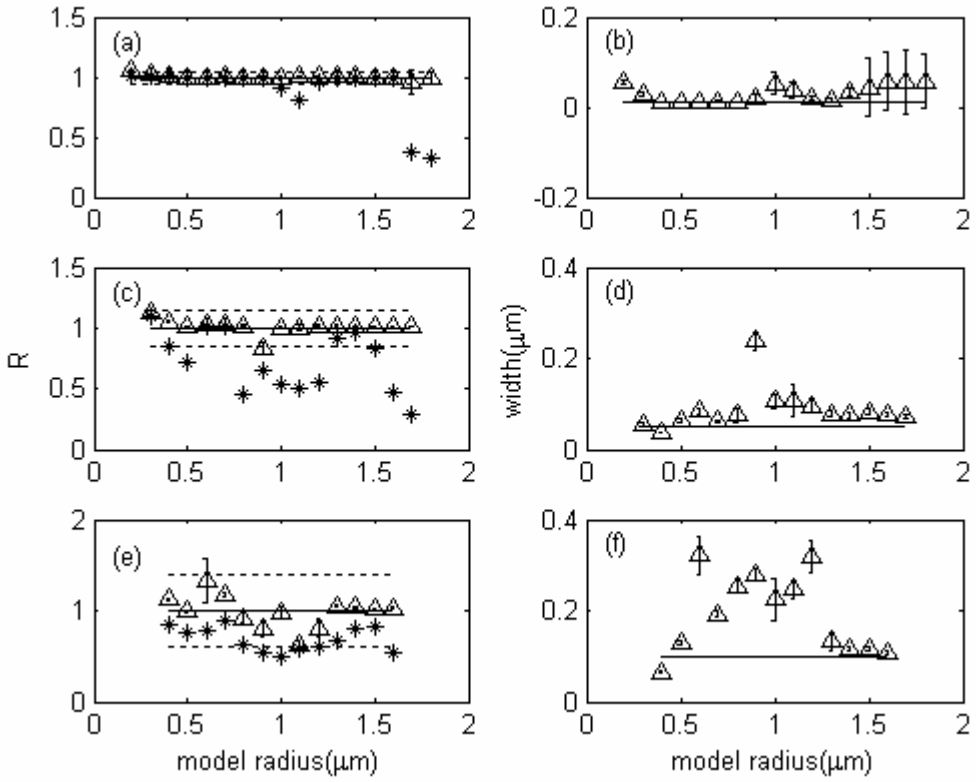

Figure 2 The ratio between the retrieved radius and the modal radius $R=\frac{r_{ret}}{r_m}$ (left) and the retrieved width δ_{ret} (right) as a function of input modal width r_m. In (a), (c), (e), solid line: R=1; dashed line: maximum error bound. In (b), (d), (f), solid line: input δ values. Triangle: power law initialization; star: uniform initialization. (a), (b) for δ=0.01μm; (c), (d) for δ=0.05μm and (e), (f) for δ=0.1μm

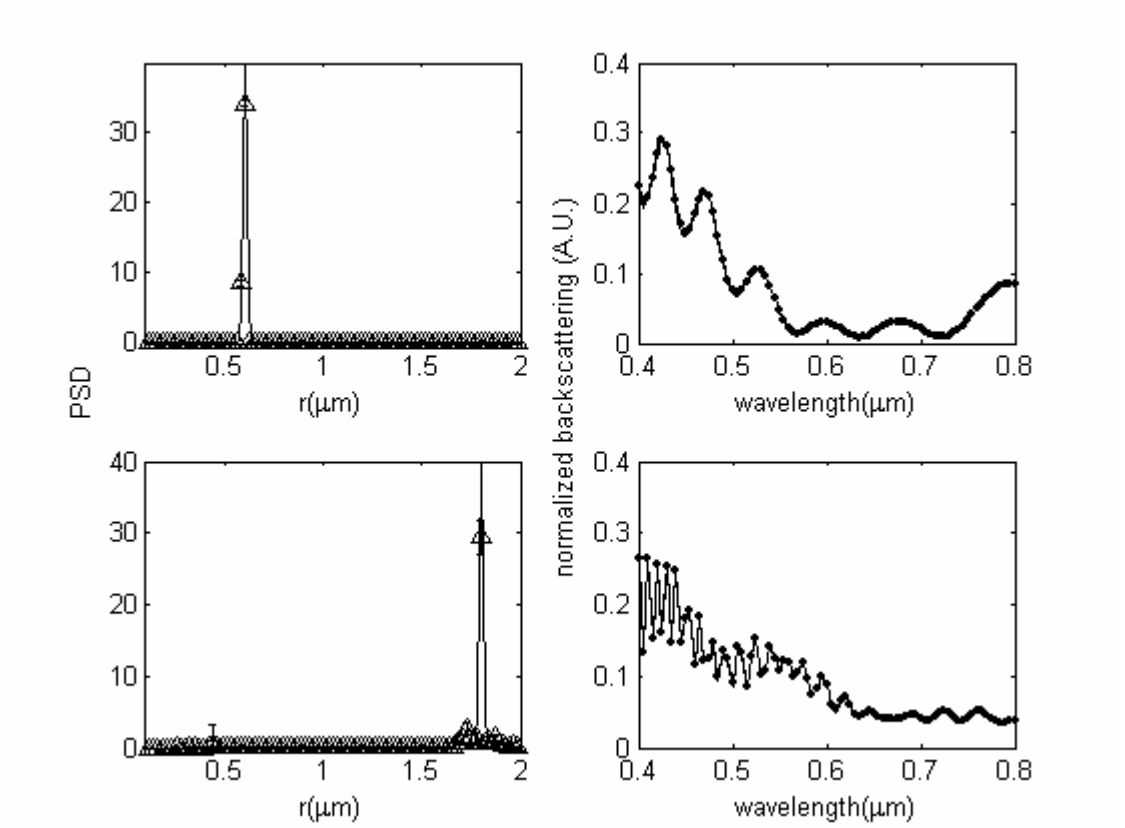

Figure 3 Retrieval results for two selected modal radius with δ=0.01μm. r_m=0.6μm in (a), (b); r_m=1.8μm in (c), (d). (a), (c): the retrieved PSD functions (triangle) and the exact distribution (solid line); (b), (d): the input backscatter signal (solid line) and the fitted one from the retrieval (dots)

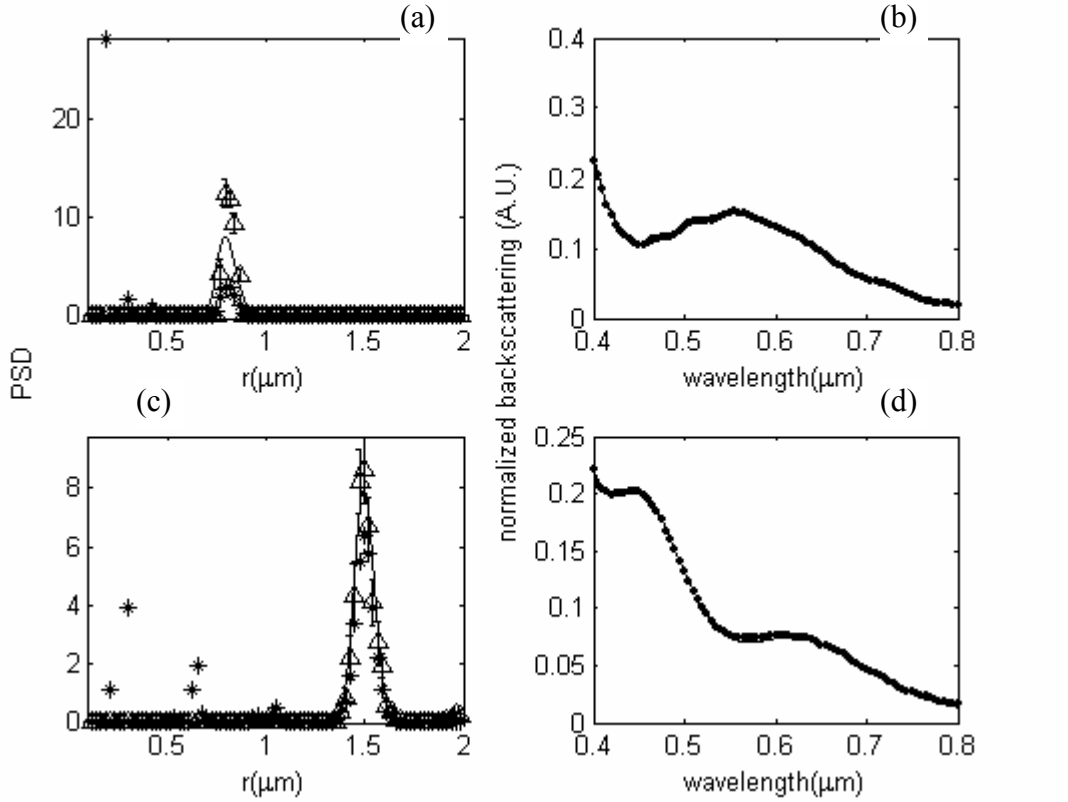

Figure 4 Retrieval results for two selected modal radii with distribution width δ=0.05 μm. r_m=0.9μm in (a), (b); r_m=1.5μm in (c), (d). In (a), (c): retrieved PSD functions using power law initialization (triangle) and uniform initialization (star) as well as exact distribution (solid line). In (b), (d): input backscatter signal (solid line); fitted backscatter spectrum (dots).

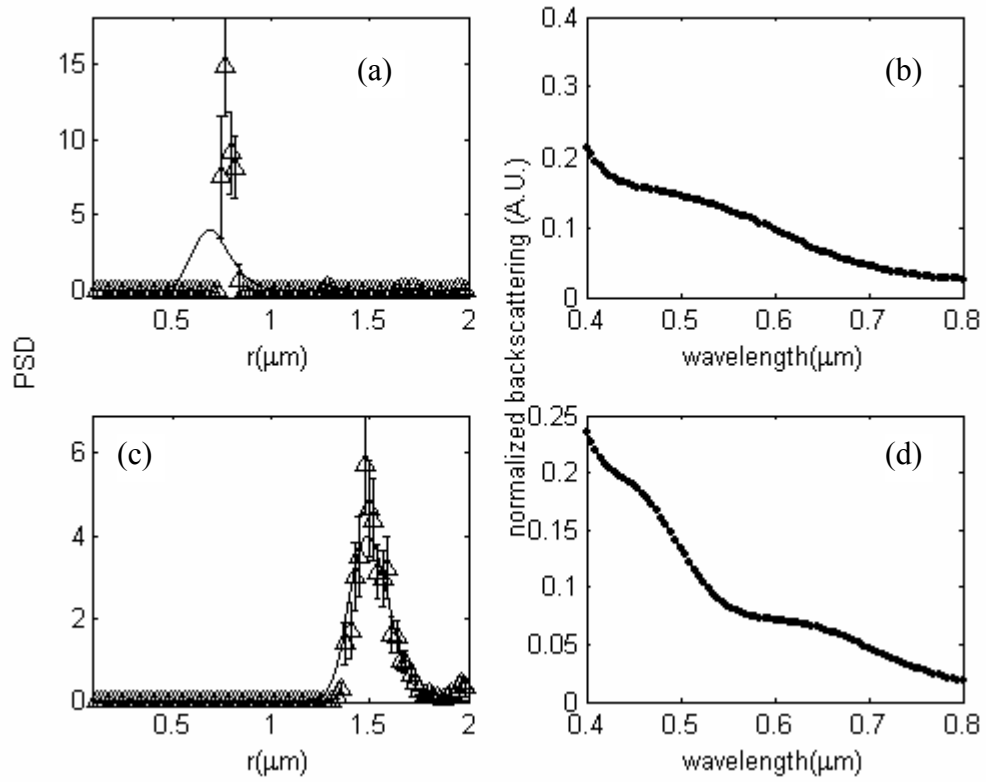

Figure 5 Retrieval results with 5% noise for two selected modal radius with δ=0.1μm. r_m=0.7μm in (a), (b); r_m=1.5μm in (c), (d). (a), (c): the retrieved PSD functions (triangle) and the exact distribution (solid line); (b), (d): the input backscatter signal (solid line) and the fitted one from the retrieval (dots).

5.5 Noise sensitivity of TIM retrieval

Various noise levels were added to the backscattering data to test the sensitivity and stability of the TIM retrieval. Fig.6 shows the retrievals of mean radius r_{ret} and standard deviation δ_{ret} for two sharp distributions (δ=0.01μm) with radii r_m=0.6 and 1.2μm for variable noise levels up to 30%. For r_m=0.6μm, errors in the retrieval are negligible over the noise range considered. However for r_m=1.2μm particles, as the noise increases, the retrieval significantly underestimates the mean particle sizes and the error in the retrieved mean radius increases substantially as spurious spikes appear in the smaller particle size bins in the final PSD solution. The comparatively large uncertainties associated with the retrieval with noise level > 5% show that these spikes are strongly dependent on the noise. Therefore the power law initial distribution can also ensure the stability of the solution by effectively reducing the possibility of spurious spikes at the lower end of size windows. The retrieved distribution widths δ_{ret} were always larger than the input ones and proportional to the noise since the iteration stops before it reaches the noise level. For the same noise level, the retrieved distribution for 0.6μm particles shows much better accuracy and stability than that of 1.2μm particles. Examining the backscattering spectra of these two particles, the oscillatory features for the 1.2μm particle are sharper and shallower than that of 0.6μm, which makes them more difficult to be resolved in the presence of the same level of noise. Fig. 7 shows the retrieved PSD functions for r_m=0.6 (left) and 1.2μm (right) with δ=0.05μm at three different noise levels (5%, 15%, 30%) added to the simulated backscattering spectra. As expected, the retrieval becomes more and more susceptible to noise at higher noise levels since there are increasing

combinations of size classes within the same size windows that can reproduce the input backscattering spectrum well within the noise limit. However, the bell shape of the input distributions can be still recovered with the noise up to 30%.

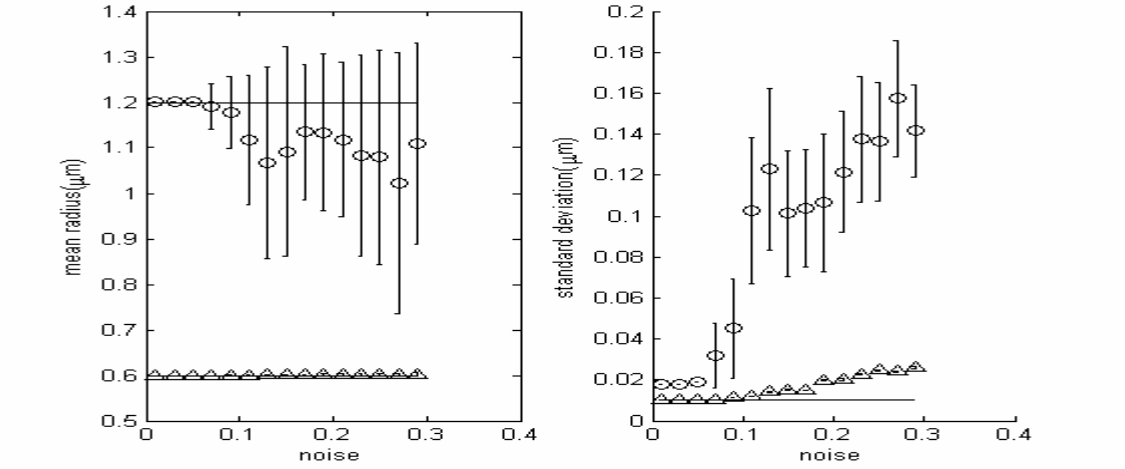

Figure 6 Retrieved mean radius r_{ret} (left) and standard deviation δ_{ret} (right) compared with the input values (solid line) as a function of noise for two sizes at δ=0.01μm: r_m=0.6 (triangle) and 1.2μm (circle).

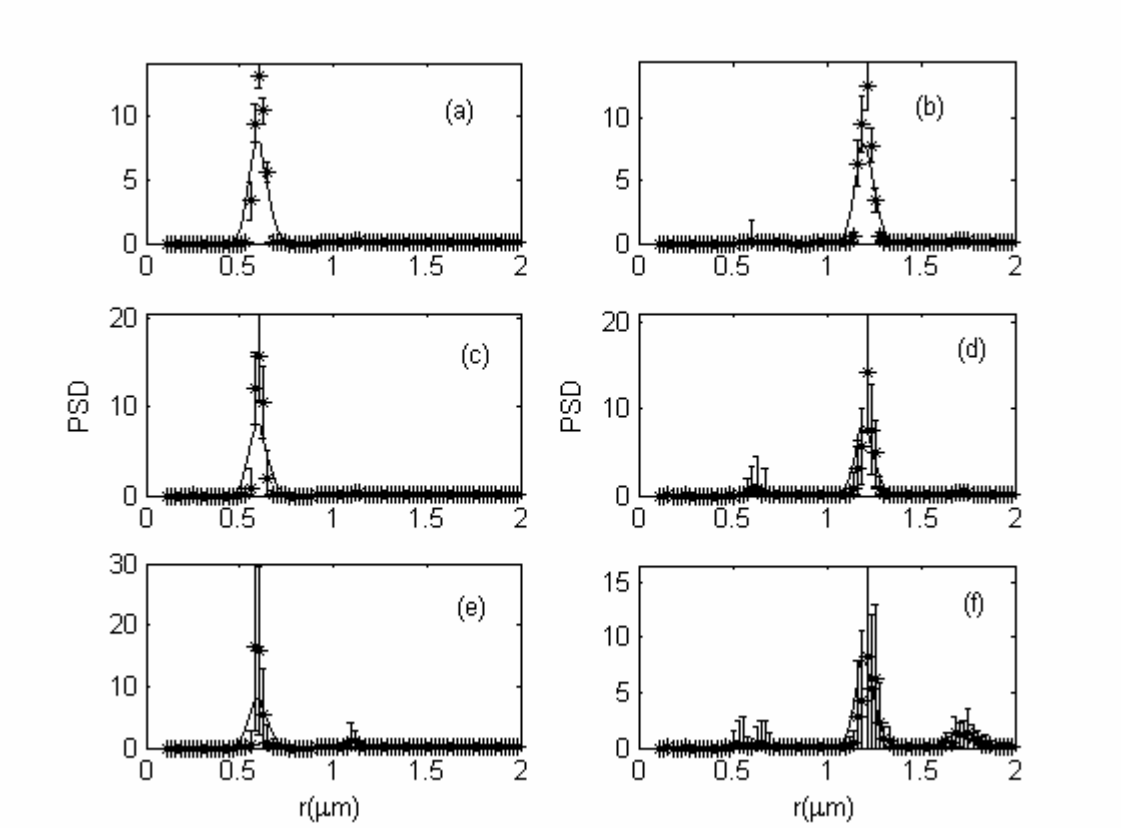

Figure 7 Retrieved PSD (star) with three different level of noise for two distributions with δ=0.05μm and r_m=0.6 (left) and 1.2μm (right). (a), (b): 5%; (c),(d): 15%; (e), (f): 30%. Solid line is the exact the distributions.

5.6 Multimode distribution

In this section, we apply the TIM to the retrieval of a mixture of 4 single-mode log-normal distributions $f_i(r;r_i,\sigma)$ with modal width σ=0.01:

$$f(r)=\sum_{i=1}^{4} c_i \cdot f_i(r;r_i,0.01) \qquad (11)$$

The relative amplitudes c_i were chosen for simplicity to be equal, and c was normalized to unity (i.e $c_i = 0.25$). Two different 4-mode distributions are used here:

1) r =0.5, 0.6, 0.7, 0.8μm
2) r =1.4, 1.5, 1.6, 1.7μm.

Fig. 8 is the retrieved PSD from synthetic backscattering spectra with 1% ((a) and (b)) and 5% ((c) and (d)) noise level respectively. It can be seen from the figure that the TIM can distinguish the correct location of all the multiple peaks for both distributions. The accuracy of the retrieved relative amplitudes of each mode is limited by the resolution of the size bins. For higher noise (5%) the four peaks are still distinguishable but large uncertainties in small size bins occur for the case 2 distribution. This is again due to the fact that the shallower and sharper oscillatory patterns in backscattering spectra for large particles are more easily to be disguised by noise.

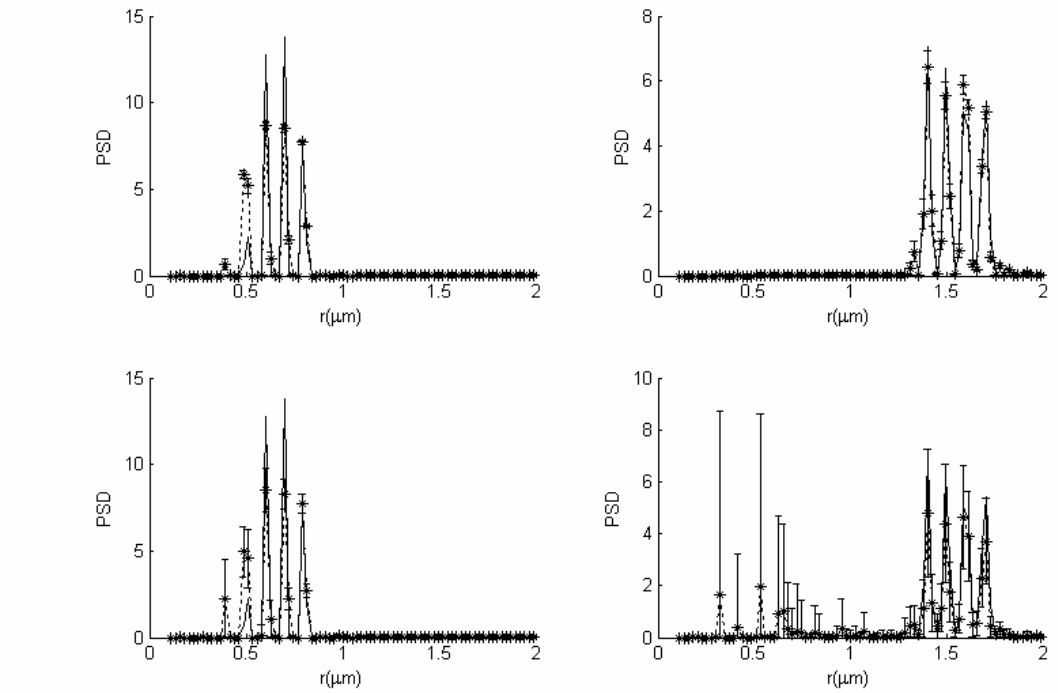

Figure 8 Retrieved PSD (star with broken line) for two 4-mode distributions: (a), (c) r =0.5, 0.6, 0.7, 0.8μm; (b), (d) r =1.4, 1.5, 1.6, 1.7μm, compared with the exact distributions (solid line)

5.7 Refractive index retrieval

Up to this point, the refractive index of the particles was assumed to be known n_p =1.589. However, in many actual experimental situations, the refractive index may not be known a-priori. Fortunately, the oscillatory features in the backscatter spectral data from particles with narrow distribution are very sensitive to the relative refractive index. Taking advantage of this property, several refractive indexes can be tried in the inversion and the refractive index with the minimum fitting residual χ_l would then be the retrieved refractive index. This approach has been already suggested [13]. But the speed and simplicity of TIM retrieval compared with inverse Monte Carlo method makes this procedure more efficient. The usefulness of this method is tested on four simulated narrow distributions with r_m = 0.25, 0.6, 1.2 and 1.8μm and with their modal widths σ adjusted so that all of them have the same standard deviation δ= 0.01μm. The backscattering spectra were generated by using three different values of relative refractive index: 1.05(representative of algal particles), 1.113 and 1.196 and 5% noise was added to the spectra. Independent TIM inversions for 15 evenly spaced values of real relative refractive index of the particles in the range of 1.02 to 1.3 were carried out. The residual χ_l as a function of refractive index is plotted in Fig. 9. Only when the refractive index used in the retrieval is close to the actual particle refractive index, does the residual reach the minimum, except for the smallest particles (0.25μm). The retrieved refractive index was1.04 for input index n=1.05, in the range of 1.1-1.12 for n =1.113 and in the range of 1.18-1.2 for n =1.196. The error is less than 10% and limited by the grid spacing of the refractive index. For the case of 0.25μm particles, χ_l approaches the noise level at multiple

refractive indices. This is due to the limited oscillations found in the backscatter spectra of small particles making the fitting residuals less sensitive to the particle refractive index used in the retrieval.

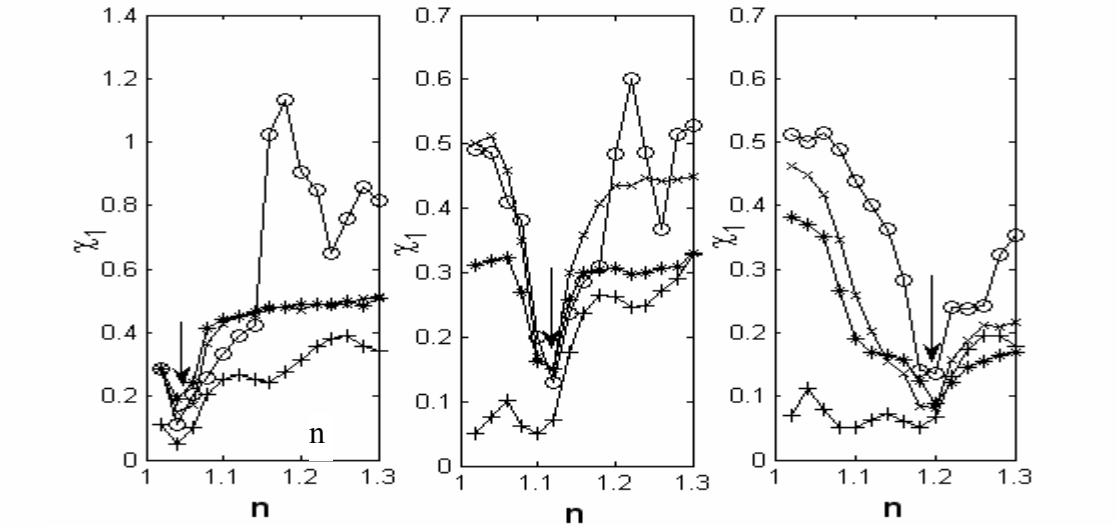

Figure 9 Refractive index retrieval of simulated backscatter spectra for four size distributions with δ=0.01μm and three different relative refractive indices. plus (+): r_m=0.25μm; circle(°): r_m=0.6μm cross (×) : r_m=1.2μm and star (*): r_m=1.8 μm. The retrieved refractive indexes are indicated by the arrows: n =1.05 (left), 1.113 (middle) and 1.196 (right) respectively

5.8 Conclusion

Twomey iterative method (TIM) has been applied to the retrieval of various particle size distributions including both single mode narrow and broad distributions as well as multi-mode distributions from simulated backscatter spectra in the range of 0.4-0.8μm. This method possesses a build-in positivity constraint and no priori information about the size distributions is needed for the retrieval. Fast retrieval computation speed and lack of any requirements for peaked kernels make this technique very suitable for the online particle size inversion from multi-wavelength and hyperspectral optical data. With an initial guess distribution which is biased towards large sizes, single mode PSDs can be recovered for size radii from 0.1μm to 2μm with standard deviation up to 0.1μm, which is much wider than the available

spectral range. Furthermore, the mixture of up to 4 single modes has also been successfully retrieved by this method. In order to find the particle refractive index, an independent inversion at several refractive index values was performed and the refractive index which has the best fit was chosen for the particle refractive index. This iterative procedure was successfully applied to simulated spectra for narrow distributions and the refractive index was obtained within an accuracy of 10%.

Reference:

1. Detlef Muller, Ulla Wandinger and Alber Ansmann, "Microphysical particle parameters from extinction and backscatter lidar data by inversion with regularization: theory", Appl. Opt. 38, 2346-2357 (1999)

2. Kusiel S. Shifrin, "Spectral attenuation and aerosol particle size distribution", Appl. Opt. 35 2114-2124 (1996)

3. L. T. Perelman, V. Backman, M. Wallace, G. Zonios, R. Manoharan, A. Nusrat, S. Shields, M. Seiler, C. Lima, T. Hamano, I. Itzkan, J. Van Dam, J. M. Crawford and M. S. Feld, " Observation of Periodic Fine Structure in Reflectance from Biological Tissue: A New Technique for Measuring Nuclear Size Distribution", Phys. Rev. Lett. 80, 627-630 (1998)

4. Vadim Backman, "Polarized light scattering spectroscopy for quantitative measurement of epithelial cellular structure In Situ", IEEE Joural of selected topics in quantum electronics, Vol. 5, 1019-1026 (1999)

5. Matthew Bartlett, George Huang, Lyndon Larcom, "Measurement of particle size distribution in mammalian cells in vitro by use of polarized light spectroscopy", Appl. Opt. 43, 1296-1307 (2004)

6. Arjen Amelink, Martin P. L. Bard, Sjaak A. Burgers, and Henricus J. C. M. Sterenborg, "Single-scattering spectroscopy for the endoscopic analysis of particle size in superficial layers of turbid media", 42, 4095-4101 (2003)

7. Anatoli P. Nefedov, "Analysis of particle sizes, concentration and refractive index in measurement of light transmittance in the forward-scatter-angle range", Appl. Opt. 36 1357-1366 (1997)

8. Konstantin A. Semyanov, “Single-particle sizing from light scattering by spectral decomposition”, Appl. Opt. 26, 5110-5115 (2004)

9. Yoichi Kitagawa, “Fiber-optic particle size monitor based on white-light scattering”, Appl. Opt. 31, 859-865 (1992)

10. Murat Canpolat, “Particle size analysis of turbid media with a single optical fiber in contact with the medium to deliver and detect white light”, Appl. Opt. 40 3792-3799 (2001)

11. Milind Kandlikar and Gurumurthy Ramachandran, “Inverse methods for analyzing aerosol spectrometer measurements: a critical revew”, J. Aerosol Sci. Vol. 30 No. 4 413-437 (1999)

12. S. Twomey, “Introduction to the mathematics of inversion in remote sensing and indirect measurement”. (Dover, New York, 1996)

13. King, M. D., D. M. Byrne, B. M. Herman, and J. A. Reagan, 1978: Aerosol size distributions obtained by inversion of special optical depth measurements. *J. Atmos., Sci*., **35**, 2153-2167.

14. Hansen, P. C., 1998: *Rank-Deficient and Ill-posed problems: Numerical Aspects of Linear Inversion.* SIAM, Philadelphia, 247pp.

15. David A. Ligon, James B. Gillespie, and Paul Pellegrino: “Aerosol properties from spectral extinction and backscatter estimated by an inverse Monte Carlo method”, Appl. Opt. 39, 4402-4410 (2000)

16. David A. Ligon, Tuan W. Chen and James B. Gillspie: “Determination of aerosol parameters from light-scattering data using an inverse Monte Carlo technique”, Appl. Opt. 35, 4297-4303 (1996)

17. Mao Ye, Shimin Wang etc. “Inversion of particle-size distribution from angular light-scattering data with genetic algorithm”, Appl. Opt. 38, 2677-2685 (1999)

18. Fabio Ferri, “Modified version of the Chahine algorithm to invert spectral extinction data for particle sizing”, Appl. Opt. 34, 5829-5839 (1995)

19. Hitzenberger, R. and Rizzi, R., “Retrieved and measured aerosol mass size distributions: a comparison”, Appl. Opt. 25, 546-553 (1986)

20. H. C. Van De Hulst, “Light scattering by small particles” Dover Publications (1981).

Chapter 6 White Light Backscattering Measurement of Hydrosols Based on Fiber Optic Technique and Its Size Inversion

6.1 Introduction

When light interacts with particles, it will scatter and the scattering pattern is determined by the size, shape and refractive index of the particles. Therefore scattering measurements reveal important information about the nature of particles in a volume of water or air. For fine particle analysis, scattering measurements are superior to other sizing methods such as electron microscopy and sieving in that it can provide non-contact high quality measurement in-situ and in real time. Actually light scattering techniques for retrieval of particle properties have attracted a great deal of attention in the applied science for the past 30 years. It has been widely applied to the remote sensing of aerosols and hydrosols in the environmental science [1,2], monitoring the combustion exhaustion process in thermal energy industry and characterizing cells for pharmaceutical and medical purpose[3-5].

In standard experiments [6], laser light is collimated and sent through a sample cell containing particles (Fig.1). The scattered light at different scattering angles is collected in the far field after a Fourier lens which focuses it onto a series of rings with various radius of the CCD. Alternatively putting a variable aperture diaphragm before the detector in a transmissometer system, the near forward angle scattering can be also recorded with variable field of view [7]. Other instruments capable of measuring the angular scattering over all the space usually requires either

many optical sensors arranged at various location over a spherical stage or complicated mechanisms to rotate one sensor around the sample cells[8,9]. On the other hand, multi-wavelength backscatter and extinction measurements with much simpler layout are often enough to obtain aerosol size information in Lidar system [1]. However, all these laser based optical systems require complicated geometric configurations, expensive and bulky equipments, as well as demanding and time-consuming adjustments. In addition, it can not provide continuous light scattering spectra since the available wavelength for laser light source is very limited.

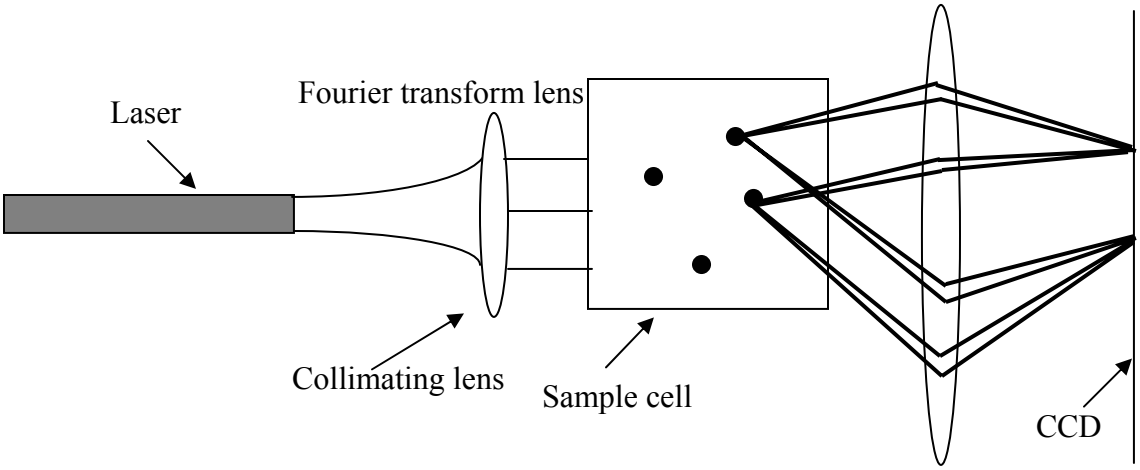

Figure 1 Standard experiment of scattering measurement for particle sizing

Recently, the scattering spectra measurements using compact fiber probes and white light sources have generated much interest in particle sizing applications [10-12]. The convenient optical arrangement and inexpensive design are ideal for in-situ and field measurement. In [10], two fibers with rod lens were used for the measurement: one delivers the white light to the samples, the other collect the scattering at one position. The white light scattering spectra can be also obtained with single optical fiber for both delivery and collection. The polarized single

backscattering spectrum from the upper layer of turbid media is distinguished from the multi-scattering background through a specially designed fiber probe consists of three fibers glued with polarization films with one fiber delivering polarized illumination and two fibers collecting two cross polarized backscattered signal[11]. All of them were used for analysis of particles or biological cells with nearly single sizes or very narrow width. In this chapter, we present a simple and portable system based on fiber probe and palm-size spectrometer to measure white light backscatter spectra. The performance of this system is evaluated by both standard mono-dispersed samples made of several different materials as well as samples with complex distributions made up of mixing individual narrow dispersions. The TIM method has been also applied to the obtained experimental data to retrieve both sizes and refractive index.

6.2 White-light backscattering measurement based on fiber optics technique

The experiment setup is shown in Fig. 2. A backscatter fiber probe from Ocean Optics Inc. (FDP-14UV200-11-5-Ref) was used for the measurement. The probe tip has one fiber in the center collecting the backscatter signal into the spectrometer (Ocean optics, S2000) and six fibers around it delivering the light source to the sample. One additional fiber is splitted from the illumination fiber bundle for light source monitoring. The diameters for all the fibers were 200μm and the fiber numerical aperture (NA) was 0.22. The light source was a 150w DC regulated QTH fiber optic illuminator from Dolan Jenner (DC-950) and was coupled through a focusing lens into the fiber. To avoid the specular reflections, the fiber

probe was tilted by 10˚ and placed just beneath the surface of the sample solutions. The backscatter signal spectrum was collected over the wavelength range of 0.4-0.75μm (limited by the light source) and 71 wavelength points in this range, at an interval of 5nm, were used for the retrievals. The collected signal I_c was spectrally calibrated against the backscatter spectrum from a Spectralon plate (Labsphere PT# SRT-99-020) I_s after subtracting the dark background I_b so that: $b_{\exp} = \frac{I_c - I_b}{I_s - I_b}$. Again since only the relative backscatter spectrum matters, b_{exp} is normalized such that the norm of the vector containing 71 measured backscatter amplitude is unity.

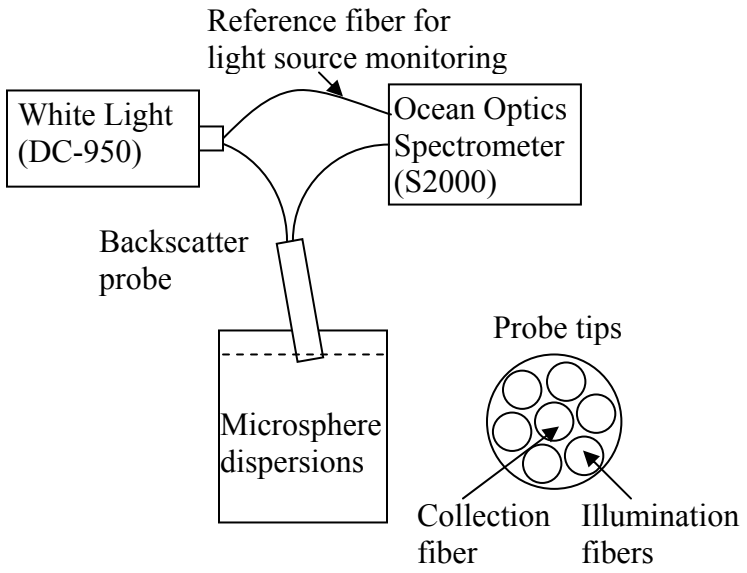

Figure 2 Experimental arrangement: White light is delivered to the sample container by the six illuminating fibers. The backscattered signal is then collected by one fiber in the center of the probe and directed to the spectrometer. To avoid the specular reflections, the fiber probe is titled by 10˚ and placed just beneath the surface of the sample solutions. A fraction of the white light power is delivered directly to the spectrometer by the reference fiber for light source monitoring. All the fibers have a diameter of 200μm and a numerical aperture (NA) of 0.22.

Ten aqueous suspensions (w =10% solids by weight) of mono-disperse polystyrene micro-spheres (5000 Series Duke Scientific) were used to evaluate both the fiber optic system and the retrieval method later for narrow mono-mode distributions. Diameters of the micro-spheres were 0.2, 0.5, 0.67, 0.74, 0.82, 0.87,

0.93, 1.0, 1.3 and 2.02μm with size fluctuations within 3%-5% of the nominal diameters as stated by the manufacturer. The refractive index of polystyrene is 1.589 at 589nm and its density is ρ_s =1.05g/cm^3. V_s =20μl of each sample was diluted in V=200ml of distilled water. This 200ml diluted solution was placed in a deep thin black container for backscatter measurement so that the influence of the container walls on scattering signal was negligible. This was experimentally verified. The number concentration of particles in the solution is estimated by $N_0 \approx \frac{V_s \rho \cdot w}{\rho_s V v}$, ρ is the water density (1.0 g/cm^3) and v is the volume of a single particle $\frac{4}{3}\pi r^3$. In order to obtain experimental data for the sample with a broad distribution, we mixed 7 mono-dispersed micro-spheres with various concentrations to approximate the log-normal distribution with r_m=0.41μm and σ=0.1 assuming that the distribution for each of the standard samples is a log-normal distribution with σ=0.03, as shown in the Fig. 8. Among these 7 samples, 6 of them were from Duke Scientific (with diameters: 0.67, 0.74, 0.81, 0.87, 0.93, and 1.0μm) and were also used for narrow distribution testing. One was from Polysicence with mode diameter d_m=0.77μm, δ=0.025μm and solid concentration w=2.62%. In addition to polystyrene particles, measurement was also made for particle sample made of two different polymers: polymethacrylate with n_p= 1.48 (1.113 relative to water), d=1.0μm and melamine resin with n_p=1.68 (1.263 relative to water), d=2.0μm. Both of them are from Sigma Aldrich with and w=10%. All the samples were sufficiently diluted to be in the single scattering regime, which has been validated through linearity test.

6.3 Results

6.3.1 Linearity test

Linearity tests including repeated dilution and superposition of component signals were performed to make sure that only single scattering events are dominant in the measurement. In dilution test, we repeated the measurements for all the samples with half of the original concentration. The spectra dependence of both backscatter keep the same for the original and diluted samples. One of the results for d=0.82μm is displayed in Fig.3 (left panel). We also mixed several mono-dispersed samples together and record their backscatter spectrum. Again the shape of this spectrum from the mixture is consistent with the sum of the individual backscatter spectrum from the component samples. All these test results prove that only single scattering is important in our measurement.

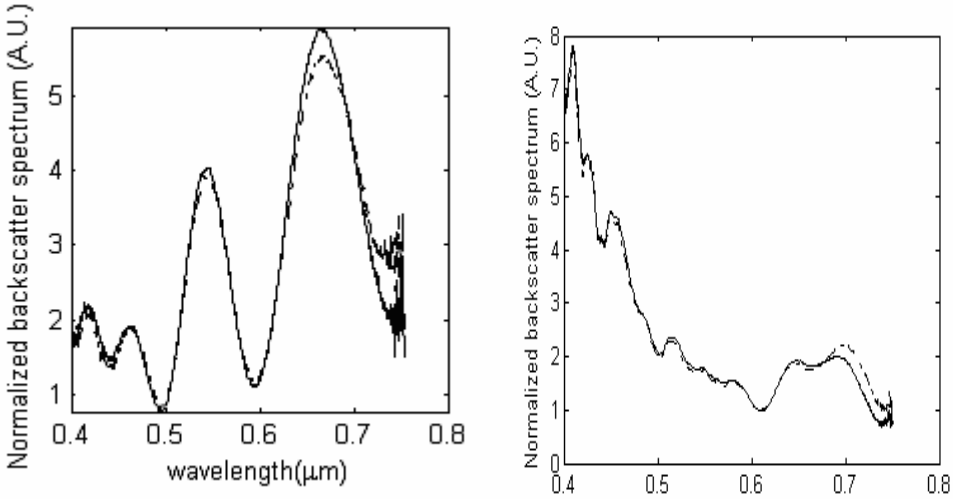

Figure 3 Backscattering spectra for linearity test: dilution test (left) and mixture test (right). Left: solid, original concentration; dashed line, half of the concentration;
Right: solid, mixed sample; dashed line, sum of backscatter from component samples

6.3.2 Comparison with computer-generated data

In order to check if the forward calculation based on eq (1) and (2) reproduce the experimental results, comparison was made between the computer-generated spectra (dotted line) and the experimental data (solid line) in Fig 4-5 by assuming log-normal distribution with the nominal radius provided by the manufacturer as the modal radius r_m and the modal width σ fixed at 0.01 for all the mono-dispersed samples. Fig.4 shows the spectra for three of the polystyrene particles from Duke scientific with d=0.2, 1.0 and 2.02μm. Scattering spectra for samples from Sigma Aldrich are displayed in Fig5. Not all the locations of the oscillatory peaks in the backscattering spectrum match exactly to simulated results, as seen, for instance, in Fig 4(c). Considering the accuracy of nominal radius is actually within 3% and the oscillations in backscattering spectra from mono-dispersed particles are very sensitive to the choice of radius and width of the input particle distribution, a least square fitting was applied to the experimental data by adjusting the mean sizes within 3%, σ in the range of [0.01, 0.03] and fixing the refractive index. In this way, knowledge about the particle distribution based on lognormal distribution can be obtained. The fitted radius and width are listed in Table 1 and the corresponding spectra are plotted in Fig. 4 and 5 using dashed line. Using the fitted distribution parameters, the agreement between simulation and experiments for backscatter becomes much better.

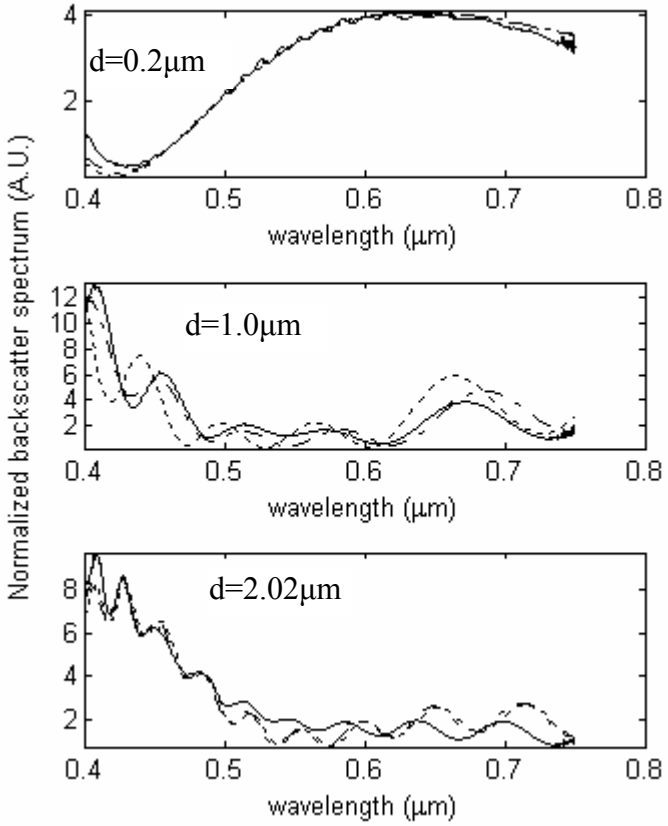

Figure 4 Backscattering spectra for three mono-dispersed samples: solid, measurement data; dashed line, fitting; dotted line, Mie calculation

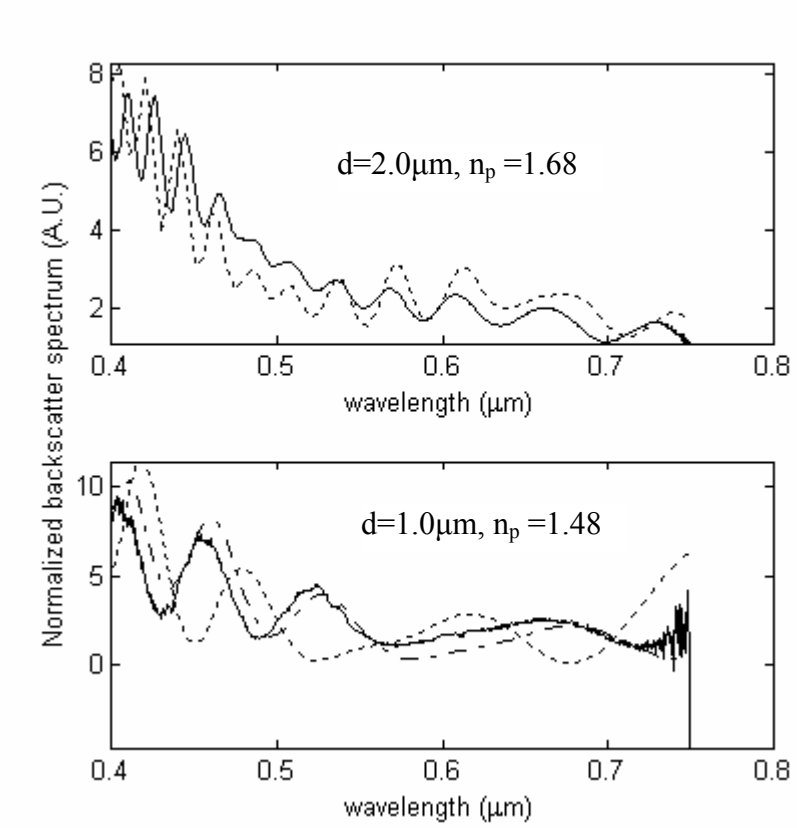

Figure 5 Backscattering for mono-dispersed non-polystyrene samples. Solid, measured data; dotted line, computer generated data; dashed line, fitted results

For the broad distribution sample made from the mixture of several standard single size particles, the simulation and measured backscatter spectra were plotted together in Fig. 6. This mismatch may be caused by that the mixed distribution is not as smooth as the standard log-normal distribution. Despite of this, the general shape of the spectrum is still considered to be satisfactory.

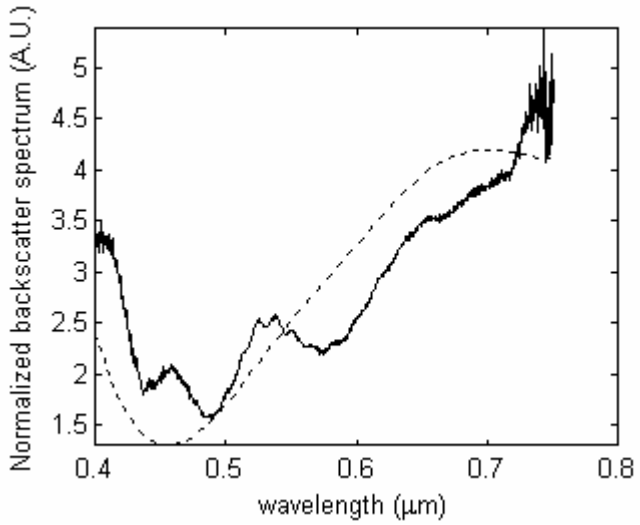

Figure 6 Backscattering for broad distribution samples. Solid, measured data; dotted line, computer generated data

6.4 Inversion results

The retrieved mean diameter and the standard deviation are listed in Table. 1. Except for the 0.2μm particles, the recovered mean sizes are very consistent with nominal sizes to within 8% accuracy, which is reasonable considering the claimed 3%-5% size uniformity of these samples. The 0.2μm particle size is outside the minimum size bin (0.22μm in diameter) used in the retrieval, which is the reason for the failure in retrieving the right particle size for this sample. The retrieved PSDs and the fitted backscatter spectra are also plotted in Fig. 10 for three samples: 0.5, 0.93 and 2.02μm. The backscatter spectra calculated from the output PSD function match with the measured data with a fitting residual of less than 10%. The retrieval results for the broad distribution are shown in Fig. 7. For comparison we have also plotted the experimental data and the retrieved spectra on the same graph. As seen from Fig. 8, due to the limited availability of diameter sizes, for standard particles, the resulting

mixture is not exactly a log-normal distribution. The retrieved PSD has the mean radius r_{ret}=0.436μm and δ_{ret}=0.052μm.

Finally we mixed the four of the mono-dispersed particles with different concentrations. The four samples chosen were 0.5, 0.67, 0.82 and 1.0μm in diameters and their relative mixing ratios are proportional to $1/r^3$: 8.5:3.8:2:1. Fig. 9 shows the retrieved PSD. The TIM can locate the four peaks very accurately, while the discrepancy in the relative amplitude between each mode is mainly due to the limited resolutions of the discrete size bins, which is consistent with the simulation results in the previous chapter.

Table 1 Narrow distribution retrieval from experimental backscattering data

Samplediameter(μm)		0.2	0.5	0.67	0.74	0.82	0.87	0.93	1.0	1.3	2.02
Retrievals	d(μm)	0.78	0.51	0.67	0.76	0.84	0.89	0.93	1.03	1.19	2.03
	δ_{ret}(μm)	0.03	0.01	0.03	0.03	0.04	0.04	0.04	0.06	0.07	0.07
fit	dm	0.20	0.51	0.66	0.73	0.82	0.88	0.93	1.03	1.31	2.01
	σ	0.03	0.02	0.02	0.02	0.02	0.03	0.02	0.02	0.02	0.01

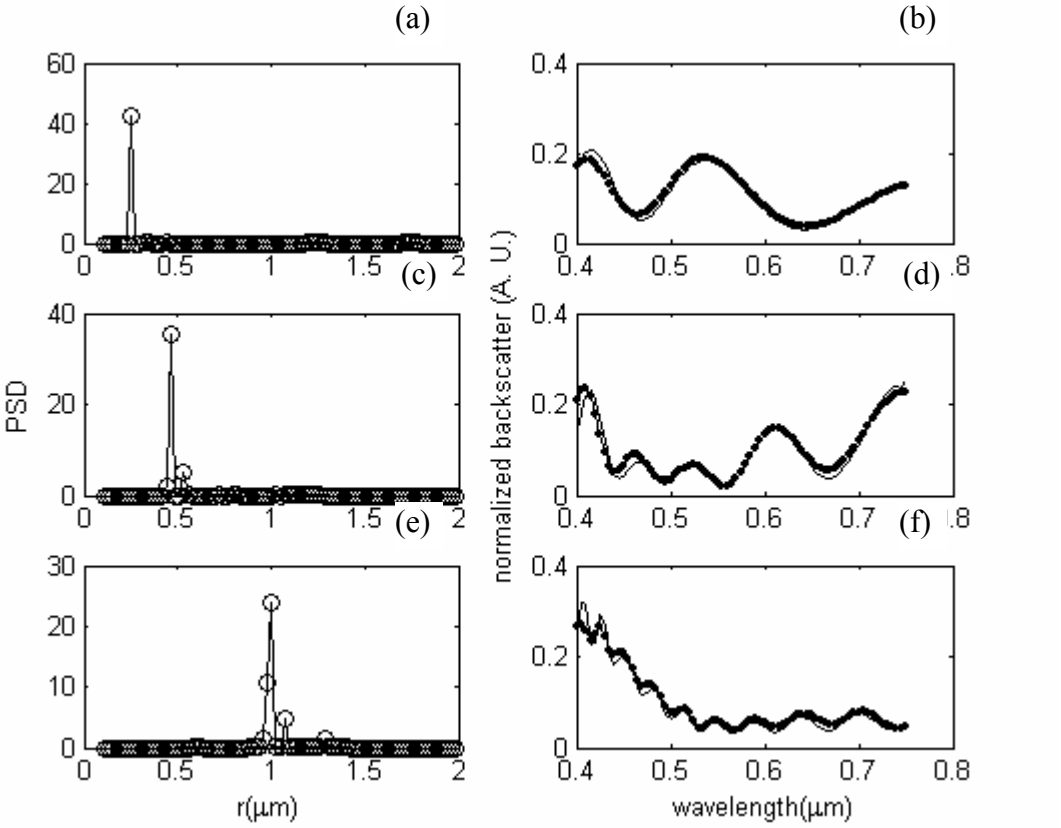

Figure 7 Retrieved PSD (left, solid line with circle) from the experimental backscatter signals (right, solid line) for three samples with nearly mono-dispersed distribution. (a), (b): d_m= 0.5μm;(c), (d): d_m=0.93μm; (e), (f): d_m=2.02μm. For comparison the fitted backscatter data (dot) are also plotted in (b), (d) and (f)

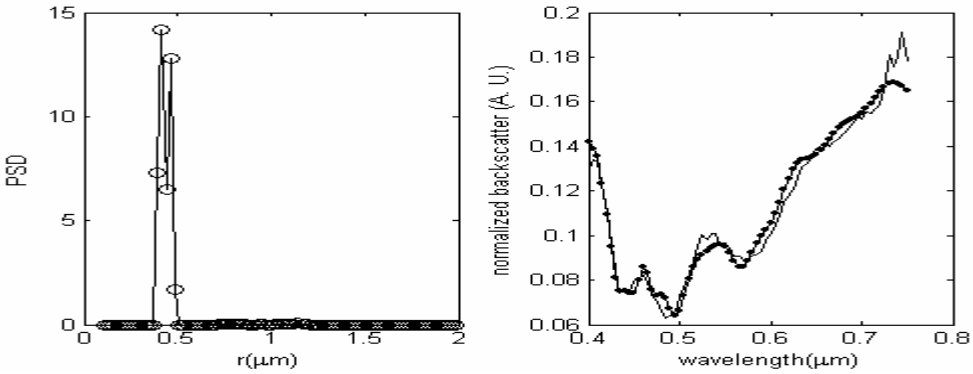

Figure 8 Retrieved PSD (left, solid line with circle) from the experimental backscatter signals (right, solid line) for broad distribution: r_m=0.41μm, σ=0.1 and r_{ret}=0.436μm, δ_{ret}=0.052μm. The dot symbols on the right figures represent the fitted data

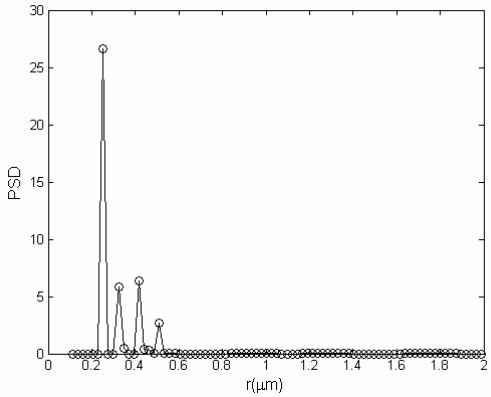

Figure 9 Multi-mode distribution retrieval of experimental data

As for the refractive index retrieval, two samples, one polystyrene particles with d = 2.02μm and one polymethacrylate particle with d =1μm and n=1.113 from Sigma Aldrich are used to test this refractive index retrieval procedure. It can be seen from Fig. 10 that both refractive index and mean diameters are recovered fairly well with n=1.2, d=2.01μm and n=1.1, d=1.1μm for polystyrene and polymethacrylate particles respectively.

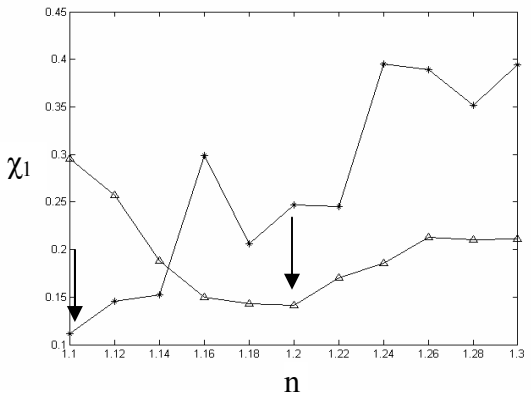

Figure10 Refractive index retrieval of experimental data. triangle: polystyrene particles with d = 2.02μm and n=1.196 from Duke Scientific; star: polymethacrylate particle with d =1μm and n=1.113 from Sigma Aldrich

6.5 Conclusion

A fiber optical system has been created to measure backscatter white light spectrum. The performance of the system is tested through standard mono-dispersed particles made of three different materials with known refractive index and particle sizes as well as broad distributed samples made by mixture of several nearly mono-dispersed particle samples. Comparison with the computer generated spectra shows that the measurements can generally reproduce the simulation results for all the samples used here, which also shows that it is possible to obtain a reliable measurement of white light backscattered spectrum from water-suspended particles by the compact and portable fiber-optical system. The success of the size and refractive retrieval from the experimental spectra further proves that the TIM method is a fast practical inversion approach for micro-physics analysis of water-borne particles.

Reference:

1. D. Muller, F. Wagner, U. Wandinger and A. Ansmann, M. Wendisch, D. Althausen and W. V. Hoyningen-Huene, "Microphysical particle parameters from extinction and backscatter lidar data by inversion with regularization: experiment", Appl. Opt. 39, 2346-2357 (2000)

2. Kusiel S. Shifrin, "Spectral attenuation and aerosol particle size distribution", Appl. Opt. 35 2114-2124 (1996)

3. L. T. Perelman, V. Backman, M. Wallace, G. Zonios, R. Manoharan, A. Nusrat, S. Shields, M. Seiler, C. Lima, T. Hamano, I. Itzkan, J. Van Dam, J. M. Crawford and M. S. Feld, " Observation of Periodic Fine Structure in Reflectance from Biological Tissue: A New Technique for Measuring Nuclear Size Distribution", Phys. Rev. Lett. 80, 627-630 (1998)

4. Vadim Backman, "Polarized light scattering spectroscopy for quantitative measurement of epithelial cellular structure In Situ", IEEE Joural of selected topics in quantum electronics, Vol. 5, 1019-1026 (1999)

5. Matthew Bartlett, George Huang, Lyndon Larcom, “Measurement of particle size distribution in mammalian cells in vitro by use of polarized light spectroscopy”, Appl. Opt. 43, 1296-1307 (2004)

6. R. Xu, “Particle characterization using light scattering techniques”, Kluwer Academic, London (2000).

7. Anatoli P. Nefedov, “Analysis of particle sizes, concentration and refractive index in measurement of light transmittance in the forward-scatter-angle range”, Appl. Opt. 36 1357-1366 (1997)

8. P. J. Wyatt, K. L. Schehrer, S. D. Phillips, C. Jackson, Y-J. Chang, R. G. Parker, D. T. Philips and J. R. Bottiger, “Aerosol particle analyzer”, Appl. Opt. 27, 217-221 (1988)

9. H. R. Haller, C. Destor, and S. Canell, “Photometer for quasielastic and classical light scattering”, Rev. Sci. Instrum. 54, 973-983 (1983)

10. Yoichi Kitagawa, “Fiber-optic particle size monitor based on white-light scattering”, Appl. Opt. 31, 859-865 (1992)

11. A. Myakow, L. Nieman, L. Wicky, U. Utzinger, R.Richards-Kortum, K. Sokolov, “Fiber optic probe for polarized reflectance spectroscopy in vivo: Design and performance”, J. Biomed. Opt., Vol. 7, 388-397 (2002)

12. Murat Canpolat, “Particle size analysis of turbid media with a single optical fiber in contact with the medium to deliver and detect white light”, Appl. Opt. 40 3792-3799 (2001)

Bibliography

Chapter 2

1. C. D. Mobley, “Light and Water: Radiative Transfer in Natural Waters”, Academic Press, New York, 1994

2. C. S. Roesler, M. J. Perry, “In situ phytoplankton absorption, fluorescence emission and particulate spectra determined from reflectance”, J. Geoph. Res. Vol. 100, 13279-13294 (1995)

3. B. Hamre, O. Frette, S. R. Erga, J. J. Stamnes and K. Stamnes, “Paramterization and analysis of the optical absorption and scattering coefficients in a western Norwegian fjord: a case II water study”, Appl. Opt. 42, 883-892 (2003)

4. G. Chang, K. Mahoney, A. Briggs-Whitmire, D.D.R. Kohler, C.D. Mobley, M. Lewis, M.A. Moline, E. Boss, M. Kim, W. Philpot, and T.D. Dickey, “The New Age of Hyperspectral Oceanography”, Oceanography, Vol. 17, 16-23 (2004)

5. T.D. Dickey, “Studeis of Coastal Ocean Dynamics and Processes Using Emerging Technologies”, Oceanography, Vol. 17, 10-13 (2004)

6. Van de Hulst, “Light Scattering by Small Particles”, Dover Publications, 1981

7. K. Carder1, F. Chen1, J. Cannizzaro1, J. Campbell, “Performance of MODIS Semi-Analytic Ocean-Color Algorithms: Chlorophyll a, Absorption Coefficients, and Absorbed Radiation by Phytoplankton (ARP)”, poster

8. Wetlabs instrument manual

9. M. S. Twardowski, E. Boss, J. B. Macdonald, W. Scott Pegau, A. H. Barnard and J. V. Zaneveld, “A model for estimating bulk refractive index from the optical backscattering ratio and the implications for understanding particle composition in case I and case II waters”, J. Geoph. Res. Vol. 106, 14129-14142 (2001)

10. M. Stramska and D. Stramski, “Effects of a nonuniform vertical profile of chlorophyll concentration on remote-sensing reflectance of ocean”, Appl. Opt. 1735-1747 (2005)

Chapter 3

1. E. Fuchs, “Separating the Fluorescence and Reflectance Components of Coral Spectra”, Appl. Opt. 40 (2001) 3614-3621.

2. J.F.R. Gower, R. Doerffer, G.A. Borstad, “Interpretation of the 685nm peak in water-leaving radiance spectra in terms of fluorescence, absorption and scattering, and its observation by MERIS”, Int. J. Rem. Sens. 20 (1999) 1771-1786.

3. A.A. Gitelson, Y.Z. Yacobi, D.C. Rundquist, R.Stark, L.Han, and D. Etzion. “Remote estimation of chlorophyll concentration in productive waters: Principals, algorithm development and validation”, Proc. of NWQMC (Austin Texas, 2000) 149-160.

4. K.H. Szekielda, C.Gobler, B.Gross, F.Moshary, S. Ahmed, “Spectral Reflectance measurements of estuarine waters”, Ocean Dynamics 53 (2003) 98-102.

5. F. Grum, Colorimetry of fluorescent materials, in Optical Radiation Measurements, vol. 2, Academic, New York, 1980, Chap. 6.

6. J.M. Schmitt, A.H. Gandjbakhche, R.F. Bonner, “Use of polarized light to discriminate short-path photons in a multiply scattering medium”, Appl. Opt. 31 (1992) 6535-6546.

7. S.G. Demos, R.R.Alfano, “Temporal gating in highly scattering media by the degree of optical polarization”, Opt. Lett. 21 (1996) 161-163.

8. S.P. Morgan, M.P. Khong, M.G. Somekh, “Effects of polarization state and scatterer concentration on optical imaging through scattering media”, Appl. Opt. 36 (1997) 1560-1565.

9. S.P. Schilders, X.S. Gan, Min Gu, “Effect of scatterer size on microscopic imaging through turbid media based on differential polarisation-gating”, Opt. Comm. 157 (1998) 238-248.

10. A. Cunningham, P. Wood, D. McKee, “Brewster-angle measurements of sea-surface reflectance using a high resolution spectroradiometer”, J. Opt. A: Pure Apl. Opt. 4 (2002) S29-S33.

11. S. Ahmed, A. Gilerson, A. Gill, B. M. Gross, F. Moshary, J. Zhou, “ Separation of Fluorescence and Elastic Scattering from Algae in Seawater Using Polarization Discrimination”, Opt. Comm. Vol 235/1-3, (2004) , pp23-30

12. D. Stramski., A.Bricaud, A.Morel, “Modeling the Inherent Optical Properties of the Ocean Based on the Detailed Composition of the Planktonic Community”, Appl. Opt. 40 (2001) 2929-2945.

13. C.F. Bohren, D.R. Huffman, Absorption and Scattering of Light, Wiley, John & Sons, 1998.

14. L. Prieur, S. Sathyendranath, “An optical classification of coastal waters based on the specific spectral absorption curves of phytoplankton pigments, dissolved organic matter and other particulate materials”, Limnolog. Oceanogr. 26 (1981) 671-689.
15. S.Ahmed, M.A. Ali, K. Mitwally, and M. El-Massry, J. Chem. Phys. 91 (1989) 3838-3845.

16. C. D. Mobley, Light and Water. Radiative Transfer in Natural Waters, Academic Press, New York, 1994.

17. H. Volten, J.F. de Haan, J.W. Hovenier, R. Schreurs, W. Vassen, A.G. Dekker, H.J. Hoogenboom, F.Charlton, R. Wouts, Limnolog. Oceanogr. 43 (1998) 1180-1197.

Chapter 4

1. A. Morel and L. Prieur, “Analysis of variations in ocean color”, Limnol. Oceanogr. 22, 709-722, 1977

2. J. E. O’Reilly, S. Maritorena, B. G. Mitchell, D. A. Siegel, K. L. Carder, S. A. Garver, M. Kahru and C. McClain, “Ocean color chlorophyll algorithms for SeaWiFS”, J. Geophys. Res. 103 (C11), 1998, 24937-24953

3. M. Sydor, R. Arnone, “Effect of suspended particulate and dissolved organic matter on remote sensing of coastal and riverine waters”, Appl. Opt., 36, 6905-6912 (1997)

4. L. Han, D. C. Rundquist, L. L. Liu, R. N. Fraser, J. F. Schalles, “The spectral responses of algal chlorophyll in water with varying levels of suspended sediment”, Int. J. Rem. Sens., 15, 3707-3718 (1994)

5. J. F. Schalles, C. M. Hladik, “Remote chlorophyll estimation in coastal waters with tription and CDOM interferences”, Proceedings of the Ocean Optics XVII conference, (Fremantle, Australia, 2004).

6. G. Dall’ Olmo and A. A. Gitelson, “Effect of bio-optical parameter variability on the remote estimation of chlorophyll a concentration in turbid productive waters: experimental results”, App. Opt., 44, 412-422 (2005)

7. D. Doxaran, J. M. Froidefond, S. Lavender, P. Castaing, "Spectral signature of highly turbid waters: Application with SPOT data to quantify suspended particulate matter concentrations", Rem. Sens. Of Environm., 81, 149-161 (2002)
8. C. Hu, K. J. Voss, "Measurements of solar-stimulated fluorescence in natural waters", Limnol. Oceanogr., 43, No. 6, 1198-1206 (1998)

9. J. Fischer and U. Kronfeld, "Sun-stimulated chlorophyll fluorescence. 1. Influence of oceanic properties", Int. J. Rem. Sens., 11, 2125-2147 (1990)

10. S. R. Laney, R. M. Letelier, and M. R. Abbott, "Parameterizing the natural fluorescence kinetics of Thalassiosira weissflogii", Limnol. Oceanogr., 50, 1499-1510 (2005)

11. D. Pozdnyakov, A. Lyaskovsky, H. Grassl and L. Petterson, "Numerical modeling of transpectral process in natural waters: implications for remote sensing", Int. J. Rem. Sens., 23, NO.8, 1581-1607 (2002)

12. J.F.R. Gower, R. Doerffer, G.A. Borstad, "Interpretation of the 685 nm peak in water-leaving radiance spectra in terms of fluorescence, absorption and scattering, and its observation by MERIS," Int. J. Rem. Sens. 20, 1771-1786 (1999)

13. J. Chowdhary, "Multiple Scattering of Polarized Light in Atmosphere-Ocean Systems: Application toSensitivity Analyses of Aerosol Polarimetry," Ph.D. thesis, Columbia University. New York, N.Y (1999)

14. J. Chowdhary, B. Cairns, M.I. Mishchenko, P.V. Hobbs, G.F. Cota, J. Redemann, K. Rutledge, Holben B.N., and E. Russell, "Retrieval of aerosol scattering and absorption properties from photopolarimetric observations over the ocean during the CLAMS experiment," J. Atmos. Sci. 62, 1093-1117 (2005)

15. D. Stramski., A. Bricaud, A. Morel, "Modeling the inherent optical properties of the ocean based on the detailed composition of the planktonic community", Appl. Opt., 40, 2929-2945 (2001)

16. A. Morel, "Optical modeling of the upper ocean in relation to its biogenuous matter content (Case 1 waters)," J. Geophys. Res. 93, No C9, 10749-10768 (1988)

17. C. Cox, W. Munk, "Statistics of the sea-surface derived from sun-glitter," J. Mar. Res., 13, 198-227 (1954)

18. M.Babin, A.Morel and B. Gentili, "Remote sensing of sea surface Sun-induced chlorophyll fluorescence: consequences of natural variations in the

optical characteristics of phytoplankton and the quantum yield of chlorophyll a fluorescence," Int. J. Rem. Sens., 17, 2417-2448 (1996)

19. S.A. Green, N.V. Blough, "Optical absorption and fluorescence properties of chromophoric dissolved organic matter in natural waters," Limnol. Oceanogr, 39, No 8, 1903-1916 (1994).
20. A. Morel, "Light and marine photosynthesis: a spectral model with geochemical and climatological implications," Prog. Oceanogr. 26, 263-306 (1991)

21. M. Chamin, R. Santer, E. Dilligeard, "Radiative transfer model for the computation of radiance and polarization in an ocean-atmosphere system: polarization properties of suspended matter for remote sensing", Appl. Opt., 40, 2938-2416 (2001)

Chapter 5

1. Detlef Muller, Ulla Wandinger and Alber Ansmann, "Microphysical particle parameters from extinction and backscatter lidar data by inversion with regularization: theory", Appl. Opt. 38, 2346-2357 (1999)

2. Kusiel S. Shifrin, "Spectral attenuation and aerosol particle size distribution", Appl. Opt. 35 2114-2124 (1996)

3. L. T. Perelman, V. Backman, M. Wallace, G. Zonios, R. Manoharan, A. Nusrat, S. Shields, M. Seiler, C. Lima, T. Hamano, I. Itzkan, J. Van Dam, J. M. Crawford and M. S. Feld, " Observation of Periodic Fine Structure in Reflectance from Biological Tissue: A New Technique for Measuring Nuclear Size Distribution", Phys. Rev. Lett. 80, 627-630 (1998)

4. Vadim Backman, "Polarized light scattering spectroscopy for quantitative measurement of epithelial cellular structure In Situ", IEEE Joural of selected topics in quantum electronics, Vol. 5, 1019-1026 (1999)

5. Matthew Bartlett, George Huang, Lyndon Larcom, "Measurement of particle size distribution in mammalian cells in vitro by use of polarized light spectroscopy", Appl. Opt. 43, 1296-1307 (2004)

6. Arjen Amelink, Martin P. L. Bard, Sjaak A. Burgers, and Henricus J. C. M. Sterenborg, "Single-scattering spectroscopy for the endoscopic analysis of particle size in superficial layers of turbid media", 42, 4095-4101 (2003)

7. Anatoli P. Nefedov, "Analysis of particle sizes, concentration and refractive index in measurement of light transmittance in the forward-scatter-angle range", Appl. Opt. 36 1357-1366 (1997)

8. Konstantin A. Semyanov, “Single-particle sizing from light scattering by spectral decomposition”, Appl. Opt. 26, 5110-5115 (2004)

9. Yoichi Kitagawa, “Fiber-optic particle size monitor based on white-light scattering”, Appl. Opt. 31, 859-865 (1992)

10. Murat Canpolat, “Particle size analysis of turbid media with a single optical fiber in contact with the medium to deliver and detect white light”, Appl. Opt. 40 3792-3799 (2001)

11. Milind Kandlikar and Gurumurthy Ramachandran, “Inverse methods for analyzing aerosol spectrometer measurements: a critical revew”, J. Aerosol Sci. Vol. 30 No. 4 413-437 (1999)

12. S. Twomey, “Introduction to the mathematics of inversion in remote sensing and indirect measurement”. (Dover, New York, 1996)

13. King, M. D., D. M. Byrne, B. M. Herman, and J. A. Reagan, 1978: Aerosol size distributions obtained by inversion of special optical depth measurements. J. Atmos., Sci., 35, 2153-2167.

14. Hansen, P. C., 1998: Rank-Deficient and Ill-posed problems: Numerical Aspects of Linear Inversion. SIAM, Philadelphia, 247pp.

15. David A. Ligon, James B. Gillespie, and Paul Pellegrino: “Aerosol properties from spectral extinction and backscatter estimated by an inverse Monte Carlo method”, Appl. Opt. 39, 4402-4410 (2000)

16. David A. Ligon, Tuan W. Chen and James B. Gillspie: “Determination of aerosol parameters from light-scattering data using an inverse Monte Carlo technique”, Appl. Opt. 35, 4297-4303 (1996)

17. Mao Ye, Shimin Wang etc. “Inversion of particle-size distribution from angular light-scattering data with genetic algorithm”, Appl. Opt. 38, 2677-2685 (1999)

18. Fabio Ferri, “Modified version of the Chahine algorithm to invert spectral extinction data for particle sizing”, Appl. Opt. 34, 5829-5839 (1995)

19. Hitzenberger, R. and Rizzi, R., “Retrieved and measured aerosol mass size distributions: a comparison”, Appl. Opt. 25, 546-553 (1986)

20. H. C. Van De Hulst, “Light scattering by small particles” Dover Publications (1981).

Chapter 6

1. D. Muller, F. Wagner, U. Wandinger and A. Ansmann, M. Wendisch, D. Althausen and W. V. Hoyningen-Huene, “Microphysical particle parameters from extinction and backscatter lidar data by inversion with regularization: experiment”, Appl. Opt. 39, 2346-2357 (2000)

2. Kusiel S. Shifrin, “Spectral attenuation and aerosol particle size distribution”, Appl. Opt. 35 2114-2124 (1996)

3. L. T. Perelman, V. Backman, M. Wallace, G. Zonios, R. Manoharan, A. Nusrat, S. Shields, M. Seiler, C. Lima, T. Hamano, I. Itzkan, J. Van Dam, J. M. Crawford and M. S. Feld, “ Observation of Periodic Fine Structure in Reflectance from Biological Tissue: A New Technique for Measuring Nuclear Size Distribution”, Phys. Rev. Lett. 80, 627-630 (1998)

4. Vadim Backman, “Polarized light scattering spectroscopy for quantitative measurement of epithelial cellular structure In Situ”, IEEE Joural of selected topics in quantum electronics, Vol. 5, 1019-1026 (1999)

5. Matthew Bartlett, George Huang, Lyndon Larcom, “Measurement of particle size distribution in mammalian cells in vitro by use of polarized light spectroscopy”, Appl. Opt. 43, 1296-1307 (2004)

6. R. Xu, “Particle characterization using light scattering techniques”, Kluwer Academic, London (2000).

7. Anatoli P. Nefedov, “Analysis of particle sizes, concentration and refractive index in measurement of light transmittance in the forward-scatter-angle range”, Appl. Opt. 36 1357-1366 (1997)

8. P. J. Wyatt, K. L. Schehrer, S. D. Phillips, C. Jackson, Y-J. Chang, R. G. Parker, D. T. Philips and J. R. Bottiger, “Aerosol particle analyzer”, Appl. Opt. 27, 217-221 (1988)

9. H. R. Haller, C. Destor, and S. Canell, “Photometer for quasielastic and classical light scattering”, Rev. Sci. Instrum. 54, 973-983 (1983)

10. Yoichi Kitagawa, “Fiber-optic particle size monitor based on white-light scattering”, Appl. Opt. 31, 859-865 (1992)

11. A. Myakow, L. Nieman, L. Wicky, U. Utzinger, R.Richards-Kortum, K. Sokolov, “Fiber optic probe for polarized reflectance spectroscopy in vivo: Design and performance”, J. Biomed. Opt., Vol. 7, 388-397 (2002)

12. Murat Canpolat, “Particle size analysis of turbid media with a single optical fiber in contact with the medium to deliver and detect white light”, Appl. Opt. 40 3792-3799 (2001)

Publications

1. J. Zhou, F. Moshary, B. Gross, M. Arend and S. Ahmed, "Population dynamics of Yb3+, Er3+ co-doped phosphate glass," Journal of Applied Physics, Vol. 96, No. 1, pp237-241, 2004

2. S. Ahmed, A.Gilerson, A.Gill, B.M. Gross, F.Moshary, J. Zhou, "Separation of Fluorescence and Elastic Scattering from Algae in Seawater Using Polarization Discrimination," Optics Communications, Vol 235/1-3 pp 23-30, 2004

3. J. Zhou, A. Gilerson, A. Gill, B. M. Gross, F. Moshary and S. Ahmed, "Polarization Discrimination Technique to Separate Overlapping Fluorescence and Elastic Scattering Applied to Algae in Seawater", Proceedings of SPIE, v.5544, 198-206, 2004, Denver

4. A. Gilerson, J. Zhou, A. Gill, B. M. Gross, F. Moshary and S. Ahmed, "Properties and Potential of a Polarization Technique for the Separation of the Overlapping Fluorescence and Elastic Scattering Applied to Algae in Seawater", Proceedings of SPIE, v. 5569, 2004

5. S. Ahmed, A. Gilerson, A. Gill, B.M. Gross, F. Moshary, J. Zhou. "Polarization Technique for Separating Overlapping Fluorescence and Reflectance Spectra Applied to Algae in Seawater in the Presence of Suspended Matter", Proceedings of the conference "Ocean Optics XVII", Fremantle, Australia, October, 2004

6. S. Ahmed, A. Gilerson, A. Gill, B. M. Gross, F. Moshary, J. Zhou, "Characteristics of Polarization Techniques for the Separation of the Overlapping Fluorescence and Reflectance Applied to Algae in Seawater", Proceedings of the conference IGARSS-04, Alaska, October, 2004.

7. A. Gilerson, J. Zhou, B. Elmaanaoui, B. Gross, F. Moshary, S. Ahmed. "Separation of fluorescence and scattering from algae and suspended solids in seawater through polarization: modeling and experiments." Proceedings of the Eighth International Conference on Remote Sensing for Marine and Coastal Environments, Halifax, Nova Scotia, 17-19 May 2005

8. J. Zhou, A. Gilerson, Fred Moshary, B. M. Gross, and S. Ahmed, "Fluorescence extraction from reflectance spectra of ocean water using polarization discrimination", Proceedings of the 20th Congress of the International Commission for Optics. August 2005, Changchun, China

9. A. Gilerson, J. Zhou, M. Ooa, J. Chowdhary, B. M. Gross, F. Moshary, and S. Ahmed, “Retrieval of fluorescence from reflectance spectra of algae in sea water through polarization discrimination: modeling and experiments”, accepted for Applied Optics, 2006

10. J. Zhou, F. Moshary, B. M. Gross, and S. Ahmed, “Particle size and refractive index retrieval from the backscattering spectrum of white light using the Twomey iterative method (TIM): simulation and experiment”, accepted to Applied Optics, 2006